INTERACTIONS BETWEEN BONE REMODELING AND MICRODAMAGE IN CANCELLOUS BONE

A Dissertation

Presented to the Faculty of the Graduate School

of Cornell University

In Partial Fulfillment of the Requirements for the Degree of

Doctor of Philosophy

by

Jonathan Bradford Matheny

August 2017

INTERACTIONS BETWEEN BONE REMODELING AND MICRODAMAGE IN CANCELLOUS BONE

Jonathan Bradford Matheny, Ph. D.

Cornell University 2017

Increases in bone remodeling impair the mechanical performance of cancellous bone and are associated with the progression of post-menopausal osteoporosis. Bone remodeling is expected to modify cancellous bone strength by changing both bone quantity and bone quality. Bone quality refers to factors that influence the mechanical performance of bone that are not well explained by bone mass. Here, I investigate how bone quality is changed by altering bone remodeling through pharmaceutical treatment and how aspects of bone quality affect the accumulation of tissue damage (microdamage) in cancellous bone. Finally, I investigate how bone remodeling responds to microdamage in a rabbit model of bone marrow lesions (BMLs).

First, we examine how treatment with anti-resorptive agents influences the size of individual resorption cavities. We find that anti-resorptive treatment is associated with reductions in the size of resorption cavities in rat vertebral cancellous bone. A reduction in resorption cavity size is hypothesized to decrease stress concentrations generated by the cavity during loading and thereby reduce the likelihood that damage will form nearby.

Next, we determine how treatment with sclerostin antibody modifies the trabecular morphology (shape and orientation of individual trabeculae) in a cynomolgus monkey model. We find that sclerostin antibody increases bone formation

leading to a conversion of rod-like trabeculae into plate-like trabeculae and increases thickness of both rods-like and plate-like trabeculae leading to an increase in apparent stiffness, as predicted using finite element models. Although microarchitecture was modified, the improvements in apparent stiffness were well explained by changes in bone mass suggesting that treatment changes bone mass and not bone quality.

We then examine how resorption cavities and tissue composition influence where microdamage forms and propagates in cancellous bone submitted to cyclic mechanical loading. We find that microdamage formed preferentially in the interior regions of cancellous bone and distant from trabecular surfaces and resorption cavities. The interior regions of trabeculae experience lower stresses but are composed of more brittle tissue.

Finally, we investigate the bone remodeling response to microdamage in an in vivo loading model. We find an increase in bone resorption in response to load-induced microdamage. Cancellous bone from within the bone marrow lesion displayed microdamage and increased bone resorption.

In summary, tissue composition of cancellous bone influences cancellous bone mechanics. Resorption cavities, while clearly generating stress concentrations do not influence microdamage accumulation. However, when microdamage does form within cancellous bone there is a focal increase in bone resorption.

BIOGRAPHICAL SKETCH

Jonathan Bradford Matheny was born in Aiken, South Carolina in 1988. He graduated from Aiken Christian School in 2007 as salutatorian. In 2011, he graduated magna cum laude from Clemson University in Clemson, South Carolina, with a Bachelor of Science degree in Bioengineering with a biomaterials concentration. While at Clemson University, he was named to the Tau Beta Pi engineering honors society and the Alpha Eta Mu Beta biomedical engineering honors society. He performed research in the Laboratory of Orthopaedic Design and Engineering at Clemson University, where he studied the kinematic behavior of unicondylar knee replacement systems and assisted graduate researchers in evaluating total knee replacement tribological performance. In 2010 has was selected for National Science Foundation Research Experience for Undergraduates Internship at Cleveland Clinic, where he investigated apoptosis kinetics of stem and progenitor cells in hypoxic conditions as part of a larger project to regrow fractured bone using tissue engineering. In 2015, he received his Master of Science degree in Biomedical Engineering from Cornell University in Ithaca, New York. While at Cornell University, he received the National Science Foundation Graduate Research Fellowship. His research in the Hernandez Research Group at Cornell University has been covered by more than 10 internet outlets and has appeared on the cover of BONE journal.

I dedicate this work to my mother and father who taught me how to learn and gave me the desire to be an engineer, and to my wife and son who have made each day worth living.

ACKNOWLEDGMENTS

I acknowledge funding support from the NSF through the Graduate Research Fellowship (GRFP) and research funding from the NIH and NIAMS (AR057362, AR054448 and AR007281), Amgen Inc., which also provided research specimens for one study. Proctor and Gamble provided risedronate for one study. Travel funding was provided by the Cornell University Graduate School.

I thank Dr. Christopher Hernandez for aiding in my personal and professional development through his mentorship and guidance over the last five years. I thank the members of my graduate advisory committee, Dr. Kei Hayashi and Dr. Eve Donnelly for their advice and support throughout my time at Cornell. I would also like to thank my fellow graduate students for their advice, support and friendship, and mentorship during my doctoral training. In particular, I thank Dr. Matthew Goff, Dr. Erin Cresswell, and Evgeniy Tkachenko for their invaluable training and friendship; I thank Ashley Torres for being a supportive friend and colleague on multiple research projects, and Jason Guss for being a great friend and colleague.

I thank the Cornell CARE facility for their assistance on my research projects. I thank Teresa Porri and Cornell Biotechnology Resource Center and the Cornell MRI facility for their assistance in acquiring images with NIH 1S10OD012287 funding for the ZEISS-Xradia Versa 520 X-ray Microscope and with NIH 1S10RR025502 funding for the shared Zeiss LSM 710 Confocal Microscope.

TABLE OF CONTENTS

LIST OF FIGURES

LIST OF TABLES

LIST OF ABBREVIATIONS

aBV/BV	Axial Volume/Bone Volume
aBV/TV	Axial-Bone Volume Fraction
AGEs	Advanced Glycation End Products
aTb.Th	Axial-Trabecular Thickness
BFR/BS	Bone Formation Rate (Bone Surface Referent)
BMD	Bone Mineral Density
BMDD	Bone Mineral Density Distribution
BML	Bone Marrow Lesion
BS/BV	Bone-specific surface
BS/Cv	Cavity Surface Area
BV/TV	Bone Volume Fraction
Cal	Calcein
Cv.De	Maximum Cavity Depth
Cv.V	Cavity Volume
DA	Degree of anisotropy
dLS/BS	Double-Labeled Surface
DMP1	Dentin Matrix Acidic Phosphoprotein 1
DV/BV	Damage Volume Fraction
E.De	Erosion Depth
ES/BS	Eroded Surface
FE	Finite Element
FTIR	Fourier Transform Infrared Spectroscopy
FV	Formation Volume
FV/TV	Newly formed volume fraction
HPLC	High-Performance Liquid Chromatography
HR-pQCT	High-Resolution Peripheral Quantitative Computed Tomography
IL-11	Interleukin-11
IL-6	Interleukin-6
ITS	Individual Trabecular Segmentation
Lead UA	lead uranyl acetate
LRP5	Low-Density Lipoprotein-Receptor-Related Protein 5
MAR	Mineral Apposition Rate
MEPE	Matrix Extracellular Phosphoglycoprotein
MicroCT	Microcomputed Tomography
Microdamage	Microscopic Tissue Damage
MRI	Magnetic Resonance Imaging
MS/BS	Mineralizing Surface
MS/dL.Ev	Surface Area per Double-Labeled Event
MS/sL.Ev	Surface Area per Single-Labeled Event
MSC	Mesenchymal Stem Cell
N.dL.Ev	No. of Double-Labeled Formation Events
N.dL.Ev/BS	No. of Double-Labeled Formation Events per Unit Bone Surface

N.sL.Ev	No. of Single-Labeled Formation Events
N.sL.Ev/BS	No. of Single-Labeled Formation Events per Unit Bone Surface
oBV/BV	Oblique Volume/Bone Volume
oBV/TV	Oblique-Bone Volume Fraction
OC	Osteocalcin
OPG	Osteoprotegerin
Osx	Osterix
oTb.Th	Oblique-Trabecular Thickness
OVX	Ovariectomy
P1NP	Intact N-terminal Propeptide of Type 1 Procollagen
pBV/BV	Plate Volume/Bone Volume
pBV/rBV	Plate Bone Volume /Rod Bone Volume
pBV/TV	Plate-Bone Volume Fraction
PEEK	Polyether Ether Ketone
PHEX	Phosphate-Regulating Neutral Endopeptidase, X-Linked
P-P Junc.D	Plate-Plate Junction Density
P-R Junc.D	Plate-Rod Junction Density
pTb.N	No. of Plate-Like Trabeculae
pTb.Th	Plate-like Trabecular Thickness
PTH	Parathyroid Hormone
RANKL	Receptor Activator of Nuclear Factor Kappa-B Ligand
rBV/TV	Rod-Bone Volume Fraction
R-R Junc.D	Rod-Rod Junction Density
rTb.N	No. of Rod-Like Trabeculae
rTb.Th	Rod-like Trabecular Thickness
Runx2	Runt-Related Transcription Factor-2
Scl-Ab	Sclerostin Antibody
SERM	Selective Estrogen Receptor Modulator
sLS/BS	Single-Labeled Surface
SMI	Structure Model Index
SrμCT	Synchrotron Radiation MicroCT
STIR	Short Tau Inversion Recovery
Tb.Sp	Trabecular Separation
Tb.Th	Trabecular Thickness
TBS	Trabecular Bone Score
tBV/BV	Transverse Volume/Bone Volume
tBV/TV	Transverse-Bone Volume Fraction
Tet	Tetracycline
TGF-β	Transforming Growth Factor Beta 1
tTb.Th	Transverse-Trabecular Thickness
UV	Ultraviolet
V/dL.Ev	Median Volume per Double-Labeled Event
XO	Xylenol Orange

LIST OF SYMBOLS

c	Cubed root of damage zone volume
c_{final}	Cubed root of damage zone volume at the end of the second bout of loading
$c_{initial}$	Cubed root of damage zone volume at the end of the first bout of loading
dc/dN	Damage Growth Rate
$N_{secondbout}$	Number of cycles applied between the first and second bouts of loading
ΔK	Local stress intensity factor range
m	Meter
Hz	Hertz
g	Gram
GB	Gigabyte
°C	Celsius
pH	Potential of Hydrogen
Pa	Pascal
σ	Stress
E_0	Initial Young's Modulus
N	Newton
M	Molar
Ex/Em	Excitation/Emission
SD	Standard Deviation
%	Percentage

CHAPTER 1
INTRODUCTION

1.1. Bone

Bone is present in two forms in the body, cortical and cancellous bone (Figure 1.1A). Cortical bone forms the outer layer of whole bones. Cortical bone has an ultrastructure that includes cylindrical lamellar structures known as osteons. Tissue in between osteons is known as interstitial bone. Cancellous bone, sometimes referred to as trabecular bone, is an open-cell foam network of trabeculae that is present at the ends of long bones as well as in the interior of short bones and vertebrae (Figure 1.1B). Cancellous bone tissue includes lamellar structures known as hemisosteons or "trabecular packets" and also contains interstitial bone between hemiosteons. Compared to cortical bone, cancellous bone has a greater surface to volume ratio and significantly greater porosity than cortical bone and displays relatively large (~1mm) spaces between trabeculae (~100 μm thick). Cancellous and cortical bone tissue are composed of Type I collagen fibers and nanometer sized mineral platelets of impure hydroxyapatite and water [1-3]. Both cortical bone and cancellous bone undergo a process known as bone remodeling to repair and replace bone tissue.

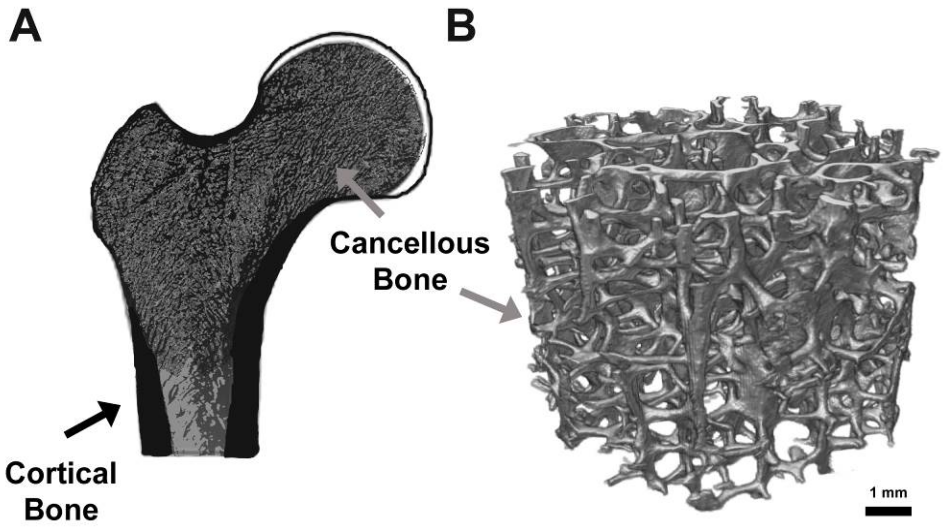

Figure 1.1. (A) A schematic showing cortical and cancellous bone in a cross-section of the proximal femur is shown. (B) A close up region of cancellous bone displaying an open-cell network of trabeculae is shown. Image in (A) adapted from Hernandez et al. [4].

1.2. Bone Remodeling and Bone Modeling

There are two ways in which bone cells modify bone volume: bone remodeling and bone modeling. Bone remodeling is a biological process in which discrete regions of bone tissue are removed by osteoclasts and replaced with new bone tissue synthesized by osteoblasts. The adult skeleton is in a continual state of bone remodeling; discrete locations of bone remodeling are present on the surfaces of trabeculae in cancellous bone as well as within osteons in cortical bone [5]. The complete resorption-formation process at one location lasts 6-9 months [6]. While bone remodeling always involves resorption followed by formation, bone modeling involves either resorption or formation. Bone modeling occurs during bone growth, following changes in mechanical loading, or due to pharmaceutical intervention (See ***Anabolic Drug Treatment***) [6, 7]. The volume of bone both resorbed and formed over a period of time is referred to a bone turnover and can be estimated using serum biomarkers of bone

formation and resorption [8]. Both bone remodeling and modeling are regulated by osteocytes. Osteocytes are cells located inside lacunae within bone tissue and form a network connecting each other and lining cells on bone surfaces. The processes involved in bone remodeling and modeling are described below (See Figure 1.2 for schematic of bone remodeling).

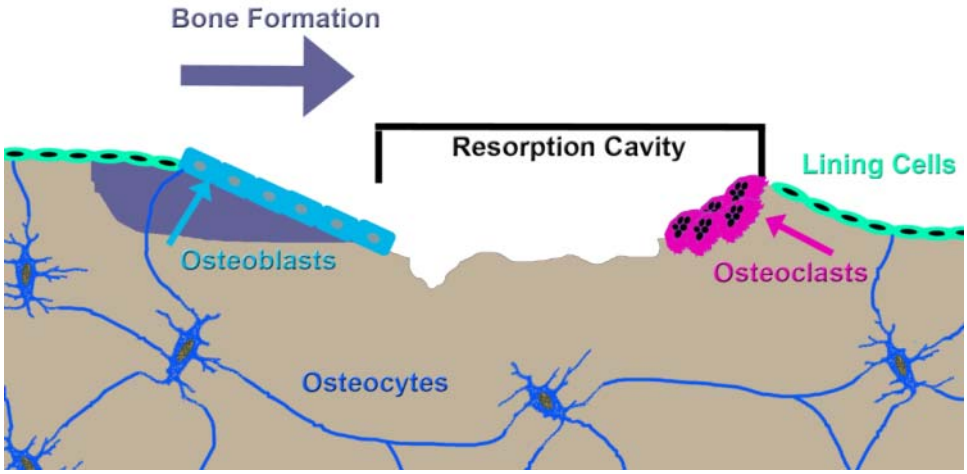

Figure 1.2. A schematic of bone remodeling is shown. Osteoclasts (pink) remove bone tissue, forming a resorption cavity. Osteoblasts (light blue) fill in the cavity with newly formed bone (shown in purple). Osteocytes (dark blue) communicate with lining cells (green) to regulate bone remodeling

1.2.1. Bone Resorption by Osteoclasts

The first step of the bone remodeling process is activation of osteoclasts [5]. Osteoclasts are derived from monocyte/macrophage precursor cells (granulocyte–macrophage colony-forming units) by the cytokine receptor activator of nuclear factor kappa-B ligand (RANKL). Osteoclastogenesis can be controlled by osteoblast/stromal cells through modification of the ratio of RANKL to osteoprotegerin (OPG, a RANKL inhibitor). Osteoclast differentiation is also regulated by interleukin-6 and -11 (IL-6 & IL-11) secreted by osteoblastic progenitor cells. The activation of RANK by RANKL

polarizes osteoclasts to resorb bone [9]. Activated osteoclasts attach to bone surfaces and release hydrochloric acid to break down the mineral component of bone and proteases to degrade the organic component of bone, leaving a resorption cavity [5, 9-11]. Osteoclasts can regulate bone remodeling by releasing transforming growth factor beta 1 (TGF-β) as bone is resorbed. TGF-β promotes osteoclast apoptosis and stimulates bone formation [12-15]. The period of bone resorption by osteoclasts at one location lasts 2-3 weeks in humans, after which osteoclasts undergo apoptosis [16].

1.2.2. Bone Formation by Osteoblasts

Osteoblasts are derived from mesenchymal stem and progenitor cells [17]. Osteoblast differentiation is promoted by a number of transcription and signaling factors, such as runt-related transcription factor-2 (Runx2), Osterix (Osx) and the low-density lipoprotein-receptor-related protein 5 (LRP5) by activating Wnt. After activation, Wnt increases levels of β-catenin in mesenchymal stem cells leading to differentiation into osteoblasts [6, 12, 16, 18, 19]. Mature osteoblasts produce and lay down new bone matrix (Type I collagen and non-collagenous proteins) filling in resorption cavities over a period of 3 months. Following bone formation, osteoblasts will either undergo apoptosis or differentiate into lining cells or osteocytes [6, 12].

1.2.3. Regulatory Function of Osteocytes

Osteocytes, derived from osteoblasts, serve a powerful regulatory function in bone. Osteocytes regulate how much bone mineral is deposited through production of Dentin Matrix Acidic Phosphoprotein 1 (DMP1), Matrix Extracellular Phosphoglycoprotein (MEPE) and Phosphate-Regulating Neutral Endopeptidase, X-Linked (PHEX). Osteocytes are mechanosensitive cells that regulate bone

modeling/remodeling. Osteocytes secrete sclerostin, a molecule which inhibits the Wnt pathway. By regulating Wnt signaling, osteocytes increase/decrease bone formation via production of sclerostin. Osteocytes also stimulate bone resorption from osteoclasts (summarized in [20]). When microdamage is formed in bone, the osteocytes in the immediate vicinity of microdamage undergo apoptosis. The viable osteocytes surrounding the microdamage then express RANKL to recruit osteoclasts to the area to resorb the damaged bone [21, 22]. The relationship between microdamage and subsequent bone resorption has been shown in cortical bone but only hypothesized in cancellous bone (For further details on microdamage, see ***Identification and Measurement of Microdamage in Bone***).

1.3. Osteoporosis and Fracture risk

Osteoporosis is a disease characterized by a reduction in bone mass. Osteoporosis affects over 10 million people, resulting in 1.5 million fractures per year in the United States and healthcare costs estimated to be $12-18 billion dollars per year [23, 24]. Most osteoporosis-related fractures involve minimal to no trauma [25] and are referred to as fragility fractures. The most common way to identify individuals with osteoporosis is through the measurement of bone mineral density (BMD) using dual x-ray absorptiometry. A person with a BMD that is 2.5 standard deviations below the reference population meets the clinical diagnosis of osteoporosis [23, 26]. BMD is influenced by bone volume, shape and tissue mineral density [27]. BMD is closely related to fracture risk but other factors also contribute to fracture risk including increased bone remodeling, estrogen depletion in post-menopausal women, and age [28-31]. Pharmaceutical treatments known as “anti-resorptive treatments” reduce the

amount of bone turnover and are therefore useful in preventing osteoporosis-related fractures.

1.5. Osteoporosis Treatments

Current osteoporosis drug treatments are classified as either anti-resorptive or anabolic based on their method of action.

1.5.1. Anti-Resorptive Drug Treatment

Anti-resorptive treatments for osteoporosis decrease the rate of bone remodeling, reducing bone turnover and preserving the existing bone microstructure. Two examples of anti-resorptive drugs are selective estrogen receptor modulators (SERMs) and bisphosphonates. Estrogen plays an important role in bone development and maintenance by suppressing bone remodeling. When circulating estrogen is depleted after the menopausal transition, the rate of bone remodeling is increased. Increases in bone turnover from remodeling causes bone loss by increasing bone resorption, perforating trabeculae by resorption events, and decreasing bone volume formed in each remodeling cycle [6, 12, 17, 32-34]. Raloxifene is a SERM used to treat osteoporosis and is an antagonist to estrogen-receptor-β and a partial agonist to estrogen-receptor-α. In patients treated with raloxifene, vertebral fractures rates are reduced by 30-50%, spinal BMD is increased (2-3%) and biomarkers of bone turnover are decreased by 20-40% [35, 36]. Bisphosphonates, such as risedronate, inhibit bone remodeling by disrupting the function of osteoclasts. Bisphosphonates bind to hydroxyapatite present on bone surfaces. When a bone surface containing bisphosphonates is resorbed, the bisphosphonate is consumed by the osteoclast and then inhibits the GTPases that regulate osteoclast cytoskeletal rearrangement,

impairing the cell's ability to resorb bone and eventually leading to apoptosis. Bisphosphonates may also inhibit osteoclastogenesis [15, 37, 38]. In patients treated with risedronate, vertebral fracture risk is decreased by 41-49%, spinal BMD is increased by 5-6%, and serum markers for bone turnover are reduced by 50% [39, 40]. While anti-resorptive drug treatments are effective at preventing fractures, there are drawbacks to this treatment option. One function of bone remodeling is remove old or damaged bone tissue. If bone turnover is inhibited, damaged tissue is less likely to be repaired by bone resorption [34]. The increase in tissue age due to inhibited bone resorption will also result in tissue with increased tissue degree of mineralization and non-enzymatic glycation: two characteristics of bone tissue associated with tissue brittleness.

1.5.2. Anabolic Drug Treatment

Anabolic drug treatments act to shift the balance of bone remodeling towards bone formation. Two examples of anabolic drug treatments are parathyroid hormone (PTH) and Sclerostin Antibody (Scl-Ab). PTH (specifically hPTH (1-34) or teraperatide) given intermittently increases bone formation by both increasing the rate of bone remodeling and increasing the amount of bone formed during each remodeling cycle [41]. In patients treated with PTH, vertebral fracture risk is decreased by 65%, spinal BMD is increased by 13% and markers of bone turnover are increased by at least 100% [42, 43]. Scl-Ab increases modeling-based bone formation and reduces bone resorption [7]. In patients treated with Scl-Ab, vertebral fracture risk is reduced by 73% and BMD is increased by 13%. Serum markers of bone formation are

increased for Scl-Ab and returned to baseline after 9-months of continuous treatment while markers for bone resorption were below levels for placebo [44].

1.6. Bone Remodeling and Bone Quality

BMD accounts of between 50-80% of whole bone strength and does not fully explain fracture risk. One study observed that 82% of postmenopausal women who experienced fractures did not meet the diagnostic threshold for osteoporosis based on BMD. The additional factors that influence bone strength and fracture risk besides bone mineral density appears to be influenced by increased bone turnover due to bone remodeling. Clinical studies indicate that biochemical markers for bone turnover can predict fracture risk independent of BMD. Furthermore, reductions in fracture risk from anti-resorptive treatments, for instance, are greater than would be expected from the associated increases in BMD [45, 46]. These clinical studies suggest that bone remodeling influences bone strength and fracture risk in ways not explained by bone mass. Differences in bone quality may explain the discrepancy between bone remodeling, bone mass and fracture risk.

Bone quality is a poorly defined term often used to refer to factors that influence the mechanical performance of bone that are not well explained by measures of bone mass or bone mineral density [47]. The primary focus of this thesis is how bone quality in cancellous bone is related to fracture risk. Most osteoporosis-related fractures occur in regions of the skeleton with high proportions of cancellous bone such as the vertebrae and proximal femur (Figure 1.1) [48]. Alterations in bone remodeling are expected to affect bone quality in cancellous bone in the following

ways: 1) increased bone resorption by osteoclasts could increase the number or size of resorption cavities which act as stress risers; 2) increased bone resorption could lead to fenestration of existing trabeculae whereas increased bone formation could lead to the creation of new trabeculae; 3) increased bone remodeling could lead to alterations to the rod- or plate-like morphology or orientation of individual trabeculae through either increased bone resorption or formation; 4) alterations in bone turnover could modify the age and composition of bone tissue. The factors mentioned above may influence pre- or post-yield mechanical properties of cancellous bone independent of bone mass and/or influence the location or amount of microdamage accumulation in bone tissue [47, 49, 50]. The subsequent sections will detail approaches that are useful in measuring aspects of bone quality that are influenced by bone remodeling as well as approaches to characterize the mechanical performance of cancellous bone (See Figure 1.3).

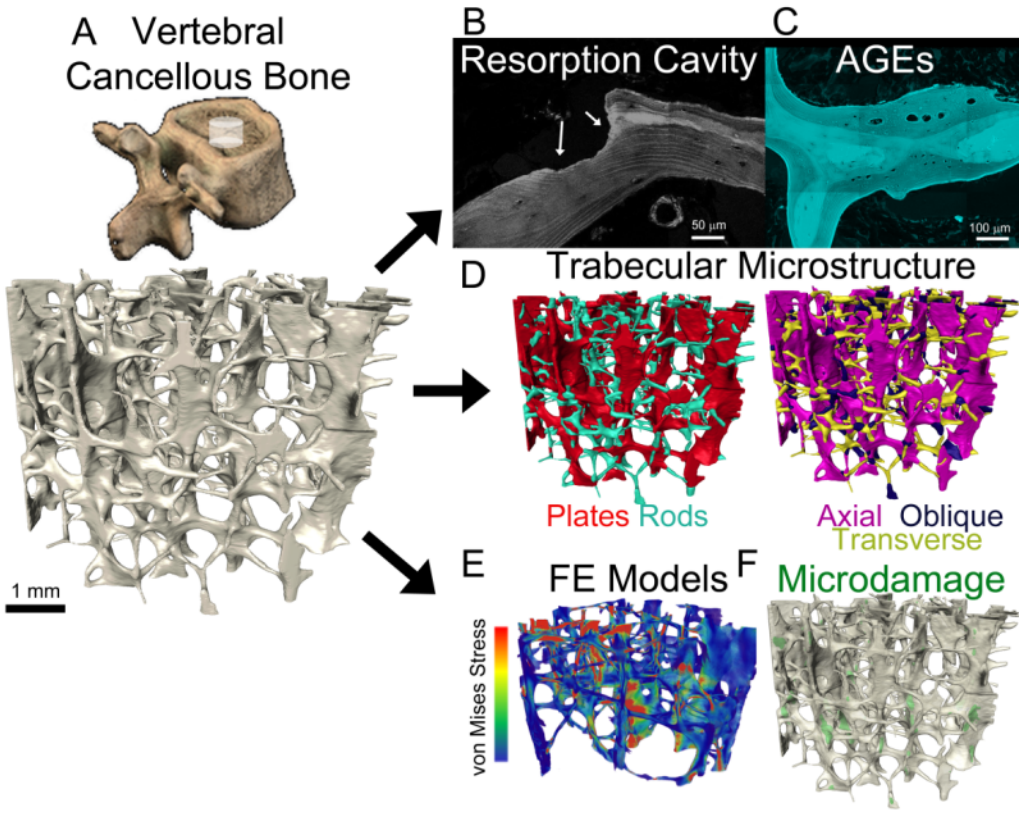

Figure 1.3. (A) Analyses of cancellous bone microstructure are used to determine factors that influence bone strength other than bone mass. A cylindrical region of cancellous bone microstructure from a vertebra is shown. Aspects of bone quality in cancellous bone include: (B) Bone remodeling events (resorption cavity shown as scalloped surface), (C) tissue composition (fluorometric measurement of advanced glycation end products (AGEs) is shown), (D) trabecular morphology (trabeculae shaped as either rods or plates) and orientation (axial, oblique and transversely aligned trabeculae). Mechanical characterization may include (E) high-resolution finite element models or (F) characterization of microdamage in the trabecular microstructure.

1.7. Identification and Measurement of Bone Remodeling Events

Bone formation is traditionally measured using two-dimensional dynamic histomorphometry. In dynamic histomorphometry, a florescent marker (tetracycline, calcein, xylenol orange) is injected into an animal, *in vivo*. The agent will accumulate at regions of newly formed bone matrix at locations where bone formation is active. Another agent is then injected some time later. Bone from the subject is then sectioned

for analysis and the fluorescent labels appear as thin fluorescent bands in two-dimensional histological sections. Measurements, such as the percentage of bone surface with fluorescent labels and mineral apposition rate (thickness of mineralized bone deposited/time in between labels) are made. The amount of bone resorption can be quantified in two-dimensions in histology sections by determining the percentage of bone surfaces with current or prior resorption (surfaces with irregular topography (Figure 1.3B) and is expressed as the percent eroded surface (ES/BS).

While two-dimensional approaches described above provide valuable information about bone remodeling, they cannot describe the number or size of remodeling events [51, 52]. Three-dimensional dynamic histomorphometry using a three-dimensional data set obtained from serial milling (described in ***Chapter 2***) allows for the measurements of the size and number of resorption cavities and bone formation events as well as three-dimensional analogs of traditional bone remodeling measurements [53].

An additional three-dimensional approach to measure bone formation and resorption is *in vivo*, serial microcomputed tomography (microCT) [54-59]. For serial microCT, animals are evaluated with high-resolution microCT (10.5 μm) at sequential time points. A comparison of both sets of images following three-dimensional image registration can identify and measure areas of bone formation and resorption. The approach has limited spatial resolution and is therefore only used on the extremities.

1.8. Characterization of Cancellous Bone Tissue Material Properties

Changes in bone remodeling can affect the composition of both the collagen matrix and bone mineral content in cancellous bone by altering tissue age. The size and morphology of individual hydroxyapatite particles can be measured using transmission electron microscopy and small angle X-ray scattering, and the crystallinity and texture of bone tissue can be characterized using Fourier transform infrared spectroscopy (FTIR). Bone mineral density distribution (BMDD) can be accessed in cancellous bone using quantitative microradiography, quantitative backscattered electron imaging and synchrotron radiation microCT (SrμCT) [2].

Advanced glycation end products (AGEs) are a product of non-enzymatic glycation of collagen. Pentosidine is an example of an AGE that forms cross-links between collagen fibers [60, 61]. AGEs can accumulate in bone tissue with age and have been associated with a decrease in post-yield mechanical properties of cancellous bone [62, 63]. Pentosidine can be quantified using high-perfosrmance liquid chromatography (HPLC) whereas overall AGE content can be accessed using a fluorometric assay (see Figure 1.3C) [60].

1.9. Characterization of Trabecular Microstructure

MicroCT and serial milling allow for three-dimensional analysis of trabecular microstructure. Traditional measurements of trabecular microstructure include bone volume fraction (volume of bone/ total volume including marrow space), average trabecular thickness, trabecular number, trabecular separation (distance between trabeculae), degree of anisotropy, and structure model index (SMI, an average measurement of trabecular morphology) [53, 64]. One issue that arises with traditional

measurements of trabecular microstructure is that most measurements strongly correlate with bone volume fraction (a measurement that is also related to the amount of bone mass and BMD as measured in patients). As such, traditional microstructural measurements are not aspects of bone quality and are of limited usefulness in explaining fracture risk independent of bone mass.

Measurements of the trabecular morphology and orientation can be obtained from individual trabecular segmentation (ITS, Figure 1.3D) and have been shown to indicate fracture risk, independent of BMD. Measurements made with ITS are also correlated with cancellous bone mechanical performance [65]. ITS can classify individual trabeculae as rods and plates and also determine the orientation of each trabeculae relative to the primary orientation of trabeculae (axial, oblique, transverse). Rods and plates are classified using a 3D skeletonization procedure to decompose the structure to surfaces (plates) and curves (rods) [66]. Trabeculae in cancellous bone from post-menopausal women and fracture patients have thinner trabeculae and fewer plate-like trabeculae [67, 68].

1.10. Cancellous Bone Mechanical Performance

Cancellous bone mechanical performance can be evaluated through mechanical testing or through finite element modeling.

1.10.1. Mechanical Testing of Cancellous Bone

Mechanical testing of cancellous bone can occur at multiple lengths scales to understand how different aspects of cancellous bone contribute to biomechanical performance [47]. For instance, mechanical testing using atomic force microscopy or

nanoindentation is useful for characterizing changes to mechanical properties of bone associated with nano-scale changes in bone tissue [2]. Mechanical testing of cancellous bone specimens on the scale of 5 mm using a mechanical testing machine is most appropriate to understand how changes to cancellous bone microstructure influence bone strength. Specimens of cancellous bone are glued within brass end-caps and placed in the mechanical testing machine. Loading (monotonic or cyclic) is applied in either tension or compression to create microdamage [69-71].

1.10.3. High Resolution Finite Element Models of Cancellous Bone

High resolution finite element (FE) models generated using three-dimensional images of cancellous bone allow for the estimation of bone tissue stresses and strains (Figure 1.3E). FE models of cancellous bone have shown good agreement with mechanical properties derived from mechanical testing [72, 73]. Microdamage has been observed to form preferentially in regions of high strain determined using FE models [74, 75]. FE models of cancellous bone indicate that resorption cavities act create as stress risers in bone and decrease cancellous bone strength independent of bone volume [50, 76, 77]; furthermore, a cavity with a greater depth relative to the its local trabecular thickness creates a greater geometric discontinuity and stress concentration effect compared to a more shallow cavity [52]. There is evidence from non-linear FE models that homogenous models both overestimate and underestimate tissue stresses and strains, indicating that tissue composition may play a role in where tissue stresses and strains occur [78].

1.10.2. Microdamage in Cancellous Bone

Microscopic tissue damage in bone is known as microdamage. Microdamage occurs in two primary forms: linear microcracks (50-100 μm long) and patches of submicroscopic cracks called diffuse damage [79]. The formation of microcracks is a fracture resistance mechanism to resist crack growth through a combination of intrinsic (ahead of crack tip) and extrinsic (behind crack tip) toughening mechanisms [80-83]. Microcracks allow the bone to dissipate energy through localized failure prior to overt failure [84, 85]. Still, small amounts of microdamage generated from mechanical loading will diminish cancellous bone mechanical properties [70, 71]. Microdamage accumulates *in vivo* as tissue ages [86] and accumulation of bone mineral and AGEs are expected to influence microdamage formation [87] as are stress risers in bone such as resorption cavities.

Microdamage is identified through a process of bulk staining. In non-living bone tissue, stains penetrate deep into bone tissue and deposit into cracks, Some stains, such as lead uranyl acetate (lead UA) and chelating agents like calcein, are site-specific, binding to calcium ions exposed by the cracks; other stains such as basic fuchsin are not site specific [88]. Most analyses of microdamage are done in two-dimensions using histological sections; however three-dimensional approaches now exist to observe and measure microdamage stained with fluorochrome chelating agents visualized using serial milling (Figure 1.3F) or with lead UA visualized using microCT [89-92].

1.12. Bone remodeling, Microdamage and Osteoarthritis

Bone remodeling also appears to play an important role in the early progression of osteoarthritis. Animal models indicate that increased bone remodeling in response to mechanical loading (likely to repair microdamage) is involved in a pathway that results in bone marrow lesions and eventually cartilage degeneration [93-96]. Bone marrow lesions manifest as an increase in signal intensity in water sensitive magnetic resonance imaging sequences of subchondral cancellous bone. Bone marrow lesions are early indicators of (and possible contributors to) early osteoarthritis progression [97].

1.12. Thesis Aims

In Aims 1 and 2, I determine if osteoporosis drug treatments can modify aspects of bone quality (resorptive cavity size and trabecular morphology) that are expected to influence cancellous bone biomechanical performance. In Aim 3, I examine how aspects of bone quality (resorption cavities and tissue composition) influence where microdamage forms and propagates in cancellous bone following cyclic mechanical loading. In Aim 4, I investigate how microdamage formed by *in vivo* loading of cancellous bone influences subsequent bone remodeling in an animal model.

1.12.1. Aim 1: Determine if anti-resorptive agents have the ability to regulate the size of individual resorption cavities.

Reductions in fracture risk from anti-resorptive treatments are greater than would be expected from the associated increases in bone mineral density (BMD) caused by treatment [45, 46]. Reductions in bone remodeling are believed to alter bone strength by causing reductions in the number and/or size of resorption cavities [98]. Alterations in the size of resorption cavities may change their effects as stress risers in

cancellous bone or the likelihood that a cavity will fenestrate an individual trabecula [49]. In the current study we use an animal model of established estrogen depletion and a three-dimensional dynamic bone histomorphometry approach to determine the effect of anti-resorptive treatment on: 1) the size of individual resorption cavities (including depth, breadth and volume); and 2) the size of individual bone formation events.

1.12.2. Aim 2: Determine the effects of Sclerostin Antibody treatment to transition rod-like trabeculae into plate-like trabeculae

Animal studies have shown that Scl-Ab treatment increases modeling-based bone formation while reducing bone resorption [7] leading to increases in bone mass and bone strength [99, 100]. Although increases in bone mineral density often result in increases in bone strength and resistance to fracture, many osteoporosis treatments cause reductions in fracture risk that are greater than expected from changes in bone mineral density alone [45, 46]. While anabolic treatments clearly increase bone volume fraction, they may also influence aspects of cancellous microstructure that influence bone quality [47]. In the current study, we combine ITS with three-dimensional dynamic bone histomorphometry to determine the changes in the number and size of rod-like and plate-like trabeculae in vertebral cancellous bone over an 8-week period of treatment with sclerostin antibody.

1.12.3. Aim 3: Determine the factors that influence the formation and propagation of microscopic tissue damage created by fatigue loading.

In bone, tissue level material toughness has been identified as a key mechanism in resisting osteoporosis- and age-related fractures [101]. AGEs

accumulate in bone tissue over time and have been shown to have a detrimental effect on resistance to crack growth and fracture [102-104]. Resorption cavities formed by osteoclasts are have been shown to act as stress risers in bone in FE models [50, 76, 105] and are thought to promote microdamage. Here we investigate whether sites of microdamage created by fatigue loading form and propagate preferentially around resorption cavities and/or in the regions where AGEs accumulate.

1.12.4. Aim 4: Develop a platform to study bone marrow lesions and microdamage repair by bone remodeling.

Bone marrow lesions are associated with increased risk of joint degeneration leading to total joint arthroplasty [106-108]. Bone marrow lesions have been observed in patients prior to clinical symptoms of osteoarthritis and may be a useful diagnostic tool or therapeutic target to prevent cartilage degeneration [109-112]. Biopsies of bone marrow lesions acquired at the time of total joint arthroplasty show microscopic cracks and other tissue damage [113] as well as increased bone remodeling [114], woven bone formation, and increased angiogenesis [115]. A pre-clinical model that recapitulates the pathogenesis of a bone marrow lesion would be valuable for understanding the natural history of bone marrow lesion development and progression. Here we establish an animal model of mechanically-induced bone marrow lesions. First, we determine whether the loads required to generate microdamage in subchondral cancellous bone would also create bone marrow lesions. Second, we investigate whether the regions of cancellous bone that receive cyclic loading and form bone marrow lesions would correspond with an increase in bone remodeling.

REFERENCES

[1] J.D. Currey, Bones: Structure and Mechanics, Princeton University Press, Princeton, NJ, USA, 2002.

[2] P. Fratzl, H.S. Gupta, E.P. Paschalis, P. Roschger, Structure and mechanical quality of the collagen-mineral nano-composite in bone, J. Mater. Chem. 14(14) (2004) 2115-2123.

[3] S. Weiner, H.D. Wagner, The material bone: Structure mechanical function relations, Annu. Rev. Mater. Sci. 28 (1998) 271-298.

[4] C.J. Hernandez, G.S. Beaupré, D.R. Carter, A model of mechanobiologic and metabolic influences on bone adaptation, J Rehabil Res Dev 37(2) (2000) 235-44.

[5] G.R. Mundy, Bone remodeling and its disorders, 2nd ed., Martin Dunitz Ltd, London, UK, 1999.

[6] A.G. Robling, A.B. Castillo, C.H. Turner, Biomechanical and molecular regulation of bone remodeling, Annu Rev Biomed Eng 8 (2006) 455-98.

[7] M.S. Ominsky, Q.T. Niu, C. Li, X. Li, H.Z. Ke, Tissue-level mechanisms responsible for the increase in bone formation and bone volume by sclerostin antibody, J Bone Miner Res 29(6) (2014) 1424-30.

[8] A.M. Parfitt, Misconceptions (2): turnover is always higher in cancellous than in cortical bone, Bone 30(6) (2002) 807-9.

[9] W.J. Boyle, W.S. Simonet, D.L. Lacey, Osteoclast differentiation and activation, Nature 423(6937) (2003) 337-342.

[10] H.K. Vaananen, H.B. Zhao, Osteoclast Function: Biology and Mechanisms, Elsevier Science Bv, Amsterdam, 2008.

[11] H.C. Blair, How the osteoclast degrades bone, BioEssays 20 (1998) 837-846.

[12] S.C. Manolagas, Birth and death of bone cells: Basic regulatory mechanisms and implications for the pathogenesis and treatment of osteoporosis, Endocr. Rev. 21(2) (2000) 115-137.

[13] G.H. Zhen, C.Y. Wen, X.F. Jia, Y. Li, J.L. Crane, S.C. Mears, F.B. Askin, F.J. Frassica, W.Z. Chang, J. Yao, J.A. Carrino, A. Cosgarea, D. Artemov, Q.M. Chen, Z.H. Zhao, X.D. Zhou, L. Riley, P. Sponseller, M. Wan, W.W. Lu, X. Cao, Inhibition of TGF-beta signaling in mesenchymal stem cells of subchondral bone attenuates osteoarthritis, Nat. Med. 19(6) (2013) 704-712.

[14] D.E. Hughes, A. Dai, J.C. Tiffee, H.H. Li, G.R. Mundy, B.F. Boyce, Estrogen promotes apoptosis of murine osteoclasts mediated by TGF-beta, Nat Med 2(10) (1996) 1132-6.

[15] R.G.G. Russell, Bisphosphonates: The first 40 years, Bone 49(1) (2011) 2-19.

[16] S. Harada, G.A. Rodan, Control of osteoblast function and regulation of bone mass, Nature 423(6937) (2003) 349-355.

[17] S.C. Manolagas, R.L. Jilka, Bone marrow, cytokines, and bone remodeling, The New England Journal of Medicine 332(5) (1995) 305-311.

[18] D.A. Glass, P. Bialek, J.D. Ahn, M. Starbuck, M.S. Patel, H. Clevers, M.M. Taketo, F.X. Long, A.P. McMahon, R.A. Lang, G. Karsenty, Canonical Wnt signaling

in differentiated osteoblasts controls osteoclast differentiation, Dev. Cell 8(5) (2005) 751-764.

[19] J.J. Westendorf, R.A. Kahler, T.M. Schroeder, Wnt signaling in osteoblasts and bone diseases, Gene 341 (2004) 19-39.

[20] M.B. Schaffler, O.D. Kennedy, Osteocyte signaling in bone, Curr Osteoporos Rep 10(2) (2012) 118-25.

[21] O.D. Kennedy, M.B. Schaffler, The roles of osteocyte signaling in bone, The Journal of the American Academy of Orthopaedic Surgeons 20(10) (2012) 670-1.

[22] O.D. Kennedy, D.M. Laudier, R.J. Majeska, H.B. Sun, M.B. Schaffler, Osteocyte apoptosis is required for production of osteoclastogenic signals following bone fatigue in vivo, Bone 64 (2014) 132-7.

[23] M. Gass, B. Dawson-Hughes, Preventing osteoporosis-related fractures: An overview, Am. J. Med. 119(4) (2006) 3S-11S.

[24] Bone health and osteoporosis: a report of the surgeon general, US Department of Health and Human Services, Rockville, MD, USA, 2004, Surgeon General Report.

[25] C. Cooper, L.J. Melton, 3rd, Epidemiology of osteoporosis, Trends Endocrinol Metab 3(6) (1992) 224-9.

[26] Assessment of fracture risk and its application to screening for postmenopausal osteoporosis, World Health Organization, Geneva, Switzerland, 1994, WHO Technical Report, 843.

[27] P. Roschger, E.P. Paschalis, P. Fratzl, K. Klaushofer, Bone mineralization density distribution in health and disease, Bone 42(3) (2008) 456-66.

[28] O. Johnell, A. Oden, C. De Laet, P. Garnero, P.D. Delmas, J.A. Kanis, Biochemical indices of bone turnover and the assessment of fracture probability, Osteoporos Int 13(7) (2002) 523-6.

[29] P. Garnero, Markers of bone turnover for the prediction of fracture risk, Osteoporos Int 11 Suppl 6 (2000) S55-65.

[30] B.L. Riggs, L.J. Melton, 3rd, Bone turnover matters: the raloxifene treatment paradox of dramatic decreases in vertebral fractures without commensurate increases in bone density, J Bone Miner Res 17(1) (2002) 11-4.

[31] L.J. Melton, 3rd, S. Khosla, E.J. Atkinson, W.M. O'Fallon, B.L. Riggs, Relationship of bone turnover to bone density and fractures, J Bone Miner Res 12(7) (1997) 1083-91.

[32] A.M. Parfitt, What is the normal rate of bone remodeling?, Bone 35(1) (2004) 1-3.

[33] E.F. Eriksen, B. Langdahl, A. Vesterby, J. Rungby, M. Kassem, Hormone replacement therapy prevents osteoclastic hyperactivity: A histomorphometric study in early postmenopausal women, J Bone Miner Res 14(7) (1999) 1217-21.

[34] E. Seeman, P.D. Delmas, Bone quality--the material and structural basis of bone strength and fragility, N Engl J Med 354(21) (2006) 2250-61.

[35] B. Ettinger, D.M. Black, B.H. Mitlak, R.K. Knickerbocker, T. Nickelsen, H.K. Genant, C. Christiansen, P.D. Delmas, J.R. Zanchetta, J. Stakkestad, C.C. Gluer, K. Krueger, F.J. Cohen, S. Eckert, K.E. Ensrud, L.V. Avioli, P. Lips, S.R. Cummings, E. Multiple Outcomes Raloxifene, Reduction of vertebral fracture risk in postmenopausal

women with osteoporosis treated with raloxifene - Results from a 3-year randomized clinical trial, JAMA-J. Am. Med. Assoc. 282(7) (1999) 637-645.

[36] B.L. Riggs, L.C. Hartmann, Selective estrogen-receptor modulators -- mechanisms of action and application to clinical practice, N Engl J Med 348(7) (2003) 618-29.

[37] R.G. Russell, Z. Xia, J.E. Dunford, U. Oppermann, A. Kwaasi, P.A. Hulley, K.L. Kavanagh, J.T. Triffitt, M.W. Lundy, R.J. Phipps, B.L. Barnett, F.P. Coxon, M.J. Rogers, N.B. Watts, F.H. Ebetino, Bisphosphonates: an update on mechanisms of action and how these relate to clinical efficacy, Ann N Y Acad Sci 1117 (2007) 209-57.

[38] D.E. Hughes, B.R. MacDonald, R.G. Russell, M. Gowen, Inhibition of osteoclast-like cell formation by bisphosphonates in long-term cultures of human bone marrow, J Clin Invest 83(6) (1989) 1930-5.

[39] S.T. Harris, N.B. Watts, H.K. Genant, C.D. McKeever, T. Hangartner, M. Keller, C.H. Chesnut, 3rd, J. Brown, E.F. Eriksen, M.S. Hoseyni, D.W. Axelrod, P.D. Miller, Effects of risedronate treatment on vertebral and nonvertebral fractures in women with postmenopausal osteoporosis: a randomized controlled trial. Vertebral Efficacy With Risedronate Therapy (VERT) Study Group, Jama 282(14) (1999) 1344-52.

[40] J.Y. Reginster, H.W. Minne, O.H. Sorensen, M. Hooper, C. Roux, M.L. Brandi, B. Lund, D. Ethgen, S. Pack, I. Roumagnac, R. Eastell, R. Vertebral Efficacy, Randomized trial of the effects of risedronate on vertebral fractures in women with established postmenopausal osteoporosis, Osteoporosis Int. 11(1) (2000) 83-91.

[41] A.B. Hodsman, D.C. Bauer, D.W. Dempster, L. Dian, D.A. Hanley, S.T. Harris, D.L. Kendler, M.R. McClung, P.D. Miller, W.P. Olszynski, E. Orwoll, C.K. Yuen, Parathyroid hormone and teriparatide for the treatment of osteoporosis: A review of the evidence and suggested guidelines for its use, Endocr. Rev. 26(5) (2005) 688-703.
[42] R.M. Neer, C.D. Arnaud, J.R. Zanchetta, R. Prince, G.A. Gaich, J.Y. Reginster, A.B. Hodsman, E.F. Eriksen, S. Ish-Shalom, H.K. Genant, O. Wang, B.H. Mitlak, Effect of parathyroid hormone (1-34) on fractures and bone mineral density in postmenopausal women with osteoporosis, N Engl J Med 344(19) (2001) 1434-41.
[43] J.J. Body, G.A. Gaich, W.H. Scheele, P.M. Kulkarni, P.D. Miller, A. Peretz, R.K. Dore, R. Correa-Rotter, A. Papaioannou, D.C. Cumming, A.B. Hodsman, A randomized double-blind trial to compare the efficacy of teriparatide [recombinant human parathyroid hormone (1-34)] with alendronate in postmenopausal women with osteoporosis, J Clin Endocrinol Metab 87(10) (2002) 4528-35.
[44] F. Cosman, D.B. Crittenden, J.D. Adachi, N. Binkley, E. Czerwinski, S. Ferrari, L.C. Hofbauer, E. Lau, E.M. Lewiecki, A. Miyauchi, C.A. Zerbini, C.E. Milmont, L. Chen, J. Maddox, P.D. Meisner, C. Libanati, A. Grauer, Romosozumab Treatment in Postmenopausal Women with Osteoporosis, N Engl J Med 375(16) (2016) 1532-1543.
[45] S.R. Cummings, D.B. Karpf, F. Harris, H.K. Genant, K. Ensrud, A.Z. LaCroix, D.M. Black, Improvement in spine bone density and reduction in risk of vertebral fractures during treatment with antiresorptive drugs, Am J Med 112(4) (2002) 281-9.

[46] P.D. Delmas, Z. Li, C. Cooper, Relationship between changes in bone mineral density and fracture risk reduction with antiresorptive drugs: some issues with meta-analyses, J Bone Miner Res 19(2) (2004) 330-7.

[47] C.J. Hernandez, T.M. Keaveny, A biomechanical perspective on bone quality, Bone 39(6) (2006) 1173-81.

[48] B.L. Riggs, L.J. Melton, The Worldwide Problem of Osteoporosis - Insights Afforded by Epidemiology, Bone 17(5) (1995) S505-S511.

[49] C.J. Hernandez, How can bone turnover modify bone strength independent of bone mass?, Bone 42(6) (2008) 1014-20.

[50] C.J. Hernandez, A. Gupta, T.M. Keaveny, A biomechanical analysis of the effects of resorption cavities on cancellous bone strength, J Bone Miner Res 21(8) (2006) 1248-55.

[51] E.M. Hauge, L. Mosekilde, F. Melsen, Stereological considerations concerning the measurement of individual osteoid seams and resorption cavities, Bone Miner 26(1) (1994) 89-90.

[52] M.G. Goff, C.R. Slyfield, S.R. Kummari, E.V. Tkachenko, S.E. Fischer, Y.H. Yi, M.G. Jekir, T.M. Keaveny, C.J. Hernandez, Three-dimensional characterization of resorption cavity size and location in human vertebral trabecular bone, Bone 51(1) (2012) 28-37.

[53] C.R. Slyfield, E.V. Tkachenko, D.L. Wilson, C.J. Hernandez, Three-dimensional dynamic bone histomorphometry, J Bone Miner Res 27(2) (2012) 486-95.

[54] A.R. Altman, W.J. Tseng, C.M. de Bakker, B.K. Huh, A. Chandra, L. Qin, X.S. Liu, A closer look at the immediate trabecula response to combined parathyroid hormone and alendronate treatment, Bone 61 (2014) 149-57.

[55] A.R. Altman, C.M. de Bakker, W.J. Tseng, A. Chandra, L. Qin, X.S. Liu, Enhanced individual trabecular repair and its mechanical implications in parathyroid hormone and alendronate treated rat tibial bone, J Biomech Eng 137(1) (2015) 10.

[56] F.A. Schulte, F.M. Lambers, G. Kuhn, R. Muller, In vivo micro-computed tomography allows direct three-dimensional quantification of both bone formation and bone resorption parameters using time-lapsed imaging, Bone 48(3) (2011) 433-42.

[57] A.I. Birkhold, H. Razi, G.N. Duda, R. Weinkamer, S. Checa, B.M. Willie, Mineralizing surface is the main target of mechanical stimulation independent of age: 3D dynamic in vivo morphometry, Bone 66 (2014) 15-25.

[58] C.M. de Bakker, A.R. Altman, W.J. Tseng, M.B. Tribble, C. Li, A. Chandra, L. Qin, X.S. Liu, muCT-based, in vivo dynamic bone histomorphometry allows 3D evaluation of the early responses of bone resorption and formation to PTH and alendronate combination therapy, Bone 73 (2015) 198-207.

[59] F.M. Lambers, F.A. Schulte, G. Kuhn, D.J. Webster, R. Muller, Mouse tail vertebrae adapt to cyclic mechanical loading by increasing bone formation rate and decreasing bone resorption rate as shown by time-lapsed in vivo imaging of dynamic bone morphometry, Bone 49(6) (2011) 1340-50.

[60] D. Vashishth, Advanced Glycation End-products and Bone Fractures, IBMS Bonekey 6(8) (2009) 268-278.

[61] A.J. Bailey, R.G. Paul, L. Knott, Mechanisms of maturation and ageing of collagen, Mechanisms of Ageing and Development 106(1-2) (1998) 1-56.

[62] S.Y. Tang, A.D. Sharan, D. Vashishth, Effects of collagen crosslinking on tissue fragility, Clin Biomech (Bristol, Avon) 23(1) (2008) 122-3; author reply 124-6.

[63] S.Y. Tang, U. Zeenath, D. Vashishth, Effects of non-enzymatic glycation on cancellous bone fragility, Bone 40(4) (2007) 1144-51.

[64] M.L. Bouxsein, S.K. Boyd, B.A. Christiansen, R.E. Guldberg, K.J. Jepsen, R. Muller, Guidelines for assessment of bone microstructure in rodents using micro-computed tomography, J Bone Miner Res 25(7) (2010) 1468-86.

[65] B. Zhou, X.S. Liu, J. Wang, X.L. Lu, A.J. Fields, X.E. Guo, Dependence of mechanical properties of trabecular bone on plate-rod microstructure determined by individual trabecula segmentation (ITS), J Biomech 47(3) (2014) 702-8.

[66] X.S. Liu, P. Sajda, P.K. Saha, F.W. Wehrli, G. Bevill, T.M. Keaveny, X.E. Guo, Complete volumetric decomposition of individual trabecular plates and rods and its morphological correlations with anisotropic elastic moduli in human trabecular bone, J Bone Miner Res 23(2) (2008) 223-35.

[67] M.D. Walker, X.S. Liu, B. Zhou, S. Agarwal, G. Liu, D.J. McMahon, J.P. Bilezikian, X.E. Guo, Premenopausal and postmenopausal differences in bone microstructure and mechanical competence in Chinese-American and white women, J Bone Miner Res 28(6) (2013) 1308-18.

[68] E.M. Stein, A. Kepley, M. Walker, T.L. Nickolas, K. Nishiyama, B. Zhou, X.S. Liu, D.J. McMahon, C. Zhang, S. Boutroy, F. Cosman, J. Nieves, X.E. Guo, E. Shane,

Skeletal structure in postmenopausal women with osteopenia and fractures is characterized by abnormal trabecular plates and cortical thinning, J Bone Miner Res 29(5) (2014) 1101-9.

[69] T.M. Keaveny, E.F. Wachtel, D.L. Kopperdahl, Mechanical behavior of human trabecular bone after overloading, J Orthop Res 17 (1999) 346-53.

[70] F.M. Lambers, A.R. Bouman, C.M. Rimnac, C.J. Hernandez, Microdamage caused by fatigue loading in human cancellous bone: relationship to reductions in bone biomechanical performance, PLoS One 8(12) (2013) e83662.

[71] C.J. Hernandez, J. Widjaja, F.M. Lambers, C. Chapa, T.M. Nguyen, S.M. Kowtha, N.G. Halarnkar, C.M. Rimnac, Quantitative Relationships Between The Amount of Microdamage and Reductions in Cancellous Bone Stiffness and Strength, 60th Annual Meeting of the Orthopaedic Research Society, New Orleans, LA, USA, 2014, p. 156.

[72] H.H. Bayraktar, T.M. Keaveny, Mechanisms of uniformity of yield strains for trabecular bone, J Biomech 37(11) (2004) 1671-8.

[73] E.F. Morgan, H.H. Bayraktar, O.C. Yeh, S. Majumdar, A. Burghardt, T.M. Keaveny, Contribution of inter-site variations in architecture to trabecular bone apparent yield strains, J Biomech 37(9) (2004) 1413-20.

[74] M.G. Goff, F.M. Lambers, R.M. Sorna, T.M. Keaveny, C.J. Hernandez, Finite element models predict the location of microdamage in cancellous bone following uniaxial loading, J Biomech 48(15) (2015) 4142-8.

[75] R. Herblum, M. Beek, C.M. Whyne, muFEA successfully exhibits higher stresses and strains in microdamaged regions of whole vertebrae, J Orthop Res 31(10) (2013) 1653-60.

[76] S.K. Easley, M.T. Chang, D. Shindich, C.J. Hernandez, T.M. Keaveny, Biomechanical effects of simulated resorption cavities in trabecular bone across a wide range of bone volume fraction, J Bone Miner Res Submitted (2012).

[77] L.M. McNamara, J.C. van der Linden, H. Weinans, P.J. Prendergast, Stress-concentrating effect of resorption lacunae in trabecular bone, J Biomech 39(4) (2006) 734-41.

[78] G.A. Renders, L. Mulder, L.J. van Ruijven, G.E. Langenbach, T.M. van Eijden, Mineral heterogeneity affects predictions of intratrabecular stress and strain, J Biomech 44(3) (2011) 402-7.

[79] Z. Seref-Ferlengez, J. Basta-Pljakic, O.D. Kennedy, C.J. Philemon, M.B. Schaffler, Structural and mechanical repair of diffuse damage in cortical bone in vivo, J Bone Miner Res 29(12) (2014) 2537-44.

[80] R.K. Nalla, J.H. Kinney, R.O. Ritchie, Mechanistic fracture criteria for the failure of human cortical bone, Nat Mater 2(3) (2003) 164-8.

[81] K.J. Koester, J.W. Ager, 3rd, R.O. Ritchie, The true toughness of human cortical bone measured with realistically short cracks, Nat Mater 7(8) (2008) 672-7.

[82] M.E. Launey, M.J. Buehler, R.O. Ritchie, On the Mechanistic Origins of Toughness in Bone, Annu. Rev. Mater. Res. 40(1) (2010) 25-53.

[83] E.A. Zimmermann, E. Schaible, H. Bale, H.D. Barth, S.Y. Tang, P. Reichert, B. Busse, T. Alliston, J.W. Ager, R.O. Ritchie, Age-related changes in the plasticity and toughness of human cortical bone at multiple length scales, Proc. Natl. Acad. Sci. USA 108(35) (2011) 14416-14421.

[84] R.O. Ritchie, How does human bone resist fracture?, in: M. Zaidi (Ed.), Skeletal Biology and Medicine, Blackwell Publishing, Oxford, 2010, pp. 72-80.

[85] D. Vashishth, J.C. Behiri, W. Bonfield, Crack growth resistance in cortical bone: concept of microcrack toughening, J. Biomech. 30(8) (1997) 763-9.

[86] D. Vashishth, J. Koontz, S.J. Qiu, D. Lundin-Cannon, Y.N. Yeni, M.B. Schaffler, D.P. Fyhrie, In vivo diffuse damage in human vertebral trabecular bone, Bone 26 (2000) 147-152.

[87] Z. Seref-Ferlengez, O.D. Kennedy, M.B. Schaffler, Bone microdamage, remodeling and bone fragility: how much damage is too much damage?, Bonekey Rep 4 (2015) 644.

[88] T.C. Lee, S. Mohsin, D. Taylor, R. Parkesh, T. Gunnlaugsson, F.J. O'Brien, M. Giehl, W. Gowin, Detecting microdamage in bone, J Anat 203(2) (2003) 161-72.

[89] S.Y. Tang, D. Vashishth, A non-invasive in vitro technique for the three-dimensional quantification of microdamage in trabecular bone, Bone 40(5) (2007) 1259-64.

[90] R.F. Bigley, M. Singh, C.J. Hernandez, G.J. Kazakia, R.B. Martin, T.M. Keaveny, Validity of serial milling-based imaging system for microdamage quantification, Bone 42(1) (2008) 212-5.

[91] D.B. Burr, M. Hooser, Alterations to the en bloc basic fuchsin staining protocol for the demonstration of microdamage produced in vivo, Bone 17(4) (1995) 431-3.

[92] T.C. Lee, T.L. Arthur, L.J. Gibson, W.C. Hayes, Sequential labelling of microdamage in bone using chelating agents, J Orthop Res 18(2) (2000) 322-5.

[93] A.J. Ramme, M. Lendhey, J.G. Raya, T. Kirsch, O.D. Kennedy, A novel rat model for subchondral microdamage in acute knee injury: a potential mechanism in post-traumatic osteoarthritis., Osteoarthritis Cartilage 24(10) (2016) 1776-85.

[94] D.B. Burr, E.L. Radin, Microfractures and microcracks in subchondral bone: are they relevant to osteoarthrosis?, Rheum. Dis. Clin. North Am. 29(4) (2003) 675-685.

[95] D.B. Burr, M.A. Gallant, Bone remodelling in osteoarthritis, Nat. Rev. Rheumatol. 8(11) (2012) 665-673.

[96] E.L. Radin, R.B. Martin, D.B. Burr, B. Caterson, R.D. Boyd, C. Goodwin, Effects of mechanical loading on the tissues of the rabbit knee, J. Orthop. Res. 2(3) (1984) 221-34.

[97] L. Xu, D. Hayashi, F.W. Roemer, D.T. Felson, A. Guermazi, Magnetic resonance imaging of subchondral bone marrow lesions in association with osteoarthritis, Semin Arthritis Rheum 42(2) (2012) 105-18.

[98] A.M. Parfitt, High bone turnover is intrinsically harmful: two paths to a similar conclusion. The Parfitt view, J Bone Miner Res 17(8) (2002) 1558-9.

[99] X. Li, M.S. Ominsky, K.S. Warmington, S. Morony, J. Gong, J. Cao, Y. Gao, V. Shalhoub, B. Tipton, R. Haldankar, Q. Chen, A. Winters, T. Boone, Z. Geng, Q.T. Niu, H.Z. Ke, P.J. Kostenuik, W.S. Simonet, D.L. Lacey, C. Paszty, Sclerostin

antibody treatment increases bone formation, bone mass, and bone strength in a rat model of postmenopausal osteoporosis, J Bone Miner Res 24(4) (2009) 578-88.

[100] M.S. Ominsky, F. Vlasseros, J. Jolette, S.Y. Smith, B. Stouch, G. Doellgast, J. Gong, Y. Gao, J. Cao, K. Graham, B. Tipton, J. Cai, R. Deshpande, L. Zhou, M.D. Hale, D.J. Lightwood, A.J. Henry, A.G. Popplewell, A.R. Moore, M.K. Robinson, D.L. Lacey, W.S. Simonet, C. Paszty, Two doses of sclerostin antibody in cynomolgus monkeys increases bone formation, bone mineral density, and bone strength, J Bone Miner Res 25(5) (2010) 948-59.

[101] R.O. Ritchie, M.J. Buehler, P. Hansma, Plasticity and toughness in bone, Phys Today 62(6) (2009) 41-47.

[102] J.W. Ager, G. Balooch, R.O. Ritchie, Fracture, aging, and disease in bone, J. Mater. Res. 21(08) (2006) 1878-1892.

[103] X. Wang, X. Shen, X. Li, C. Mauli Agrawal, Age-related changes in the collagen network and toughness of bone, Bone 31(1) (2002) 1-7.

[104] D. Vashishth, G.J. Gibson, J.I. Khoury, M.B. Schaffler, J. Kimura, D.P. Fyhrie, Influence of nonenzymatic glycation on biomechanical properties of cortical bone, Bone 28(2) (2001) 195-201.

[105] J. Vanderoost, G.H. van Lenthe, The effect of resorption cavities on bone stiffness is site dependent, Comput Methods Biomech Biomed Engin 17(13) (2014) 1483-91.

[106] D.J. Hunter, W. Zhang, P.G. Conaghan, K. Hirko, L. Menashe, L. Li, W.M. Reichmann, E. Losina, Systematic review of the concurrent and predictive validity of MRI biomarkers in OA, Osteoarthritis Cartilage 19(5) (2011) 557-588.

[107] L. Xu, D. Hayashi, F.W. Roemer, D.T. Felson, A. Guermazi, Magnetic Resonance Imaging of Subchondral Bone Marrow Lesions in Association with Osteoarthritis, Semin. Arthritis Rheum. 42(2) (2012) 105-118.

[108] S.K. Tanamas, A.E. Wluka, J.P. Pelletier, J.M. Pelletier, F. Abram, P.A. Berry, Y.Y. Wang, G. Jones, F.M. Cicuttini, Bone marrow lesions in people with knee osteoarthritis predict progression of disease and joint replacement: a longitudinal study, Rheumatology 49(12) (2010) 2413-2419.

[109] L. Sharma, M. Nevitt, M. Hochberg, A. Guermazi, F.W. Roemer, M. Crema, C. Eaton, R. Jackson, K. Kwoh, J. Cauley, O. Almagor, J.S. Chmiel, Clinical significance of worsening versus stable preradiographic MRI lesions in a cohort study of persons at higher risk for knee osteoarthritis, Ann. Rheum. Dis. 75(9) (2016) 1630-6.

[110] F.J. Baranyay, Y. Wang, A.E. Wluka, D.R. English, G.G. Giles, R.O. Sullivan, F.M. Cicuttini, Association of bone marrow lesions with knee structures and risk factors for bone marrow lesions in the knees of clinically healthy, community-based adults, Semin Arthritis Rheum 37(2) (2007) 112-8.

[111] E. Guymer, F. Baranyay, A.E. Wluka, F. Hanna, R.J. Bell, S.R. Davis, Y. Wang, F.M. Cicuttini, A study of the prevalence and associations of subchondral bone marrow lesions in the knees of healthy, middle-aged women, Osteoarthritis Cartilage 15(12) (2007) 1437-42.

[112] D.T. Felson, M.J. Parkes, E.J. Marjanovic, M. Callaghan, A. Gait, T. Cootes, M. Lunt, J. Oldham, C.E. Hutchinson, Bone marrow lesions in knee osteoarthritis change in 6-12 weeks, Osteoarthritis Cartilage 20(12) (2012) 1514-1518.

[113] M.S. Taljanovic, A.R. Graham, J.B. Benjamin, A.F. Gmitro, E.A. Krupinski, S.A. Schwartz, T.B. Hunter, D.L. Resnick, Bone marrow edema pattern in advanced hip osteoarthritis: quantitative assessment with magnetic resonance imaging and correlation with clinical examination, radiographic findings, and histopathology, Skeletal Radiol 37(5) (2008) 423-31.

[114] M. Zanetti, E. Bruder, J. Romero, J. Hodler, Bone marrow edema pattern in osteoarthritic knees: Correlation between MR imaging and histologic findings, Radiology 215(3) (2000) 835-840.

[115] M. Shabestari, J. Vik, J.E. Reseland, E.F. Eriksen, Bone marrow lesions in hip osteoarthritis are characterized by increased bone turnover and enhanced angiogenesis, Osteoarthritis Cartilage 24(10) (2016) 1745-52.

CHAPTER 2
ANTI-RESORPTIVE AGENTS REDUCE THE SIZE OF RESORPTION CAVITIES: A THREE-DIMENSIONAL DYNAMIC BONE HISTOMORPHOMETRY STUDY

The following chapter was published in Bone in 2013 in Volume 57(1), pgs. 277-283. The article is titled “Anti-resorptive agents reduce the size of resorption cavities: A three-dimensional dynamic bone histomorphometry study” by Matheny JB, Slyfield CR, Tkachenko EV, Lin I, Ehlert KM, Tomlinson RE, Wilson DL, and Hernandez CJ and is reprinted here with permission of Elsevier. The animal work in the study described was performed under the approval of the Case Western Reserve University IACUC.

2.1. Abstract

Alterations in resorption cavities and bone remodeling events during anti-resorptive treatment are believed to contribute to reductions in fracture risk. Here, we examine changes in the size of individual remodeling events associated with treatment with a selective estrogen receptor modulator (raloxifene) or a bisphosphonate (risedronate). Adult female rats (6 months of age) were submitted to ovariectomy (n = 17) or sham surgery (SHAM, n = 5). One month after surgery, the ovariectomized animals were separated into three groups: untreated (OVX, n = 5), raloxifene treated (OVX + Ral, n = 6) and risedronate treated (OVX + Ris, n = 6). At 10 months of age, the lumbar vertebrae were submitted to three-dimensional dynamic bone histomorphometry to examine the size (depth, breadth and volume) of individual resorption cavities and formation events. Maximum resorption cavity depth did not differ between the SHAM (23.66 ± 1.87 μm, mean ± SD) and OVX (22.88 ± 3.69 μm) groups but was smaller in the OVX + Ral (14.96 ± 2.30 μm) and OVX + Ris (14.94 ± 2.70 μm) groups ($p < 0.01$). Anti-resorptive treatment was associated with reductions in the surface area of resorption cavities and the volume occupied by each resorption cavity ($p < 0.01$ each). The surface area and volume of individual formation events (double-labeled events) in the OVX + Ris group were reduced as compared to other groups ($p < 0.02$). Raloxifene treated animals showed similar amounts of bone remodeling (ES/BS and dLS/BS) compared to sham-operated controls but smaller cavity size (depth, breadth and volume). The current study shows that anti-resorptive agents influence the size of resorption cavities and individual remodeling events and that the effect of anti-

resorptives on individual remodeling events may not always be directly related to the degree of suppression of bone remodeling.

2.2. Introduction

Anti-resorptive agents are the most commonly used type of pharmacological treatment for osteoporosis. Reductions in fracture risk from anti-resorptive treatments, however, are greater than would be expected from the associated increases in bone mineral density (BMD) caused by treatment [1, 2].The causes for the disproportionate reduction in fracture risk associated with anti-resorptive treatment are not known but are commonly attributed to reductions in the amount of bone remodeling in the body. Reductions in bone remodeling are believed to alter bone strength by causing reductions in the number and/or size of resorption cavities [3].

Reductions in bone turnover caused by anti-resorptive agents may occur through a reduction in the number of remodeling events, a reduction in the size of individual remodeling events (depth, breadth) or both. Alterations in the number and size of resorption cavities may change their effects as stress risers in cancellous bone or increase the likelihood that a remodeling event will fenestrate individual trabecula [4]. Traditional, two-dimensional bone histomorphometry does not differentiate between a reduction in the number of individual remodeling events and a reduction in the size of individual remodeling events, but differences in number and size represent distinct differences in bone biomechanics [4, 5].

There are differences among anti-resorptive treatments that have the potential to alter bone biomechanical performance. Allen and colleagues found that dogs treated with raloxifene showed greater increases in vertebral bone strength per unit bone mineral density than untreated animals or animals treated with more potent anti-resorptive agents (alendronate) [6]. That raloxifene was associated with increased

bone strength per unit BMD as compared to animals with greater rates of bone turnover (untreated controls) as well as animals with less bone turnover (alendronate treated) suggests that the biomechanical effects of anti-resorptive treatments may differ, independent of BMD and the degree to which they reduce bone turnover. Although changes in tissue material properties are likely a contributor to changes in biomechanical properties independent of BMD, alterations in the size of resorption cavities/remodeling events may also contribute to changes in cancellous bone biomechanics [7].

Studies using two-dimensional histomorphometry have reported that anti-resorptive treatment is associated with a reduction of resorption cavity size [8-15]. Although two-dimensional measures of average cavity depth (erosion depth, E.De) in a specimen are well established, the technique has been criticized and has been limited to a few practitioners [16]. Measures of the surface area of individual resorption cavities and formation events estimated from simple perimeter measures in two-dimensional sections violate stereological assumptions and are therefore biased [17] (see [18] for more discussion of the limitations of two-dimensional measures of resorption cavities). Recently, we applied a three-dimensional dynamic bone histomorphometry approach to the ovariectomized rat, and found that established estrogen deficiency in rats is associated with a reduction in the number of resorption cavities and formation events in vertebral cancellous bone, but not changes in the size of individual resorption cavities (including cavity width and depth) and few changes in formation event size [19]. To the authors' knowledge, no studies have used three-

dimensional imaging to assess the size of resorption cavities and formation events in animals treated with anti-resorptive agents.

Given our previous observation that the size of resorption cavities is not altered by a state of estrogen depletion (ovariectomy), we expect that a selective estrogen receptor modulator (raloxifene) will not have an effect on the size of resorption cavities. In contrast, we expect that a bisphosphonate (risedronate) will reduce the size of resorption cavities in three-dimensions because bisphosphonates have direct effects on osteoclasts. The long-term goal of the current line of investigation is to understand how changes in bone turnover influence bone biomechanics and fracture risk. In the current study we use an animal model of established estrogen depletion and a three-dimensional dynamic bone histomorphometry approach to determine the effect of anti-resorptive treatment on: 1) the size of individual resorption cavities (including depth, breadth and volume); and 2) the size of individual bone formation events.

2.3. Materials and Methods

2.3.1. Image Acquisition and Processing

A total of 22, six month old female Sprague–Dawley rats were subjected to either bilateral ovariectomy (n = 17) or sham surgery (SHAM, n = 5). After allowing bone loss for one month, the ovariectomized animals were divided into three groups: no treatment (OVX, n = 5), or three months of treatment with raloxifene (OVX + Ral, n = 6) or risedronate (OVX + Ris, n = 6, Figure 2.1). Raloxifene and risedronate were selected because they characterize two different classes of anti-resorptive treatment (SERM and bisphosphonate). Raloxifene was selected as it is the only SERM

currently used clinically for the treatment of osteoporosis, while risedronate was selected because it is a less potent anti-resorptive agent than other bisphosphonates, allowing for a more direct comparison to raloxifene. Raloxifene (Sigma-Aldrich, St. Louis, MO, USA) was dissolved in deionized water at 1 g/mL and dosed at 1.5 mg/kg, 3 × per wk. by oral gavage. Risedronate (Proctor & Gamble, Cincinnati, OH, USA) was dissolved in deionized water at 0.1 mg/mL and dosed at 5 μg/kg, 3 × per wk. by subcutaneous injection (see Figure 2.1). Dosages of raloxifene and risedronate for rats were recommended by pharmaceutical companies (Eli Lilly and Co., Indianapolis, IN, USA, Proctor & Gamble) to simulate clinical doses for the treatment of postmenopausal osteoporosis. Animals were subjected to bone formation double labeling with xylenol orange (90 mg/kg) followed by calcein (10 mg/kg) at 10 and 3 days before euthanasia. Ovariectomy was confirmed using measures of uterine mass. Animals from the SHAM and OVX groups were described in a previous publication [19]. Animal use was performed under IACUC approval.

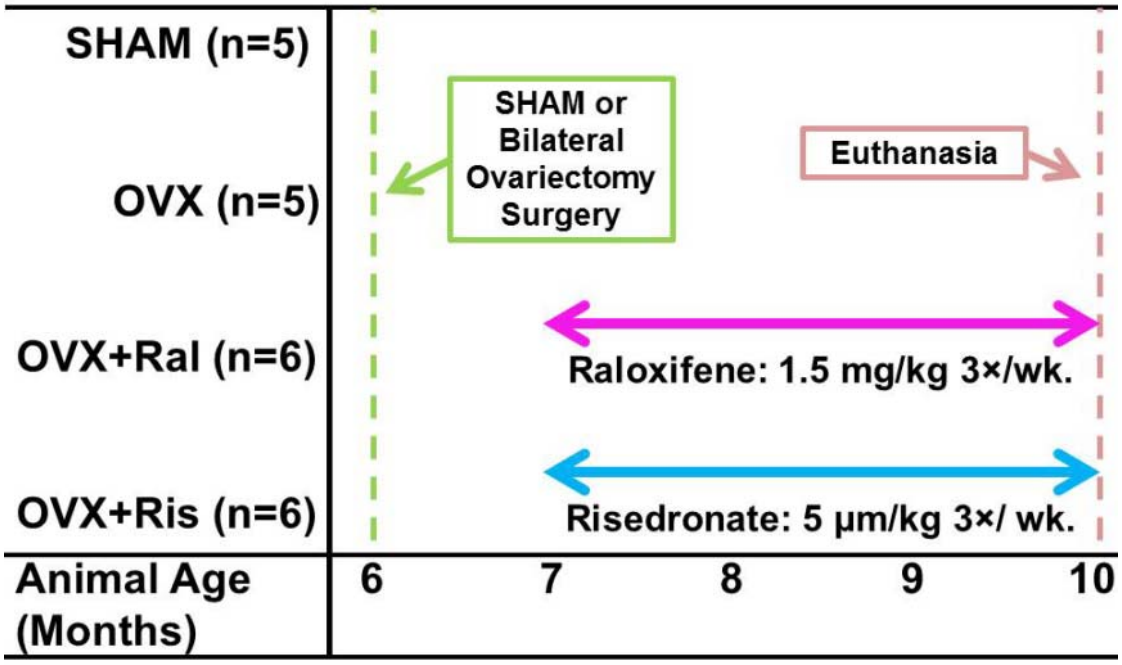

Figure 2.1. The timing of surgery and treatment in the study design are illustrated.

Following euthanasia, the lumbar vertebrae were dissected free of soft tissue. The cranial and caudal endplates of one lumbar vertebra from each animal (L3 or L4) were removed with a low-speed diamond saw and the marrow was washed out using a low pressure water jet. The undecalcified vertebrae were then embedded in opaque methyl-methacrylate and three-dimensional images of the vertebrae were collected using serial milling, as previously described [19, 20]. Serial milling involves repeatedly removing the top 5 µm from a plastic embedded specimen and collecting a mosaic of images of the newly revealed block face using epifluorescence microscopy. In the current study, serial milling was used to collect three fluorescent images (one for bone and one for each of the two bone formation labels) at a voxel size of 0.7 × 0.7 × 5.0 µm [19]. Raw images collected using serial milling occupied 290–390 GB per specimen. Pre-processing steps were performed to tile the mosaic, to crop the raw

image to the size of the specimen and to remove noise caused by fluorescent signal originating beneath the optical plane [20]. Images were manually thresholded to obtain binary images of bone and each of the two bone formation markers (xylenol orange and calcein). A region of interest more than 1 mm from the growth plate and 1 mm × 1 mm × 2 mm (height) in size was selected from the center of the vertebral body on the caudal side. The region of interest size has been shown to be sufficient for characterizing remodeling in a specimen using three-dimensional dynamic bone histomorphometry [19].

2.3.2. Three-dimensional measurements of bone remodeling

Three-dimensional measures of resorption cavities were achieved through manual tracing by a trained observer. Because manual tracing of resorption cavities in three-dimensional images is labor intensive, only a subset of all resorption cavities were examined using the following sampling strategy [18]: six independent uniform random transverse slices from each specimen were selected (each slice 300 μm from the next). An observer identified all eroded surfaces within a slice and the location of the eroded surface was recorded. A three-dimensional image of the neighborhood surrounding each identified eroded surface was displayed and the resorption cavity was traced in the three-dimensional image [21] (Figure 2.2). Our method achieved a sampling of 8–32 resorption cavities in each specimen. A three-dimensional spline was fit over the cavity to estimate the bone surface existing before resorption began to allow automated measures of cavity depth [19]. The mean and maximum depth of each cavity was determined. Cavity surface area (the area traced by the observer) and

cavity volume were also determined. Three-dimensional dynamic bone histomorphometry was used to measure the number and surface area of individual formation events (double-labeled) and to measure mineral apposition rate in the three-dimensional images (See Figure 2.3 for three-dimensional images of cancellous bone specimens with bone formation labels) [19]. Following standard sampling rules formation event size was measured only in formation events entirely within the region of interest. A total of 7–82 double-labeled formation events entirely within the region of interest were measured in each specimen. Interobserver repeatability using these techniques has been previously characterized [19-21].

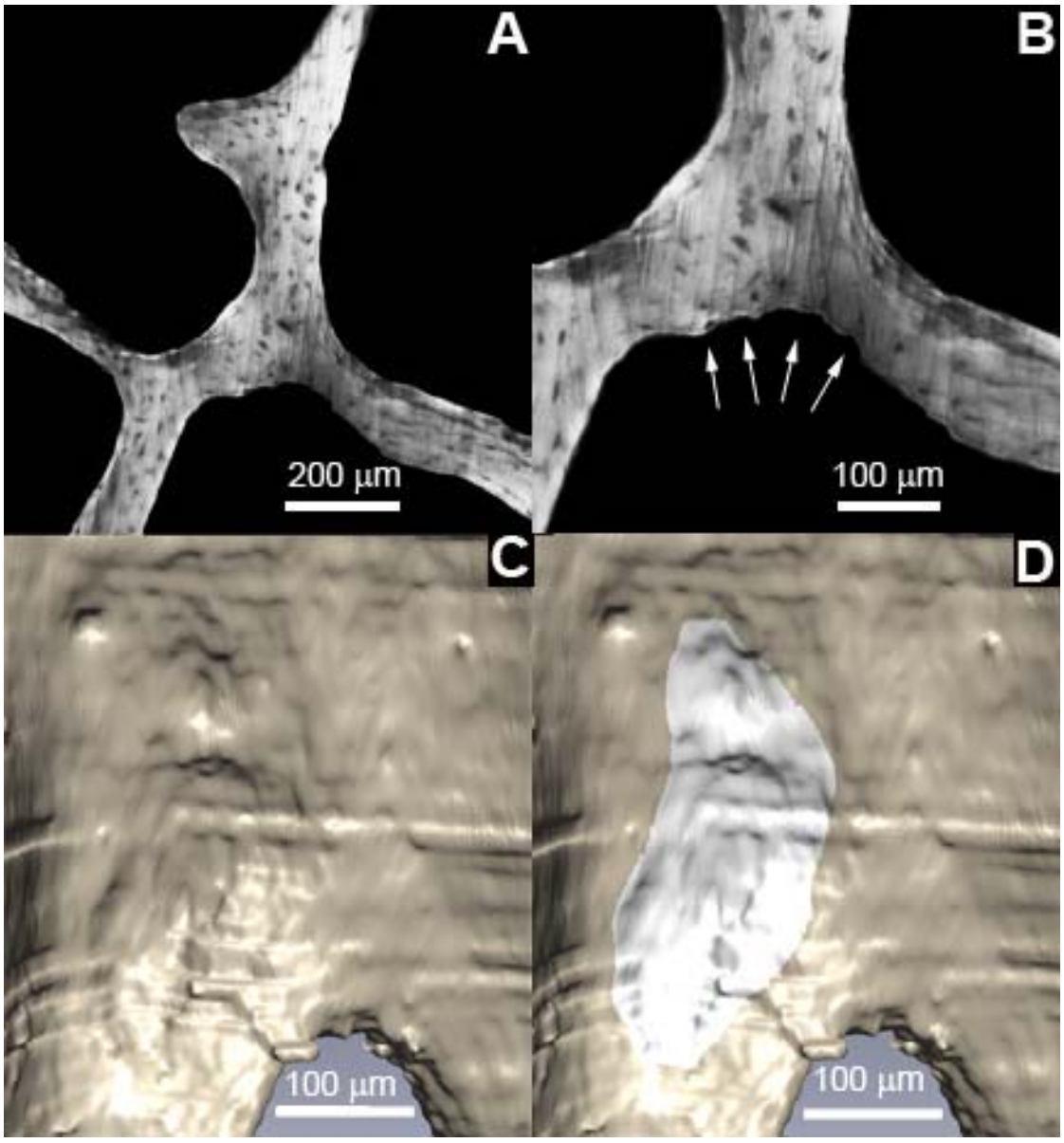

Figure 2.2. Resorption cavities were identified as eroded surfaces in gray scale images (A) after examination at 2 × magnification (B). Cavities were visualized in three-dimensions (C) and traced by a trained observer using gray scales images and the three-dimensional surface (D).

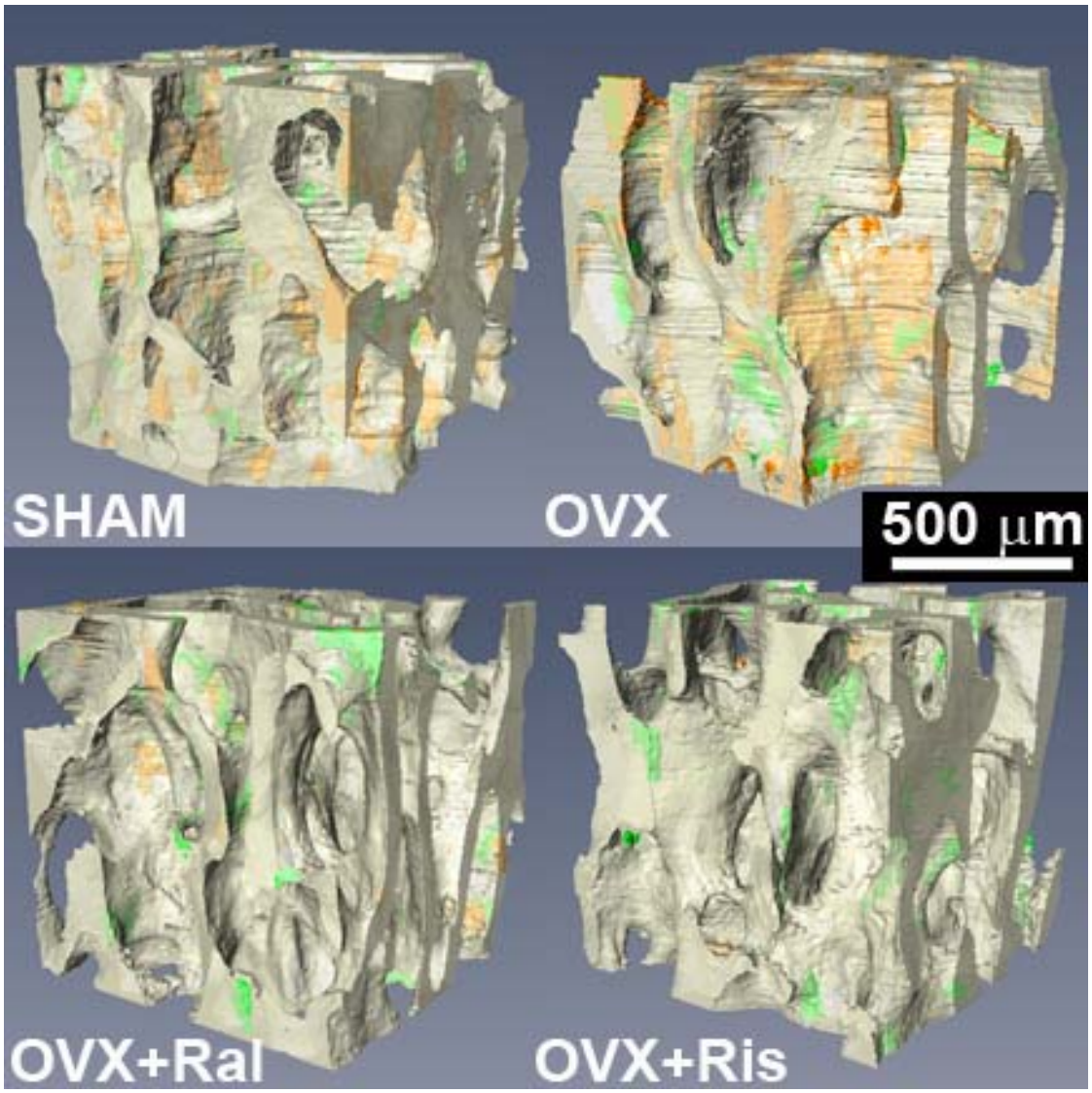

Figure 2.3. Three-dimensional images of cancellous bone from the rat lumbar vertebrae for the four groups are shown with transparency to show regions of the first bone formation label (xylenol orange) and the second formation label (calcein green).

The eroded surface in the entire specimen (ES/BS) was measured using line intersection counting in two-dimensional sections (the six transverse cross-sections, grid with lines spaced 50 μm apart). Additionally, the percent double-labeled surface (dLS/BS) was calculated from the three-dimensional images. Three-dimensional

measures of bone microarchitecture (BV/TV, Tb.Sp, etc.) were measured using BoneJ after coarsening images to 5.0 × 5.0 × 5.0 μm voxels [22].

Differences in bone microarchitecture, dLS/BS, MS/BS, BFR/BS and ES/BS among the four groups (SHAM, OVX, OVX + Ral, OVX + Ris) were identified with the non-parametric Kruskal–Wallis technique using Dunn's multiple comparisons test. Differences in formation event or resorption cavity size among groups were determined using a generalized least squares regression model to perform ANOVA including donor as a random effect to account for repeated measures within each animal (i.e. multiple formation events and cavities within each specimen). Multiple comparisons were performed using the Holm post-hoc test.

2.4. Results

At four months after surgery, ovariectomized animals showed reduced bone volume fraction and bone-specific surface as compared to sham-operated controls ($p < 0.05$). Ovariectomized animals treated with raloxifene for three months showed reduced eroded surface (ES/BS) as compared to untreated ovariectomized animals ($p = 0.04$) but no significant differences in double-labeled surface (dLS/BS). Raloxifene treatment also led to a reduction in trabecular separation compared to untreated ovariectomized animals ($p = 0.02$) (Figure 2.4). Ovariectomized animals treated with risedronate for three months had reduced ES/BS as compared to untreated ovariectomized animals ($p = 0.02$) (Figure 2.4). Risedronate treatment resulted in a reduction in double-labeled surface (dLS/BS, $p < 0.01$), mineralizing surface (MS/BS, $p = 0.02$) and bone formation rate (BFR/BS, $p = 0.05$) compared to untreated

ovariectomized animals (Table 2.2). Trends suggested that anti-resorptive treatment increased bone volume fraction as compared to ovariectomized animals but were not considered statistically significant ($p > 0.05$).

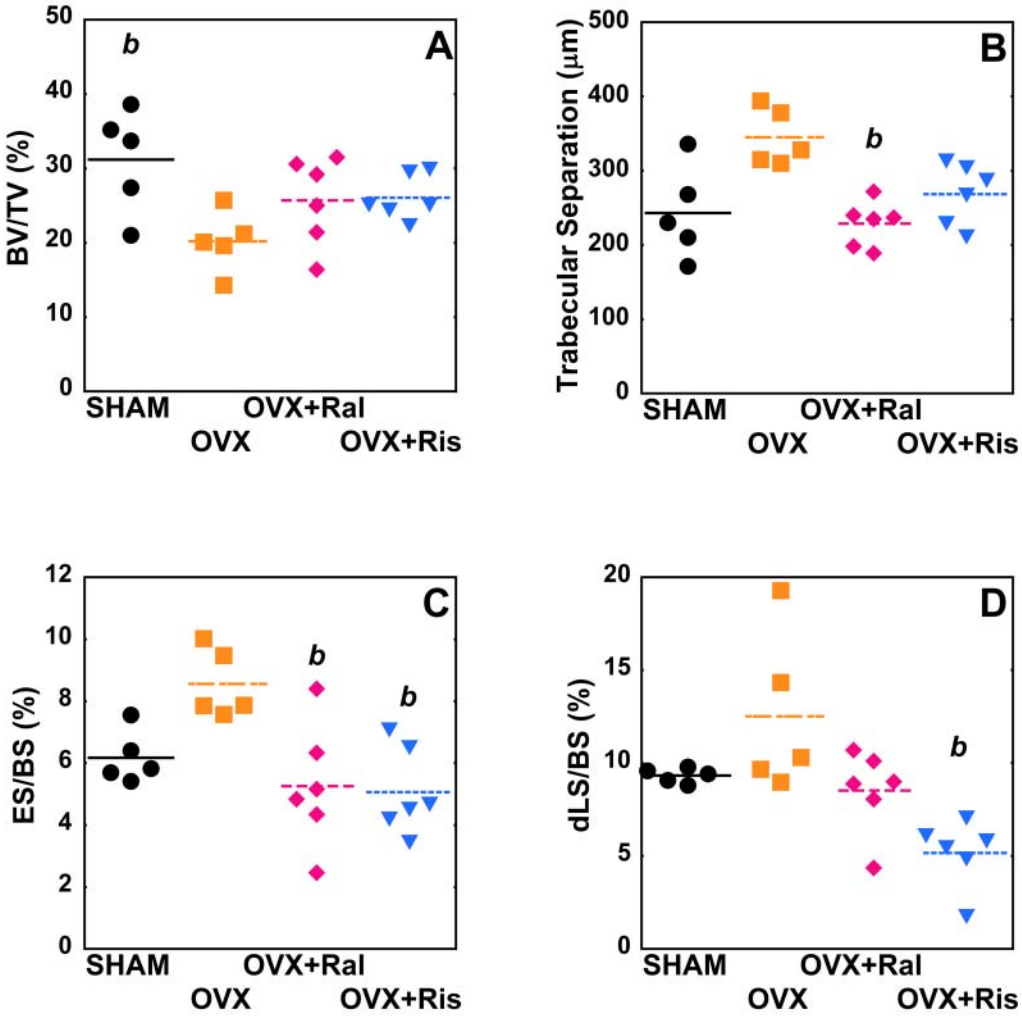

Figure 2.4. Whole specimen measures of bone microarchitecture and remodeling are shown for each of the study groups ($p < 0.05$), (A) BV/TV, (B) Tb.Sp, (C), ES/BS (D) dLS/BS. Differences between groups analyzed using Dunn's multiple comparisons test, b — $p < 0.05$ vs. OVX untreated.

Three-dimensional analysis of individual resorption cavities demonstrated no

differences in cavity surface area (BS/Cv), maximum cavity depth (Cv.De), or cavity volume (Cv.V) between untreated ovariectomized animals and sham-operated controls. Ovariectomized animals treated with raloxifene or risedronate, however, showed 34.5 – 56.8% reductions in cavity surface area, maximum cavity depth and cavity volume as compared to untreated ovariectomized animals and sham controls ($p < 0.01$) (Table 2.1, Figure 2.5A–B). Risedronate treatment was associated with reductions in mean depth per cavity as compared to both untreated ovariectomized animals and sham controls ($p < 0.01$). Raloxifene treatment was associated with reduced mean depth per cavity as compared to sham controls ($p < 0.01$). No differences in cavity morphology were observed between animals in the OVX + Ral and OVX + Ris groups (Table 2.1, Figure 2.5A-B).

Table 2.1. Static histomorphometry measures for each group are shown, mean ± SD across animals within a group, 95% CI (5th, 95th).

Measurement	SHAM (n=5)	OVX (n=5)	OVX+Ral (n=6)	OVX+Ris (n=6)
Bone volume fraction (BV/TV, %)	31.18±6.99 (22.50, 39.86)	20.18±4.08 (15.12, 25.24)	25.68±5.92 (19.47, 31.90)	26.05±3.01 (22.89, 29.21)
Bone-specific surface (BS/BV, mm^{-1})	9.60±1.64 (7.53, 11.63)	7.05±1.18 (5.60, 8.36)	9.03±1.20 (7.80, 10.27)	8.39±0.78 (7.58, 9.18)

Trabecular thickness (Tb.Th, μm)	87.52±7.57 (78.13, 96.92)	76.14±3.20 (72.17, 80.12)	75.13±14.58 (59.83, 90.43)	83.59±8.83 (74.33, 92.85)
Trabecular separation (Tb.Sp, μm)	243.01±62.92 (164.89, 321.14)	344.83±38.32 (297.25, 392.42)	228.51±30.29 (196.72, 260.29)[b]	268.74±41.10 (225.61, 311.87)
Structural modeling index (SMI)	1.16±0.27 (0.82, 1.50)	1.47±0.37 (1.02, 1.93)	1.48±0.34 (1.12, 1.83)	1.44±0.11 (1.33, 1.56)
Degree of anisotropy (DA)	0.68±0.12 (0.53, 0.83)	0.65±0.08 (0.55, 0.75)	0.72±0.06 (0.65, 0.79)	0.67±0.12 (0.54, 0.80)
*Eroded surface (ES/BS, %)	6.17±0.85 (4.78, 7.56)	8.52±1.11 (7.13, 9.91)	5.26±2.00 (3.99, 6.52)	5.06±1.41 (3.79, 6.33)[b]
†Median Maximum Cavity Depth (Cv.De, μm)	23.66±1.87 (21.33, 25.97)	22.88±3.69 (18.30, 27.47)	14.96±2.30 (12.55, 17.38)[ab]	14.94±2.70 (12.11, 17.77)[ab]
†Median Mean Cavity Depth	3.76±0.42	3.20±0.88	2.38±0.47	1.82±0.44

(μm)	(3.23, 4.28)	(2.11, 4.29)	(1.89, 2.87)[ab]	(1.36, 2.28)[ab]
†Median Cavity Surface Area (BS/Cv, 10^3 μm^2)	17.99±2.33 (15.11, 20.88)	19.76±3.02 (16.01, 23.51)	9.59±2.24 (7.24, 11.94)[ab]	8.55±2.17 (6.28, 10.82)[ab]
†Median Cavity Volume (Cv.V, 10^3 μm^3)	31.49±5.18 (25.06, 37.92)	33.92±5.87 (26.63, 41.21)	17.73±3.96 (13.58, 21.89)[ab]	15.44±3.32 (11.95, 18.92)[ab]

* - Measured in two-dimensions using line intersection.
†-Median of 8-32 cavities within a specimen.
a- $p<0.05$ vs SHAM group
b- $p<0.05$ vs OVX group

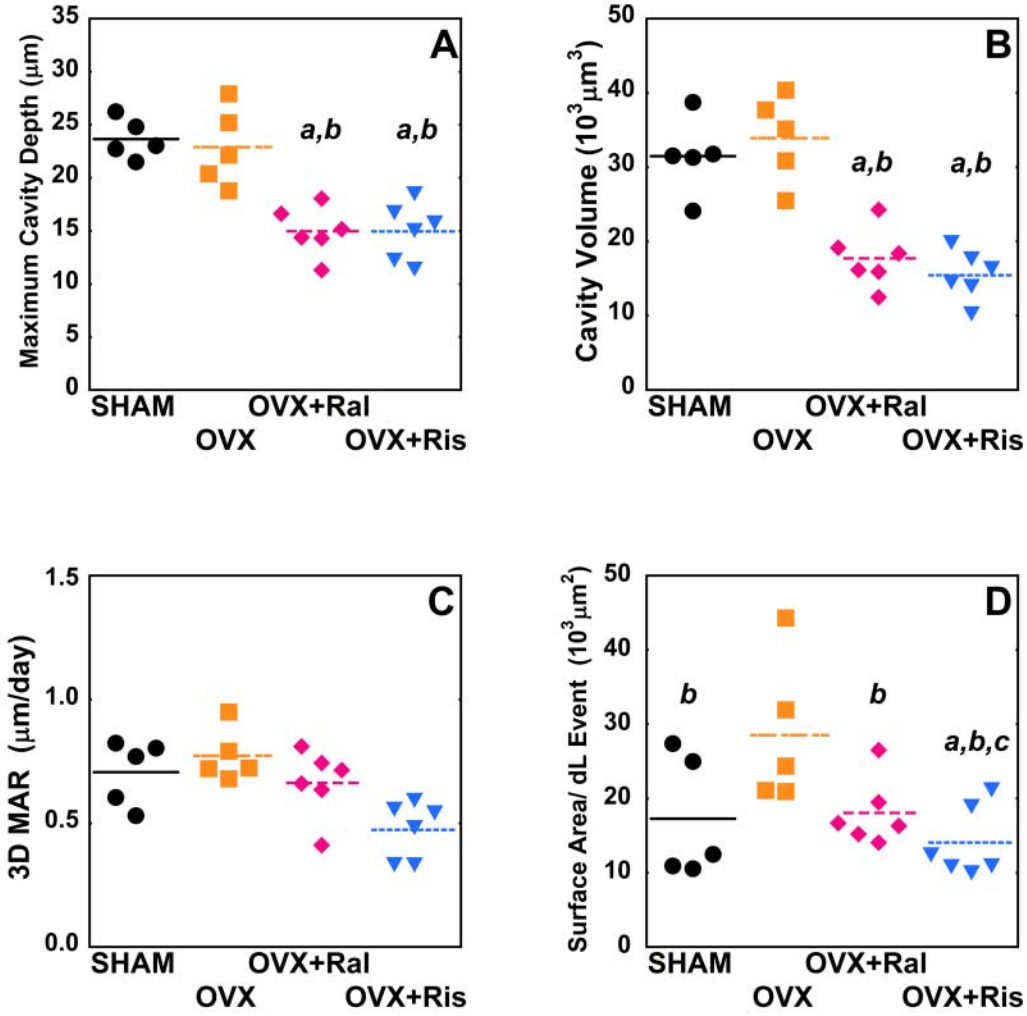

Figure 2.5. Median measurements of individual resorption cavities and formation events are shown for each of the study groups ($p < 0.05$), (A) Cv.De, (B) Cv.V, (C), 3D MAR (D) MS/dL.Ev. Statistical differences are shown based on generalized least squares regression models that include all events and donor as a random effect. a — $p < 0.05$ vs. SHAM operated, b — $p < 0.05$ vs. OVX untreated, and c — $p < 0.05$ vs. OVX + Ral.

Histograms showing the distribution of sizes of cavities and formation events are show no difference in cavity size and formation event surface area between OVX and SHAM but a shift to the left in the groups treated with anti-resorptive agents (Figure 2.6 in ***Supplementary Materials***). Surface area per double-labeled event

(MS/dL.Ev) was greater in untreated ovariectomized animals compared to all other groups ($p < 0.01$). In addition, the risedronate treated group had reduced MS/dL.Ev compared to both sham controls and the raloxifene treated group ($p < 0.02$) (Table 2.2, Figure 2.5D). Volume within each double-labeled formation event was reduced in animals treated with risedronate compared to other groups ($p < 0.01$) (Table 2.2). No differences in 3D mineral apposition rate were observed among the four groups (Figure 2.5C). No significant differences in the number of formation events per unit bone surface or in measurements of the size and number of single-labeled surfaces were observed between groups. As expected, median measures of formation event size were correlated with dLS/BS, and median measures of cavity size were correlated with ES/BS (See Figure 2.7 in ***Supplementary Materials***).

Table 2.2. Dynamic bone histomorphometry measures are shown for each group, Mean ± SD, 95% CI (5th, 95th).

Measurement	SHAM (n=5)	OVX (n=5)	OVX+Ral (n=6)	OVX+Ris (n=6)
Double-labeled surface (dLS/BS, %)	9.30±0.40 (8.84, 9.82)	12.51±4.32 (7.15, 17.88)	8.52±2.24 (6.20, 10.87)	5.16±1.83 (3.24, 7.08)[ab]
Mineralizing surface (MS/BS, %)	11.44±0.76 (10.50, 12.39)	13.89±4.61 (8.17, 19.62)	10.38±2.71 (7.54, 13.22)	8.14±1.98 (6.06, 10.22)[ab]

Single-labeled surface (sLS/BS, %)	4.23±2.19 (2.42, 6.04)	2.75±1.11 (0.95, 4.56)	3.71±2.26 (2.06, 5.36)	5.95±1.85 (4.30, 7.60)
No. of double-labeled formation events (N.dL.Ev)	59.20±33.54 (40.64, 77.76)	29.40±8.68 (10.84, 47.96)	38.50±16.16 (21.55, 55.45)	25.17±13.56 (8.22, 42.11)
No. of single-labeled formation events (N.sL.Ev)	114.00±63.52 (77.60, 150.40)	49.60±18.74 (13.20, 86.00)	77.50±29.15 (44.27, 110.73)	110.33±32.32 (77.11, 143.56)
No. of double-labeled formation events per unit bone surface (N.dL.Ev/BS, mm^{-2})	3.20±1.32 (2.29, 4.10)	2.23±0.54 (1.32, 3.14)	2.25±0.87 (1.43, 3.08)	1.63±0.98 (0.81, 2.46)
No. of single-labeled formation events per unit bone surface (N.sL.Ev/BS, mm^{-2})	6.50±3.61 (4.40, 8.60)	3.76±1.27 (1.66, 5.87)	2.25±0.87 (2.71, 6.54)	6.97±1.66 (5.05, 8.89)
††Median 3D mineral apposition rate (3D MAR, μm/day)	0.71±0.13 (0.54, 0.87)	0.77±0.11 (0.64, 0.90)	0.66±0.14 (0.52, 0.81)	0.47±0.11 (0.35, 0.59)

Bone formation rate (BFR/BS, μm/day)	0.11±0.03 (0.08, 0.15)	0.13±0.05 (0.10, 0.16)	0.09±0.04 (0.06, 0.12)	0.05±0.05 (0.02, 0.08)
††Median surface area per double-labeled event (MS/dL.Ev, 10^3 μm^2)	17.26±8.22 (7.06, 27.46)[b]	28.53±9.89 (16.25, 40.80)	18.05±4.53 (13.29, 22.80)[b]	14.05±4.77 (9.04, 19.05)[abc]
Median surface area per single-labeled event (MS/sL.Ev, 10^3 μm^2)	3.31±2.42 (3.01, 3.61)	3.98±0.41 (3.47, 4.49)	3.74±0.64 (3.08, 4.41)	4.34±0.56 (3.76, 4.93)
††Median volume per double-labeled event (V/dL.Ev, 10^3 μm^3)	80.76±41.33 (29.43, 132.08)	155.71±93.06 (40.16, 271.26)	91.74±29.20 (61.11, 122.39)	43.90±21.72 (21.11, 66.69)[abc]

††-Median of 8-109 formation events in each specimen
a- $p<0.05$ vs SHAM group
b- $p<0.05$ vs OVX group
c- $p<0.05$ vs OVX+Ral group

2.5. Discussion

Anti-resorptive agents can cause a fundamental change in the morphology of individual remodeling events, resulting in resorption cavities that are smaller in depth, volume and surface area as compared to ovariectomized animals and sham-operated controls. Furthermore, the anti-resorptive treatments examined here reduce the surface

area of individual formation events as compared to untreated ovariectomized animals. The reduction in resorption cavity size with anti-resorptive treatment may not be correlated to the reduction in the total amount of bone remodeling, because cavity size is reduced during raloxifene treatment as compared to sham-operated controls while the total amount of bone turnover (characterized by ES/BS and dLS/BS) does not appear to differ between the two.

There are a number of strengths to the current study that provide confidence in our results. First, the current study is unique in using three-dimensional dynamic bone histomorphometry to examine differences in remodeling event size among treatments and therefore achieves the size and variability of individual events rather than specimen averages. Image processing and analysis using our three-dimensional approach has been validated thoroughly in a series of previous studies [19-21]. Second, the current study examined cavities that had been formed *in vivo*. Although three-dimensional studies of resorption cavity depth and breadth have been performed on cavities formed by osteoclasts *in vitro* [23-26] such measures are limited by culture conditions that do not exactly match the conditions *in vivo*. Lastly, the current study used older animals and began anti-resorptive treatment after allowing bone loss to be established, thereby simulating the effects of treatment on a pre-existing state of osteopenia.

There are some limitations that must be considered when interpreting our results. First, we characterized the morphology of resorption cavities based on the observation of eroded surface and not on the presence of active osteoclasts, so our

results are characteristic of cancellous bone morphology but are only indirect measures of bone resorption. It is possible to achieve three-dimensional images of resorption cavities identified with tartrate resistant acid phosphatase [27], but such approaches are labor intensive and to our knowledge have only been applied to a handful of cavities. Additionally, we measured only a subset of all resorption cavities in each specimen. Hence, we could not directly determine if the number of resorption cavities was altered with treatment. In a previous study in which we traced all resorption cavities in each specimen, we found that established estrogen deficiency resulted in an increase in the number of resorption cavities but no changes in cavity size (depth, surface area) [19]. Although ES/BS was reduced by both anti-resorptive agents ($p < 0.05$), the current study does not allow us to make conclusions regarding changes in the number of resorption cavities associated with anti-resorptive treatment. However, we were able to examine all bone formation events within the region of interest. While the number of bone formation events observed varied considerably (range 7–82), it did not differ between the four groups after accounting for differences in bone surface area.

Previous studies using two-dimensional histomorphometry approaches have suggested that anti-resorptive agents cause 10–30% reductions in average cavity depth and 20–30% reductions in cavity breadth (only two studies examined cavity breadth) [9-15]. In comparison, the current study found more pronounced reductions in resorption cavity size including a 35–51% reduction in depth and reductions in resorption cavity surface area of 47–57%. To the authors' knowledge, no studies have

measured changes in the size of bone formation events following anti-resorptive treatment. The current study is the first to use three-dimensional approaches to analyze the effects of anti-resorptive agents on the surface area and volume of individual resorption cavities and formation events. In comparison to previous work the current study does not require stereology or selection of only cavities ideal for measurement (which introduces selection bias [16]).

The mechanism through which resorption cavities are reduced in size is not clear, but could be caused by changes in the number of osteoclasts at each resorption site, the amount of bone resorption by each osteoclast, the lifespan of osteoclasts at resorption sites or some combination of the three. Nitrogen containing bisphosphonates such as risedronate have been shown to reduce osteoclast function/lifespan, primarily by inhibiting GTPases that regulate osteoclast cytoskeletal rearrangement, membrane ruffling and vesicular trafficking necessary for bone resorption [28]. Recent work has shown that osteoclasts from mice deficient in Rac1 and Rac2 form smaller resorption cavities *in vitro* [26] which is consistent with the idea that risedronate treatment regulates cavity size by impairing osteoclast function. In contrast, our finding that raloxifene also leads to reductions in cavity size as compared to both SHAM and OVX animals is surprising because raloxifene is believed to act primarily as a replacement for estrogens and was therefore expected to reverse any changes in bone remodeling associated with ovariectomy. Since there was no difference in cavity size between the SHAM and OVX groups, we expected that raloxifene would not alter cavity size. There are two possible explanations for the

changes in cavity size with raloxifene: First, it is possible that the reduction in size may be related to the timing of raloxifene dosage (3 times per week) leading to differences in the concentration of raloxifene in ovariectomized animals and circulating estrogens in SHAM operated animals. Second, others have noted subtle differences in the effects of raloxifene and estrogen on bone remodeling [29, 30] and it is possible that alterations in the size of individual resorption cavities may be another difference between raloxifene and estrogen.

The current study is consistent with the idea that changes in resorption cavities may explain why reductions in fracture risk following anti-resorptive treatment are greater than expected from the associated changes in BMD. Reductions in maximum cavity depth and cavity volume associated with raloxifene and risedronate treatment are expected to reduce stress concentrations associated with resorption cavities, potentially providing benefits to bone strength independent of bone mineral density [4, 31]. Additionally, reductions in the maximum depth of resorption cavities may also reduce the likelihood that a resorption cavity disconnects or fenestrates a trabecula, helping to preserve cancellous bone microarchitecture over time. The magnitude of stress concentrations associated with resorption cavities depends on the number and size of resorption cavities, the location of the cavity within the structure (on a longitudinal trabecula vs. transverse trabecula, in a highly loaded or less loaded region of the microstructure) and local bone morphology (local trabecular thickness, plate-like vs. rod-like trabeculae, nodes in the structure, etc.) [4, 18]. Given the complex microarchitecture and load distribution within cancellous bone, additional

biomechanical analyses are required to understand the mechanical consequences of resorption cavities.

In conclusion, our findings demonstrate that existing drug treatments have the ability to regulate the size of individual resorption cavities. Regulation of the size of individual resorption cavities may be one way in which anti-resorptive agents make cancellous bone more resistant to mechanical failure. Finally, regulating resorption cavity size has the potential to alter cancellous bone biomechanical performance in a way that may not be immediately apparent from measure of overall amounts of bone turnover.

2.6 Acknowledgements

This publication was made possible by AR057362 and AR054448 from NIAMS/NIH. Its contents are solely the responsibility of the authors and do not necessarily represent the official views of the NIAMS or NIH. The authors thank Proctor & Gamble for donating risedronate used in the study. The authors thank Amanda R. Bouman for assistance in image preparation.

Authors' roles: Study design: CJH, CRS, JBM, DWL. Data Collection: JBM, CRS, EVT, IL, KME, RET. Data Analysis: JBM, IL, CJH. Drafting of the manuscript: JBM, CJH. Revising the manuscript content: JBM, DWL, CJH. Approving the final version of the manuscript: JBM, CRS, EVT, IL, KME, RET, DWL, CJH. JBM and CJH take responsibility for the integrity of the data analysis.

Conflict of interest statement: Dr. Wilson has an interest in BioInVision, Inc. which may commercialize the image acquisition/analysis approach. All other authors have no disclosures relevant to the current manuscript.

2.7. Supplemental Material

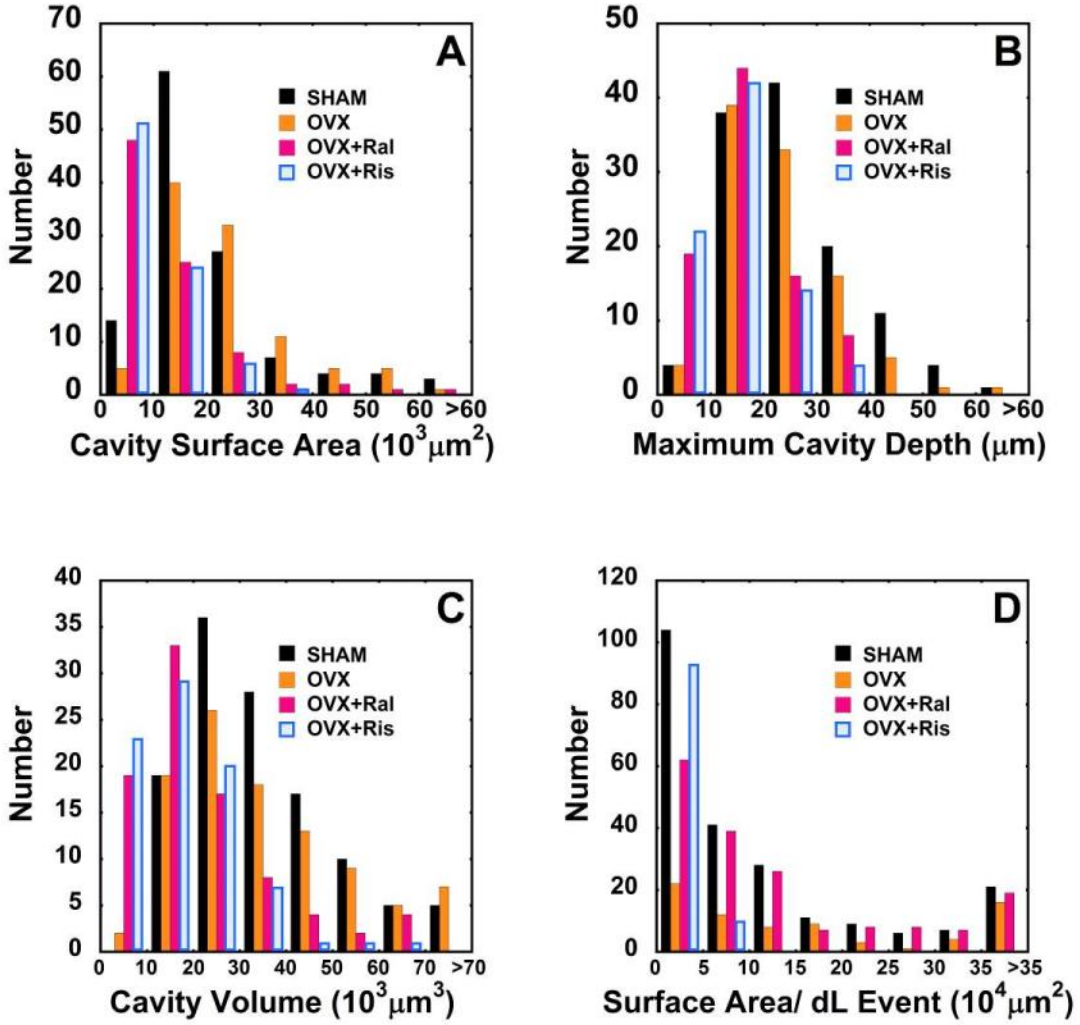

Figure 2.6. Histograms showing the distribution of sizes of cavities (A-C) and formation events (D) are shown for each of the four groups. The labels on the x-axis constitute discrete data bins. The distribution of cavity size and formation event surface area does not differ between OVX and SHAM but is shifted to the left in the groups treated with anti-resorptive agents.

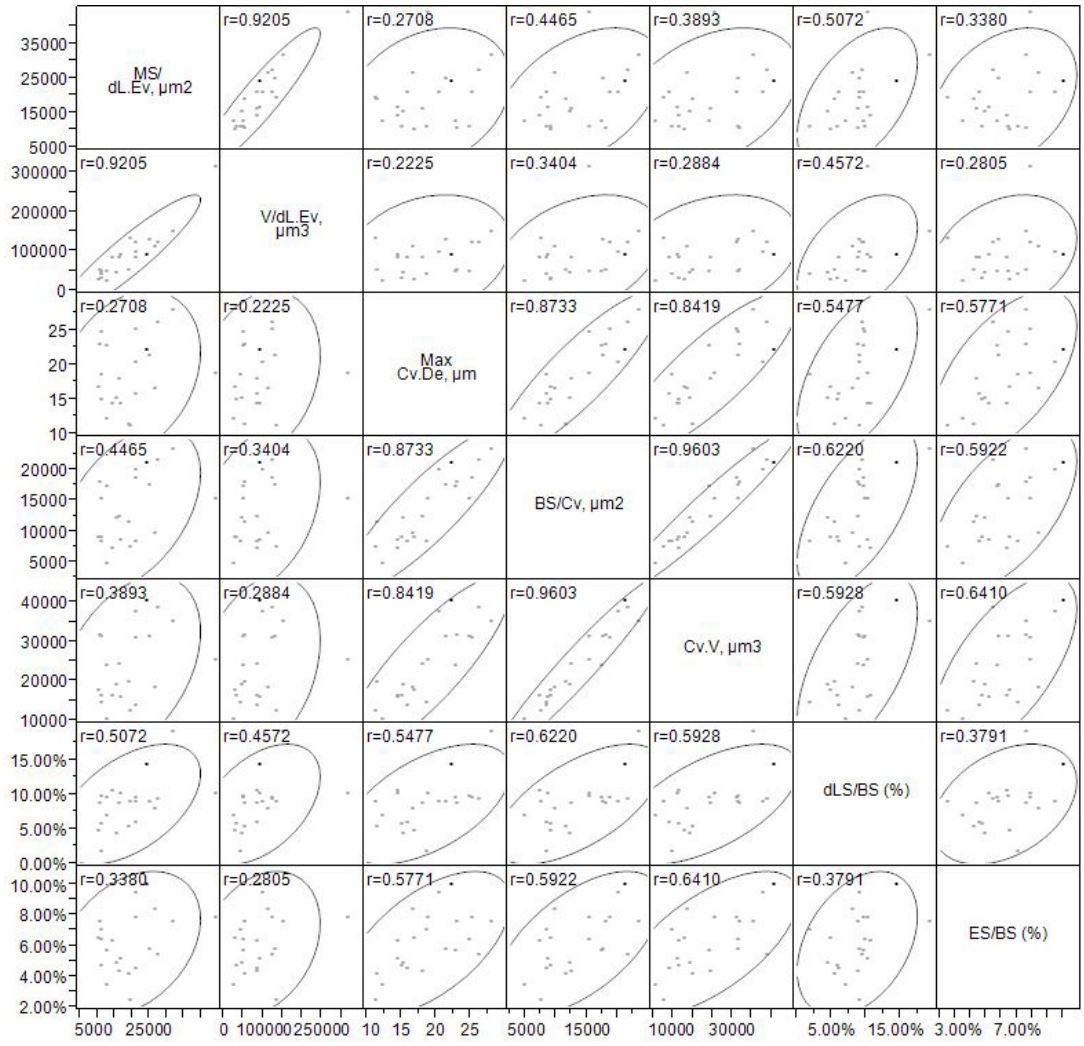

Figure 2.7. Scatterplot chart showing correlations between remodeling event size measurements and whole specimens measurements of bone remodeling are shown. Scatterplots were exported from JMP Pro 9 (For shaded ellipses, $\alpha = 0.95$).

REFERENCES

[1] S.R. Cummings, D.B. Karpf, F. Harris, H.K. Genant, K. Ensrud, A.Z. LaCroix, D.M. Black, Improvement in spine bone density and reduction in risk of vertebral fractures during treatment with antiresorptive drugs, Am J Med 112(4) (2002) 281-9.

[2] P.D. Delmas, Z. Li, C. Cooper, Relationship between changes in bone mineral density and fracture risk reduction with antiresorptive drugs: some issues with meta-analyses, J Bone Miner Res 19(2) (2004) 330-7.

[3] A.M. Parfitt, High bone turnover is intrinsically harmful: two paths to a similar conclusion. The Parfitt view, J Bone Miner Res 17(8) (2002) 1558-9.

[4] C.J. Hernandez, How can bone turnover modify bone strength independent of bone mass?, Bone 42(6) (2008) 1014-20.

[5] A.M. Parfitt, Skeletal heterogeneity and the purposes of bone remodeling, in: R. Marcus, D. Feldman, D.A. Nelson, C.J. Rosen (Eds.), Osteoporosis, Elsevier Academic Press, San Diego, CA, USA, 2008, pp. 71-92.

[6] M.R. Allen, K. Iwata, M. Sato, D.B. Burr, Raloxifene enchances vertebral mechanical properties independent of bone density, Bone 39(5) (2006) 1130-1135.

[7] M.R. Allen, D.B. Burr, Bisphosphonate effects on bone turnover, microdamage, and mechanical properties: what we think we know and what we know that we don't know, Bone 49(1) (2011) 56-65.

[8] M.E. Cohen-Solal, M.S. Shih, M.W. Lundy, A.M. Parfitt, A new method for measuring cancellous bone erosion depth: application to the cellular mechanisms of bone loss in postmenopausal osteoporosis J Bone Miner Res 6(12) (1991) 1331-1338.

[9] T. Storm, T. Steiniche, G. Thamsborg, F. Melsen, Changes in bone histomorphometry after long-term treatment with intermittent, cyclic etidronate for postmenopausal osteoporosis, J Bone Miner Res 8(2) (1993) 199-208.
[10] M.C. Monier-Faugere, R.M. Friedler, F. Bauss, H.H. Malluche, A new bisphosphonate, BM 21.0955, prevents bone loss associated with cessation of ovarian function in experimental dogs, J Bone Miner Res 8(11) (1993) 1345-55.
[11] C.D. Wright, N.J. Garrahan, M. Stanton, J.C. Gazet, R.E. Mansell, J.E. Compston, Effect of long-term tamoxifen therapy on cancellous bone remodeling and structure in women with breast cancer, J Bone Miner Res 9(2) (1994) 153-9.
[12] C. Roux, P. Ravaud, M. Cohen-Solal, M.C. de Vernejoul, S. Guillemant, B. Cherruau, P. Delmas, M. Dougados, B. Amor, Biologic, histologic and densitometric effects of oral risedronate on bone in patients with multiple myeloma, Bone 15(1) (1994) 41-9.
[13] R.W. Boyce, C.L. Paddock, J.R. Gleason, W.K. Sletsema, E.F. Eriksen, The effects of risedronate on canine cancellous bone remodeling: three-dimensional kinetic reconstruction of the remodeling site, J Bone Miner Res 10(2) (1995) 211-21.
[14] P.M. Chavassieux, M.E. Arlot, C. Reda, L. Wei, A.J. Yates, P.J. Meunier, Histomorphometric assessment of the long-term effects of alendronate on bone quality and remodeling in patients with osteoporosis, J Clin Invest 100(6) (1997) 1475-80.
[15] M.R. Allen, A.M. Erickson, X. Wang, D.B. Burr, R.B. Martin, S.J. Hazelwood, Morphological assessment of basic multicellular unit resorption parameters in dogs

shows additional mechanisms of bisphosphonate effects on bone, Calcif Tissue Int 86(1) (2010) 67-71.

[16] R.R. Recker, D.B. Kimmel, D. Dempster, R.S. Weinstein, T.J. Wronski, D.B. Burr, Issues in modern bone histomorphometry, Bone 49(5) (2011) 955-64.

[17] E.M. Hauge, L. Mosekilde, F. Melsen, Stereological considerations concerning the measurement of individual osteoid seams and resorption cavities, Bone Miner 26(1) (1994) 89-90.

[18] M.G. Goff, C.R. Slyfield, S.R. Kummari, E.V. Tkachenko, S.E. Fischer, Y.H. Yi, M.G. Jekir, T.M. Keaveny, C.J. Hernandez, Three-dimensional characterization of resorption cavity size and location in human vertebral trabecular bone, Bone 51(1) (2012) 28-37.

[19] C.R. Slyfield, E.V. Tkachenko, D.L. Wilson, C.J. Hernandez, Three-dimensional dynamic bone histomorphometry, J Bone Miner Res 27(2) (2012) 486-95.

[20] C.R. Slyfield, Jr., K.E. Niemeyer, E.V. Tkachenko, R.E. Tomlinson, G.G. Steyer, C.G. Patthanacharoenphon, G.J. Kazakia, D.L. Wilson, C.J. Hernandez, Three-dimensional surface texture visualization of bone tissue through epifluorescence-based serial block face imaging, J Microsc 236(1) (2009) 52-9.

[21] E.V. Tkachenko, C.R. Slyfield, R.E. Tomlinson, J.R. Daggett, D.L. Wilson, C.J. Hernandez, Voxel size and measures of individual resorption cavities in three-dimensional images of cancellous bone, Bone 45 (2009) 487-492.

[22] M. Doube, M.M. Klosowski, I. Arganda-Carreras, F.P. Cordelieres, R.P. Dougherty, J.S. Jackson, B. Schmid, J.R. Hutchinson, S.J. Shefelbine, BoneJ: Free and extensible bone image analysis in ImageJ, Bone 47(6) (2010) 1076-9.

[23] A. Boyde, S.J. Jones, Pitfalls in pit measurement, Calcif Tissue Int 49(2) (1991) 65-70.

[24] K. Suzuki, S. Takeyama, T. Kikuchi, S. Yamada, J. Sodek, H. Shinoda, Osteoclast responses to lipopolysaccharide, parathyroid hormone and bisphosphonates in neonatal murine calvaria analyzed by laser scanning confocal microscopy, J Histochem Cytochem 53(12) (2005) 1525-37.

[25] K. Soe, T.L. Andersen, A.S. Hobolt-Pedersen, B. Bjerregaard, L.I. Larsson, J.M. Delaisse, Involvement of human endogenous retroviral syncytin-1 in human osteoclast fusion, Bone 48(4) (2011) 837-46.

[26] S.R. Goldberg, J. Georgiou, M. Glogauer, M.D. Grynpas, A 3D scanning confocal imaging method measures pit volume and captures the role of Rac in osteoclast function, Bone 51(1) (2012) 145-52.

[27] T.L. Andersen, T.E. Sondergaard, K.E. Skorzynska, F. Dagnaes-Hansen, T.L. Plesner, E.M. Hauge, T. Plesner, J.M. Delaisse, A physical mechanism for coupling bone resorption and formation in adult human bone, Am J Pathol 174(1) (2009) 239-47.

[28] R.G. Russell, Z. Xia, J.E. Dunford, U. Oppermann, A. Kwaasi, P.A. Hulley, K.L. Kavanagh, J.T. Triffitt, M.W. Lundy, R.J. Phipps, B.L. Barnett, F.P. Coxon, M.J. Rogers, N.B. Watts, F.H. Ebetino, Bisphosphonates: an update on mechanisms of

action and how these relate to clinical efficacy, Ann N Y Acad Sci 1117 (2007) 209-57.

[29] A. Taranta, M. Brama, A. Teti, V. De luca, R. Scandurra, G. Spera, D. Agnusdei, J.D. Termine, S. Migliaccio, The selective estrogen receptor modulator raloxifene regulates osteoclast and osteoblast activity in vitro, Bone 30(2) (2002) 368-76.

[30] A. Rogers, J.A. Clowes, C.A. Pereda, R. Eastell, Different effects of raloxifene and estrogen on interleukin-1beta and interleukin-1 receptor antagonist production using in vitro and ex vivo studies, Bone 40(1) (2007) 105-10.

[31] D.W. Dempster, The contribution of trabecular architecture to cancellous bone quality, J Bone Miner Res 15(1) (2000) 20-3.

CHAPTER 3
ROMOSOZUMAB TREATMENT CONVERTS TRABECULAR RODS INTO TRABECULAR PLATES IN MALE CYNOMOLGUS MONKEYS

The following chapter was published in Calcified Tissue International in 2017 in Volume 101(1), pgs. 82-91.The article is titled “Romosozumab treatment converts trabecular rods into trabecular plates in male cynomolgus monkeys” by Matheny JB, Torres AM, Ominsky MS, and Hernandez CJ and is reprinted here with permission of Springer. All applicable international, national, and/or institutional guidelines for the care and use of animals were followed. All procedures performed in studies involving animals were in accordance with the ethical standards of the institution or practice at which the studies were conducted.

3.1. Abstract

Treatment with sclerostin antibody (romosozumab) increases bone formation while reducing bone resorption, leading to increases in bone volume and bone mineral density. Sclerostin antibody treatment may also provide beneficial changes in trabecular microarchitecture and strength that are not reflected in bone volume and density. Here we use three-dimensional dynamic histomorphometry to determine longitudinal changes in vertebral trabecular microarchitecture in adolescent male cynomolgus monkeys (4-5 years old) treated with sclerostin antibody. Animals were treated bi-weekly with either sclerostin antibody (30 mg/kg, sc, n = 6) or vehicle (n = 6) for 10 weeks. Animals were administered fluorochrome bone formation labels on days 14 and 24 (tetracycline) and on days 56 and 66 (calcein), followed by necropsy on day 70. Cylindrical specimens of cancellous bone from the 5th lumbar vertebrae were used to generate high-resolution, three-dimensional images of bone and fluorescent labels of bone formation (0.7 × 0.7 × 5.0 μm/voxel). The three-dimensional images of the bone formation labels were used to determine the bone volume formed between days 14 and 66 and the resulting alterations in trabecular microarchitecture within each bone. Treatment with sclerostin antibody resulted in a conversion of rod-like trabeculae into plate-like trabeculae at a higher rate than in vehicle treated animals ($p = 0.01$). Plate-bone volume fraction was greater in the sclerostin antibody group relative to vehicle (mean 43% vs. 30%, $p < 0.05$). Bone formation increased the thickness of trabeculae in all three trabecular orientations (axial, oblique, and transverse, $p < 0.05$). The volume of bone formed between days 14 to 66 was greater in sclerostin antibody treated groups (9.0 vs. 5.4%, $p = 0.02$), and

new bone formation due to sclerostin antibody treatment was associated with increased apparent stiffness as determined from finite element models. Our results demonstrate that increased bone formation associated with sclerostin antibody treatment increases plate-like trabecular morphology and improves mechanical performance.

3.2. Introduction

Osteoporosis is characterized by deterioration of cancellous bone microstructure, including reductions in bone volume fraction and trabecular thickness [1]. Anabolic treatments for osteoporosis have the potential to reverse bone loss and recover trabecular microstructure by causing increases in new bone formation. Romosozumab is an antibody that blocks sclerostin, a protein secreted by osteocytes that negatively regulates bone formation [2-6]. Animal studies have shown that sclerostin antibody treatment increases modeling-based bone formation while reducing bone resorption [7] leading to increases in bone mass and bone strength [2, 8]. Recent clinical studies have shown that sclerostin antibody treatment increases bone mineral density in the lumbar spine and hip [9-11] and reduces vertebral fracture risk in postmenopausal women [12]. Although increases in bone mineral density often result in increases in bone strength and resistance to fracture, many osteoporosis treatments cause reductions in fracture risk that are greater than expected from changes in bone mineral density alone [13, 14]. Possible explanations for the disproportionate change in fracture risk include alterations in bone tissue mechanical properties, cortical-trabecular density distribution and cancellous bone microarchitecture [15].

Cancellous bone microarchitecture is an aspect of bone quality that may influence fracture risk [15]. Traditional measures of cancellous bone microarchitecture include bone volume fraction, average trabecular thickness and trabecular separation [16]. However, direct enumeration and classification of individual trabeculae through Individual Trabecula Segmentation (ITS) has been shown to improve the prediction of cancellous bone strength and stiffness beyond what is possible with traditional measures [17-19]. Additionally, alterations in rod- and plate-like morphology of cancellous bone in patients has been associated with fragility fractures independent of bone mineral density determined through dual-energy X-ray absorptiometry [20]. Hence, changes in rod-like and plate-like trabecular microarchitecture have the potential to improve bone mechanical performance to a greater extent than expected from bone mineral density.

While anabolic treatments clearly increase bone volume fraction, they may also influence aspects of cancellous microstructure that influence bone quality. The number and orientation of trabeculae are known to influence biomechanical performance of cancellous bone. It is believed that once a trabecula is resorbed during age-related bone loss, it cannot be reformed by subsequent bone formation and that subsequent increases in bone density occur through thickening of existing trabeculae [21]. Finite element models suggest that increasing the number of trabeculae is more effective at increasing cancellous bone strength and stiffness than thickening existing trabeculae [21]. Differentiating between increases in the number and thickness of trabeculae is challenging because bone formation is typically assessed in two-

dimensional sections which do not display out-of-plane morphology, making it difficult to identify the presence of entirely new trabeculae [22, 23]. Three-dimensional imaging using *in vivo*, serial microcomputed tomography (serial microCT) [24-29] or high-resolution peripheral quantitative computed tomography (HR-pQCT) [30-33] has been used to evaluate changes in cancellous bone microarchitecture due to bone formation; however, both approaches have limited spatial resolution (10.5 μm for serial microCT and 82 μm or higher for HR-pQCT) and have typically been used only to study extremities. We have demonstrated a three-dimensional dynamic histomorphometry approach that provides assessment of bone formation markers in vitro [34-37], allowing for examination of changes in trabecular microarchitecture caused by bone formation that can be used on specimens from any region of the skeleton.

While cross-sectional studies have associated sclerostin antibody treatment with increased bone volume fraction [2, 7, 8, 38], there are no longitudinal studies of alterations in trabecular microarchitecture in the spine. It is not known how treatment with sclerostin antibody alters the rod and plate-like morphology of individual trabeculae in cancellous bone. Given the anabolic nature of sclerostin antibody, we hypothesize that treatment will generate sufficient bone formation to increase the total number of trabeculae or specifically increase the number of plate-like trabeculae. The long term goal of the current line of investigation is to understand how changes in bone formation and microarchitecture influence cancellous bone biomechanics and fracture risk. In the current study, we combine Individual Trabecula Segmentation

with three-dimensional dynamic bone histomorphometry to determine the changes in the number and size of rod-like and plate-like trabeculae in vertebral cancellous bone over an 8-week period of treatment with sclerostin antibody.

3.3. Materials and Methods

3.3.1 Study Design

Here we report a new analysis using tissue generated from a prior study. The study was performed under Institutional Animal Care and Use Committee approval at Charles River Laboratories (Montreal, Quebec, Canada), which has been thoroughly described elsewhere [7, 38]. All efforts were made to minimize animal suffering. Adolescent (4-5 year old) male cynomolgus monkeys (*Macaca fascicularis*) were used in the study because the monoclonal antibody (romosozumab) can only be used effectively in humans or primates. The animals were cared for in accordance to the Guide for the Care and Use of Laboratory Animals, and were maintained in Association for Assessment and Accreditation of Laboratory Animal Care International – accredited facilities in species-specific housing on a 12:12 hour light: dark cycle. The animals were socially housed indoors in environmental conditions 24°C ± 3°C, 50% ± 20% humidity, and were allowed normal physical activity. Animals were fed twice daily a certified pelleted primate diet (2050C Certified Global 20% Protein Primate Diet: Harlan Teklad) in amounts appropriate for the age and size of the animals. In addition, each animal was offered food supplements daily in any combination of the following: Golden Banana Softy®, Prima-Treat® (5 g format), fresh or dried fruit, fresh or dried vegetables and at least once weekly Prima-Foraging Crumbles® (20-25 g) as part of the environmental enrichment program. Animals had

ad libitum access to water that was treated by reverse osmosis and ultraviolet radiation.

The cynomolgus monkeys were randomly assigned to receive either sclerostin antibody (Scl-Ab, 30 mg/kg romosozumab, subcutaneous injection, n = 6) or vehicle (10 mM sodium acetate, 9% sucrose, 0.004% polysorbate 20, pH 5.2, n = 6) biweekly for 10 weeks. Animals received fluorochrome labels on days 14 and 24 (25 mg/kg tetracycline, intravenous) and on days 56 and 66 (8 mg/kg calcein, intravenous) following treatment. Romosozumab was well tolerated by the animals, and no adverse effects of sclerostin inhibition were observed. Following administration of a sedative (ketamine, intramuscular injection), monkeys were euthanized by intravenous injection of sodium pentobarbital followed by exsanguination by incision of the axillary or femoral arteries (see Figure 3.1). The fifth lumbar vertebra was stored at -20 °C.

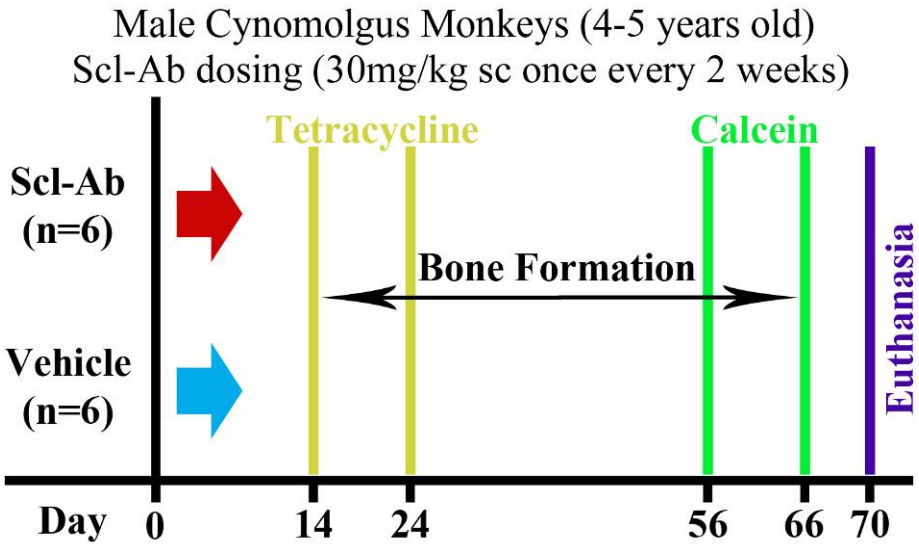

Figure 3.1. The timing of treatment and fluorochrome labeling in the study design are illustrated. Male cynomolgus monkeys were administered either sclerostin antibody (Scl-Ab, n = 6) or vehicle. Animals received fluorochrome labels on days 14 and 24 (tetracycline) and on days 56 and 66 (calcein) following treatment, and were euthanized at day 70.

3.3.2 Image Acquisition and Processing

Cylindrical specimens of cancellous bone (4 mm in height, 5 mm diameter) were obtained from the center of the 5th lumbar vertebral body. Bone marrow was removed from the specimens using a low pressure water jet and specimens were embedded undecalcified in methyl-methacrylate. Three-dimensional images of bone and fluorochrome labels were obtained using serial milling (voxel size of 0.7 × 0.7 × 5.0 μm) as described previously (See Figure 3.2) [34-36]. Serial milling uses a custom-made system that involves repeatedly removing the top 5 μm from the specimen using a computer controlled milling system (Benchman MX, Intelitek, Manchester, NH, USA) and collecting a mosaic of images from the newly revealed block face using epifluorescence microscopy. Three fluorescent images were collected of each cross-section using different filter sets: one for bone autofluorescence

(390/460 nm Ex/Em), one for tetracycline labels (390/630 nm) and one for calcein labels (480/535 nm). A manually determined global threshold was selected by a trained observer to segment bone and fluorescent labels (tetracycline and calcein). The segmentation approach has been shown to provide similar results as two-dimensional histomorphometry measurements with low inter-observer variation [34]. A cylindrical region of interest of 2 mm in height, 4 mm in diameter from the center of each specimen was used for analysis.

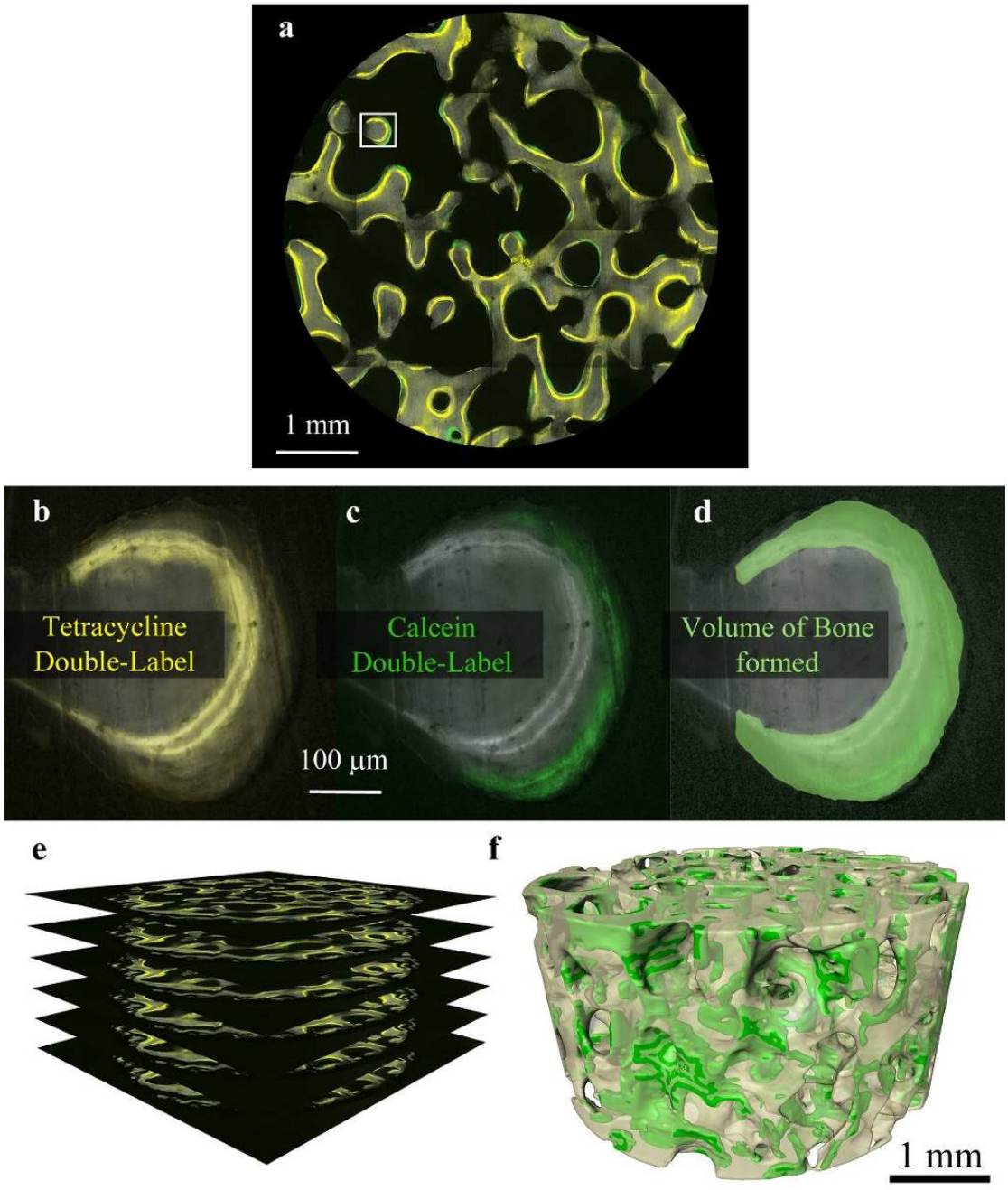

Figure 3.2. (A) A representative cross-section from a cancellous bone specimen with bone and fluorescent formation markers (tetracycline yellow (B) and calcein green (C)) obtained using serial milling at a voxel size of 0.7 × 0.7 × 5.0 µm. The two pairs of bone formation labels were merged using three-dimensional morphological closing to isolate the Formation Volume (D).Three-dimensional images of bone and bone formation were created from the collection of two-dimensional cross-sections (Formation Volume shown in green) (E-F).

3.3.3 Three-dimensional Measurements of Bone Formation

Three-dimensional dynamic bone histomorphometry differs from traditional dynamic histomorphometry in that it measures bone formation throughout the specimen and is therefore not subject to limitations associated with stereology or "label escape error," making it possible to evaluate changes in bone formation in a region of cancellous bone and longitudinal assessment of changes in bone microstructure caused by bone formation. Three-dimensional measures of bone formation were generated from the images using measurement approaches described previously [34]. Three-dimensional mineral apposition rate (3D MAR) and mineralizing surface (3D MS/BS) were determined for each of the two pairs of fluorescent labels (one pair of tetracycline and one pair of calcein) [34]. Three-dimensional bone formation rate was calculated as the mineral apposition rate multiplied by the mineralizing surface (3D BFR/BS-Tet and 3D BFR/BS-Cal). In addition to determining the bone formation indices of each of the two pairs of fluorescent labels, the entire volume of bone formed between the administration of the first tetracycline label (day 14), the last calcein label (day 66) and the bone formed between the last calcein label and euthanasia (day 70) was determined by merging all of the fluorescent labels and the adjacent surface in the three-dimensional image using morphological closing. The resulting volume was referred to as the Formation Volume (FV) and represents a direct measure of the entire volume of bone formed during the 8 week period between first and last formation labels (Figure 3.2). The changes in trabecular microarchitecture between images with and without the Formation Volume therefore approximated longitudinal changes in trabecular morphology.

3.3.4 Individual Trabecula Segmentation Based Analyses

The morphology of individual trabeculae was analyzed using Individual Trabecula Segmentation (ITS, Columbia University). Images were coarsened to 21 × 21 × 21 μm voxels to reduce computational time and to provide measures consistent with prior work [17]. Individual Trabecula Segmentation associates each voxel of bone in the image with a discrete trabecula and then characterizes the trabecular morphology (rod-like, plate-like) and orientation (axial, oblique, and transverse, See Figure 3.3) (Please see [17] for further details). The plate-bone volume fraction (pBV/TV) and rod-bone volume fraction (rBV/TV) were measured for each group along with measurements of volume fraction and trabecular thickness for each trabecular orientation (axial, oblique and transverse). To determine the longitudinal changes in rod-like and plate-like morphology and trabecular orientation caused by bone formation during the experiment, ITS was performed on the final images as well as the same images after removal of the Formation Volume. The number of trabeculae that were changed from rod-like to plate-like as a result of bone formation during the 8 week period of the experiment was then determined. Extensive analysis for entirely new trabeculae formed between the first and last formation labels was performed. Traditional three-dimensional measurements of bone (bone volume fraction (BV/TV), trabecular thickness (Tb.Th.), trabecular separation (Tb.Sp.), and structure model index (SMI) were measured using BoneJ [39].

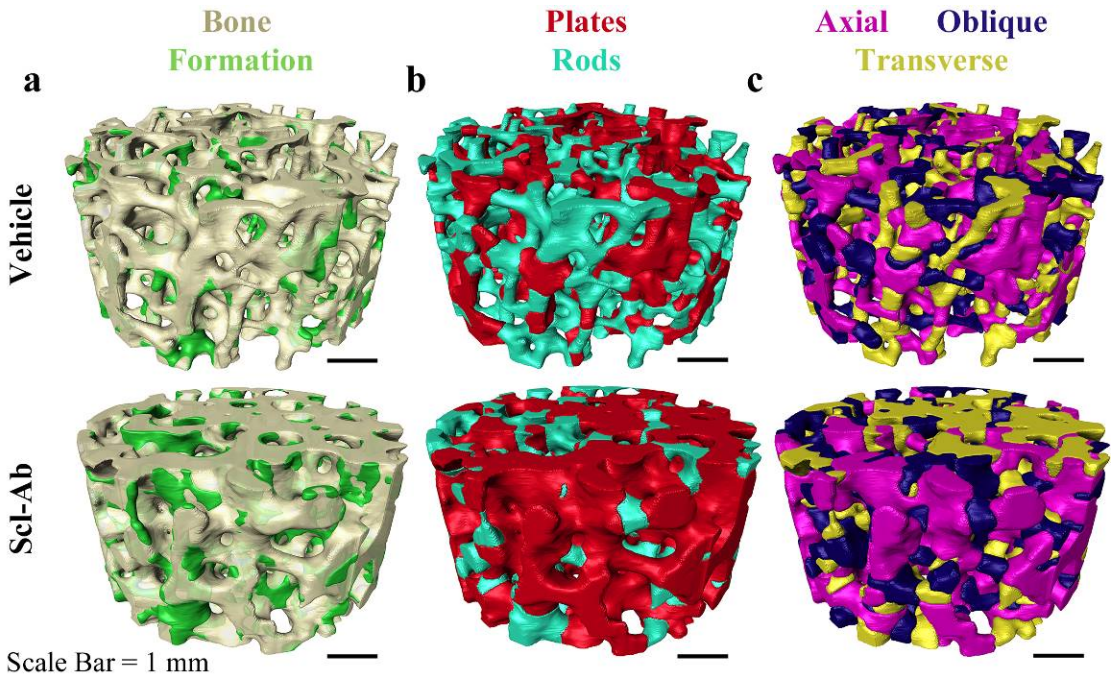

Figure 3.3. Three-dimensional images of bone formation and local trabecular morphology and orientation are shown for each group. Cancellous bone specimens from the 5th lumbar vertebra for each group are shown for (A) bone formation volume (B) plate-like and rod-like trabecular microstructure and (C) trabecular orientation for each group.

3.3.5 Serum Markers of Bone Formation

Serum osteocalcin (OC) and intact N-terminal propeptide of type 1 procollagen (P1NP), markers of bone formation, were measured using radioimmunoassay (OC: DSL-6900, Diagnostic System Laboratories country; P1NP: Intact P1NP, Orion Diagnostica) at various time points, with the day 14 time point corresponding to the initial fluorochrome label utilized for regression analysis. Please see Ominsky *et al.* for a full description of experimental procedures [8, 38] .

3.3.6 Finite Element Analysis

Linear elastic finite element models were created from three-dimensional images of the cancellous bone specimens (21-μm voxels) with and without the bone formed during the 8 weeks between formation labels. Each finite element model consisted of

0.62 - 1.69 million elements. Bone tissue was assumed to be an isotropic, linear elastic material with Young's modulus 10 GPa and Poisson's ratio of 0.3. To determine axial stiffness, an apparent compressive strain of 1% was applied to the top surface in the axial direction (z-axis), and vertical displacement on the opposite surface was fixed. To determine transverse stiffness, a cubic region of interest 2 mm in size was taken from the center of each specimen and finite element models were created with displacement applied in the transverse direction (y-axis). Apparent stress was calculated from the sum of the reaction forces on the constrained surface divided by the cross-sectional area of the surface. Apparent stiffness was calculated as the apparent stress divided by the applied apparent strain. Finite element models were implemented using Abaqus (Abaqus 6.9, Dassault Systèmes, Velizy-Villacoublay, France) with the Abaqus/Standard solver.

3.3.7 Statistical Analysis

Differences in three-dimensional measurements of bone formation, bone microarchitecture and ITS-based measurements between vehicle and sclerostin antibody treated groups were identified using two-tailed t-tests with JMP (JMP Pro 10.0.2, SAS Institute Inc., Cary, NC, USA). In addition, linear regression analyses were performed with JMP. A p-value of 0.05 was used to determine statistical significance.

3.4. Results

Over the 8 week period of the study, more rod-like trabeculae were converted to plate-like trabeculae in animals treated with sclerostin antibody (10.27 ± 3.59%,

mean ± SD) than in vehicle treated animals (4.45 ± 3.48%, p = 0.017, see Figure 3.4, Table 3.1). The volume of bone formed over the 8 week study period (Formation Volume) was 68% greater in sclerostin antibody treated animals as compared to vehicle controls (p = 0.015, See Figure 3.5A, Table 3.2). The increase in newly formed bone volume was achieved by an increase in bone formation rate (3D BFR/BS, p = 0.001) (See Figure 3.5B, Table 3.2). The increases in 3D MAR, 3D MS/BS and 3D BFR/BS due to sclerostin antibody treatment early in the study (days 14-24 observed with tetracycline) was similar to that later in the study (days 56-66, observed with calcein, Table 3.2). Additionally, serum markers of bone formation (OC and P1NP) measured two weeks following treatment were strongly correlated with the three-dimensional bone formation rate (see Figure 3.5C-D). Extensive examination of the specimens failed to provide evidence of the formation of entirely new trabeculae.

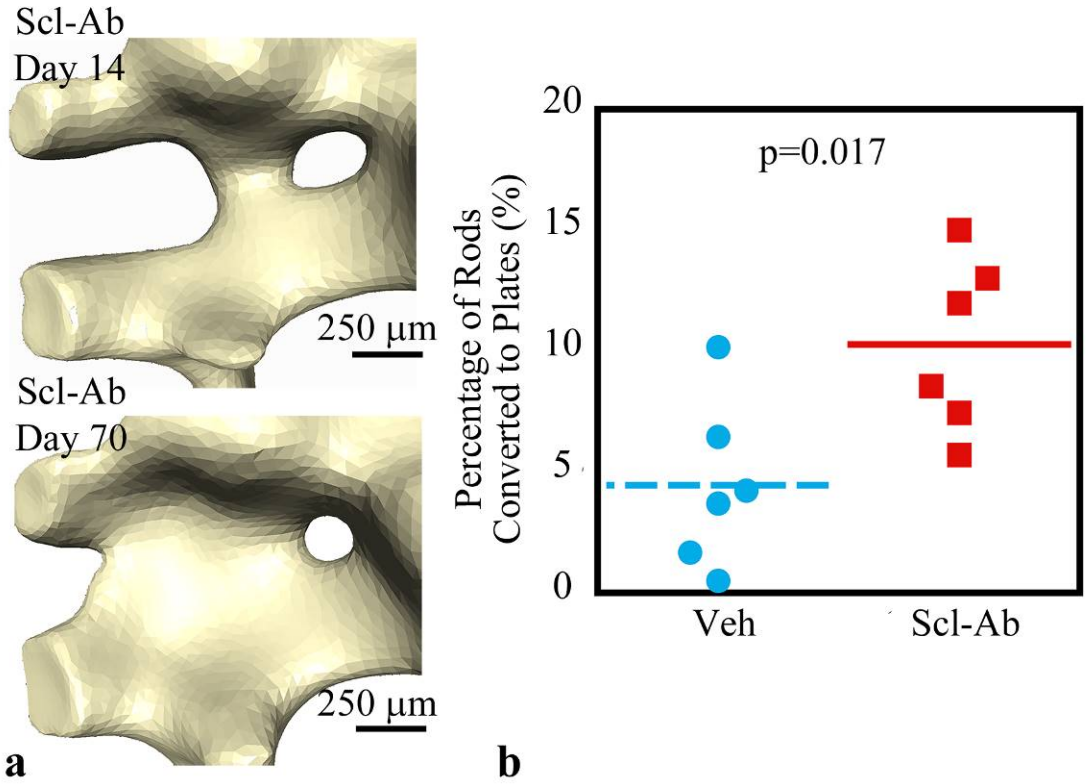

Figure 3.4. Sclerostin Antibody converts trabecular rods to trabecular plates. (A) An example of the conversion of rod-like trabeculae to a plate-like trabecula is shown (sclerostin antibody treated animal). (B) The percentage of rod-like trabeculae which were converted to plate-like trabeculae during the 8-week study period is shown.

Table 3.1. Traditional and ITS-based bone microstructural measurements are shown for each group, Mean ± SD, 95% CI (5th, 95th).

Measurement	Vehicle (n = 6)	Scl-Ab (n = 6)	p-value
Bone Volume Fraction (BV/TV, %)	42.10 ± 12.14 (29.37, 54.84)	53.87 ± 4.68 (48.96, 58.78)	0.051
Trabecular thickness (Tb.Th, µm)	219.18 ± 42.35 (174.74, 263.63)	272.39 ± 33.66 (237.06,	0.037

		307.71)	
Structural modeling Index (SMI)	0.99 ± 0.82 (0.13, 1.85)	0.13 ± 0.47 (-0.36, 0.62)	0.050
Trabecular Separation (Tb.Sp, μm)	679.97 ± 32.94 (645.40, 714.54)	687.12 ± 29.95 (655.69, 718.55)	0.702
Plate-Bone Volume Fraction (pBV/TV, %)	30.08 ± 12.90 (16.55, 43.61)	42.88 ± 4.67 (37.98, 47.78)	0.045
Rod-Bone Volume Fraction (rBV/TV, %)	12.31 ± 3.38 (8.76, 15.86)	11.41± 3.30 (7.94, 14.88)	0.650
Plate Volume/Bone Volume (pBV/BV, %)	69.00± 12.55 (56.45, 81.55)	79.63 ± 5.97 (73.65, 85.60)	0.091
Plate Bone Volume /Rod Bone Volume (pBV/rBV)	2.66 ± 1.53 (1.06, 4.27)	4.06 ± 1.33 (2.67, 5.46)	0.121
Plate-like Trabecular Thickness (pTb.Th, μm)	194.15 ± 36.90 (155.43, 232.87)	239.33 ± 27.29 (210.70, 267.96)	0.037
Rod-like Trabecular Thickness (rTb.Th, μm)	153.92 ± 7.74 (145.79, 162.05)	166.66 ± 8.99 (157.23, 176.09)	0.025

No. of rods converted to plates / No. rods (%)	4.45 ± 3.48 (0.80, 8.10)	10.27 ± 3.59 (6.50, 14.05)	0.017
Axial-Bone Volume Fraction (aBV/TV, %)	19.12 ± 6.24 (12.62, 25.72)	26.32 ± 2.66 (23.54, 29.12)	0.026
Oblique-Bone Volume Fraction (oBV/TV, %)	11.97 ± 3.46 (8.33, 15.60)	15.13 ± 2.20 (12.82, 17.45)	0.088
Transverse-Bone Volume Fraction (tBV/TV, %)	11.34 ± 3.23 (7.95, 14.73)	12.87 ± 2.75 (9.99, 15.76)	0.396
Axial-Trabecular Thickness (aTb.Th, μm)	225.02 ± 41.27 (181.71, 268.32)	273.62 ± 32.71 (239.30, 307.94)	0.047
Oblique-Trabecular Thickness (oTb.Th, μm)	229.04 ± 46.20 (180.55, 277.52)	285.26 ± 37.18 (246.23, 324.28)	0.043
Transverse-Trabecular Thickness (tTb.Th, μm)	224.70 ± 42.00 (180.62, 268.77)	283.83 ± 36.17 (245.87, 321.78)	0.026
Axial Apparent Stiffness (MPa)	2270 ± 1113 (1102, 3438)	3327 ± 416 (2891, 3764)	0.054

Transverse Apparent Stiffness (MPa)	1464 ± 852 (570, 2358)	2401 ± 439 (1940, 2862)	0.038

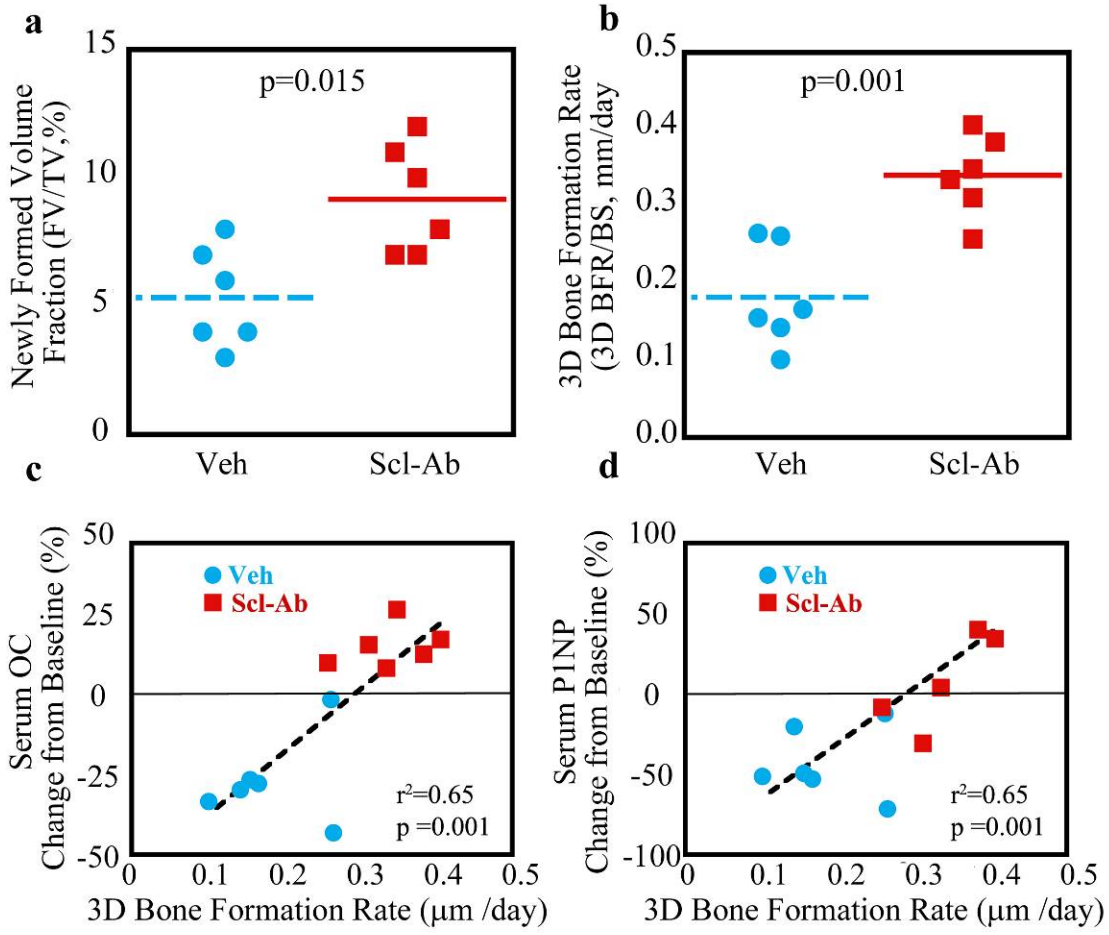

Figure 3.5. Sclerostin Antibody increases three-dimensional bone formation related to serum markers of bone formation. Three-dimensional measurements of bone formation are shown for each group (A) Newly formed bone volume, (B) Bone formation rate. Percentage change in (C) serum osteocalcin (OC) and (D) and serum intact N-terminal propeptide of type 1 procollagen (P1NP) as measured two weeks following treatment and compared to baseline levels (week 0) correspond to the three-dimensional bone formation rate.

Table 3.2 Three-dimensional dynamic bone histomorphometry measurements are shown for each group, Mean ± SD, 95% CI (5th, 95th).

Measurement	Vehicle (n = 6)	Scl-Ab (n = 6)	p-value
Newly formed volume fraction (FV/TV, %)	5.38 ± 2.04 (3.24, 7.53)	9.04 ± 2.28 (6.65, 11.44)	0.015
3D Mineralizing Surface (3D MS/BS, %)	26.30 ± 8.80 (17.07, 35.53)	40.35 ± 5.07 (35.03, 45.67)	0.007
3D Mineral Apposition Rate (3D MAR, µm/day)	0.69 ± 0.05 (0.63, 0.74)	0.84 ± 0.05 (0.79, 0.89)	0.0003
3D Bone Formation Rate (3D BFR/BS, µm/day)	0.18 ± 0.07 (0.11, 0.25)	0.34 ± 0.05 (0.29, 0.39)	0.001
3D Mineralizing Surface-Tetracycline Labels (3D MS/BS-Tet, %)	14.10 ± 10.82 (2.74, 25.46)	33.32 ± 9.77 (23.07, 43.58)	0.009
3D Mineral Apposition Rate-Tetracycline Labels (3D MAR-Tet, µm/day)	1.45± 0.19 (1.25, 1.65)	1.55 ± 0.07 (1.48, 1.63)	0.260
3D Bone Formation Rate-Tetracycline Labels (3D BFR/BS-Tet, µm/day)	0.22 ± 0.19 (0.02, 0.42)	0.52 ± 0.17 (0.34, 0.70)	0.016
3D Mineralizing Surface- Calcein	12.32 ± 7.49	34.40 ± 9.29	0.001

Labels (3D MS/BS-Cal, %)	(4.46, 20.19)	(24.65, 44.15)	
3D Mineral Apposition Rate-Calcein Labels (3D MAR-Cal, µm/day)	1.42 ± 0.18 (1.23, 1.60)	1.63 ± 0.12 (1.50, 1.75)	0.038
3D Bone Formation Rate-Calcein Labels (3D BFR/BS-Cal, µm/day)	0.17 ± 0.10 (0.07, 0.27)	0.56 ± 0.16 (0.39, 0.72)	0.0004

Sclerostin antibody treatment was associated with large changes in trabecular rod- and plate-like morphology, including increases in the plate-bone volume fraction ($p < 0.045$, See Figure 3.6A, Table 3.1). Additionally, sclerostin antibody treatment increased the thickness of both plate-like and rod-like trabeculae compared to controls ($p < 0.05$, Table 3.1). Increases in trabecular thickness associated with sclerostin treatment were distributed uniformly among trabeculae with different orientation (axial, oblique and transverse) ($p < 0.05$, See Figure 3.6D, Table 3.1). Additional ITS-based microstructural measurements can be found in Table 3.3 in ***Supplementary Materials***.

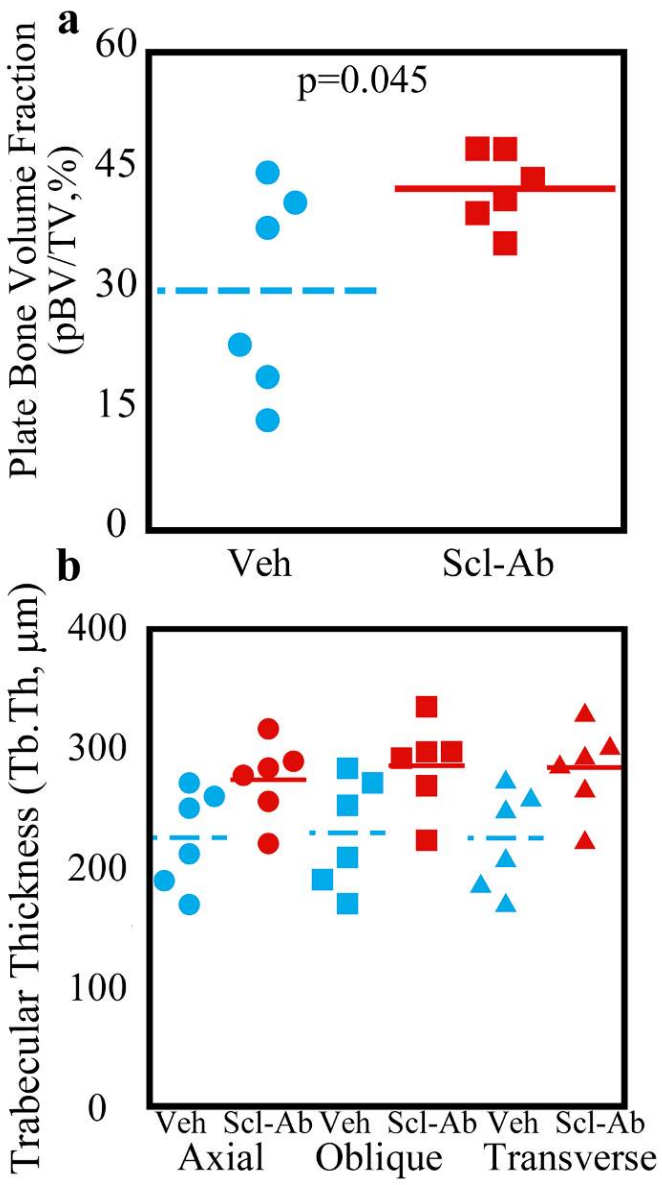

Figure 3.6. Sclerostin antibody treatment improves trabecular morphology and orientation. (A) Whole specimen measurements of Plate-bone volume fraction are shown for each group. (B) Trabecular thickness was increased in all trabecular orientations due to sclerostin antibody treatment ($p<0.05$ vs Veh for each orientation).

Sclerostin antibody treatment increased apparent stiffness in the axial and transverse directions compared to vehicle controls ($p = 0.038$-0.054, Table 3.1). Apparent stiffness in both directions was strongly correlated with measurements of cancellous bone microarchitecture such as bone volume fraction, plate-bone volume

fraction, and axial-bone volume fraction (See Figure 3.7 in ***Supplementary Materials***).

3.5. Discussion

Over an 8 week period, treatment with sclerostin antibody increased bone formation leading to a conversion of rod-like trabeculae to plate-like trabeculae and an increase in thickness of trabecular plates and rods in cancellous bone. Trabecular orientation did not influence where sclerostin antibody-induced bone formation occurred. Bone volume fraction correlated strongly with mechanical performance in our high resolution finite element models, regardless of treatment condition. No measurements of local trabecular morphology or orientation imparted any additional improvements to prediction of cancellous bone mechanical performance beyond what could be attributed to bone volume fraction.

We did not observe the formation of entirely newly trabeculae in any of the specimens. Banse and colleagues observed new trabecular connections, or "bridges" in two-dimensional, backscatter electron microscopy images. Banse surmised that these bridges were repairing struts perforated by osteoclastic resorption [22, 23]. In analyzing trabecular bone in three-dimensions, we observed multiple cross-sectional images of trabecular bridges that were not, in fact newly formed trabeculae. That no newly formed trabeculae were observed in cancellous bone with enhanced bone formation supports the idea that fenestration and loss of trabeculae during remodeling is irreversible [21].

The current study was able to analyze the rod-like and plate-like structure of individual trabeculae, providing the most detailed description of changes in trabecular morphology associated with treatment to date. The ITS analysis is more representative of trabecular microstructure than traditional measures such as structure model index (SMI), which measures rod and plate-like trabecular morphology based solely on strut curvature. Salmon and colleagues argue that the SMI measurement is confounded by a strong correlation with bone volume fraction and, consequently, does not in fact measure the rod-and plate-like structure of trabecular bone [40]. Our findings are consistent with a report by Maquer and colleagues in which bone volume fraction and fabric anisotropy explained mechanical stiffness of cancellous bone and that morphological measurements from either individual trabecula segmentation or trabecular bone score (TBS) provided no improvement in predicting cancellous bone stiffness [41].

The current study demonstrates a new method of analyzing longitudinal changes in trabecular microarchitecture associated with bone formation. Longitudinal evaluation of changes in trabecular microarchitecture has been performed with repeated, or "serial", microcomputed tomography applied to live animals [24-29]. Altman and colleagues showed that bone formation due to combined parathyroid hormone and alendronate treatment increased plate-like trabecular microarchitecture in rats over 12 days of treatment [24]. Lambers and colleagues used serial microcomputed tomography to observe changes in bone formation and resorption due to cyclic mechanical loading in a mouse-tail loading model [29]. Christen and

colleagues have correlated bone formation and resorption measured using HR-pQCT with locations of physiological tissue loading in the human distal tibia. While serial microcomputed tomography and HR-pQCT are non-invasive and non-destructive methods to access remodeling sites in cancellous bone, both approaches are subject to limitations. *In vivo,* serial microCT approaches are unable to accurately capture small bone formation events due to voxel size (10-11 μm) and are limited to the extremities of small animal species. HR-pQCT allows for the imaging of human bone tissue but is even more limited to in capturing bone formation due to a voxel size (often 82 μm or greater). In contrast, longitudinal imaging of bone formation using serial milling, while time intensive, can be performed on a specimen from any skeletal site and has a voxel size of 1-5 μm allowing for the detection of small or newly initiated locations of bone formation. Additionally, serial milling involves visualization of bone formation using fluorochrome labels (the gold standard for assessment of bone formation) making it more sensitive to bone formation in cancellous bone than *in vivo* microCT or HR-pQCT, which may present errors due to partial volume effects at bone surfaces [28]. We confirmed the validity of our three-dimensional measurements by comparing them to whole system markers for bone formation. Serum markers for bone formation (OC and P1NP) were strongly correlated with the three-dimensional dynamic bone histomorphometry ($r^2 = 0.65$ for both, Figure 3.5C-D). Correlations between three-dimensional measurements of bone formation and serum markers are similar, and in some cases stronger, to correlations between two-dimensional images of fluorochrome labels and serum markers of bone formation [8, 42].

An important limitation of the current study is that we do not account for resorption that occurred during the 8-week period, resulting in slight changes to the initial trabecular microstructure. We expect that not accounting for resorption volume may explain why the percentage of rods converted to plates in vehicle controls was greater than zero, which would be expected following balanced bone remodeling. Sclerostin antibody treatment increases modeling-based formation (bone formation not preceded by bone resorption) and reduces bone resorption [7] so any effects of resorption would be minimal. A previous study using these animals has shown that alterations in bone formation and resorption due to sclerostin antibody treatment did not change bone matrix quality in comparison to vehicle controls [43]. An additional limitation of the current study is that our analysis was limited to the 5th lumbar vertebra. Although we did not examine other regions of the skeleton, a previous study found that treatment with sclerostin antibody increased bone formation (bone formation rate) as well as trabecular microstructure (trabecular thickness) in both the proximal tibia and 2nd lumbar vertebra in adolescent female cynomolgus monkeys [8], suggesting that our findings may be indicative of changes elsewhere in the skeleton.

In conclusion, sclerostin antibody improved the trabecular morphology of cancellous bone by a prolonged increase in bone formation over 8 weeks. Improvements in local trabecular morphology due to sclerostin antibody may counteract the reduction in plate-like bone volume associated with osteoporosis.

3.6. Acknowledgements

Funding and specimens were provided by Amgen Inc. and UCB Pharma. Cornell's National Science Foundation (NSF) Grant DGE-1,144,153, NSF Graduate Research Fellowship Program (to JBM), NSF Graduate Research Fellowship Program (to AMT), and a Cornell Colman fellowship (to AMT).

Conflict of interest statement: Michael Ominsky reports personal fees from Amgen Inc during the conduct of the study; personal fees from Amgen Inc outside the submitted work. Jonathan Matheny and Ashley Torres report non-financial support from Amgen Inc and UCB Pharma (supplied specimens) during the conduct of the study. Christopher Hernandez reports grants and non-financial support from Amgen Inc and UCB Pharma (supplied specimens) during the conduct of the study. The authors have full control of primary data and agree to journal review of the data if requested.

3.7. Supplemental Materials

Table 3.3. Additional ITS-based bone microstructural measurements are shown for each group, Mean ± SD, 95% CI (5th, 95th).

Measurement	Vehicle (n = 6)	Scl-Ab (n = 6)	p-value
Volume of rods converted to plates / Volume of rods (%)	2.37± 1.84 (0.43, 4.30)	6.20 ± 2.45 (3.63, 8.77)	0.012
No. of plate-like trabeculae (pTb.N)	809.00± 190.78 (608.79, 1009.20)	933.83± 178.44 (746.57,	0.269

		1121.10)	
No. of rod-like trabeculae (rTb.N)	499.00± 150.26 (341.32, 656.68)	404.67± 143.53 (254.04, 555.29)	0.292
No. of plate-like trabeculae/ No. of rod-like trabeculae	1.75 ± 0.69 (1.03, 2.48)	2.41 ± 0.42 (1.98, 2.85)	0.072
Plate-Plate Junction Density (P-P Junc.D, 1/mm^3)	24.71 ± 5.36 (19.08, 30.24)	26.83 ± 7.23 (19.25, 34.41)	0.577
Plate-Rod Junction Density (P-R Junc.D, 1/mm3)	28.65 ± 6.04 (22.31, 34.99)	27.41 ± 8.40 (18.60, 36.23)	0.776
Rod-Rod Junction Density (R-R Junc.D, 1/mm3)	5.53± 2.78 (2.61, 8.45)	3.56 ± 1.63 (1.84, 5.27)	0.165
Axial Volume/Bone Volume (aBV/BV, %)	44.82 ± 3.86 (40.96, 48.67)	48.66 ± 5.67 (42.99, 54.34)	0.200
Oblique Volume/Bone Volume (oBV/BV, %)	28.23 ± 2.38	27.77 ± 1.97	0.722

	(25.85, 30.60)	(25.80, 29.74)	
Transverse Volume/Bone Volume (tBV/BV, %)	26.97 ± 3.00 (23.97, 29.97)	23.58 ± 4.09 (19.49, 27.67)	0.133

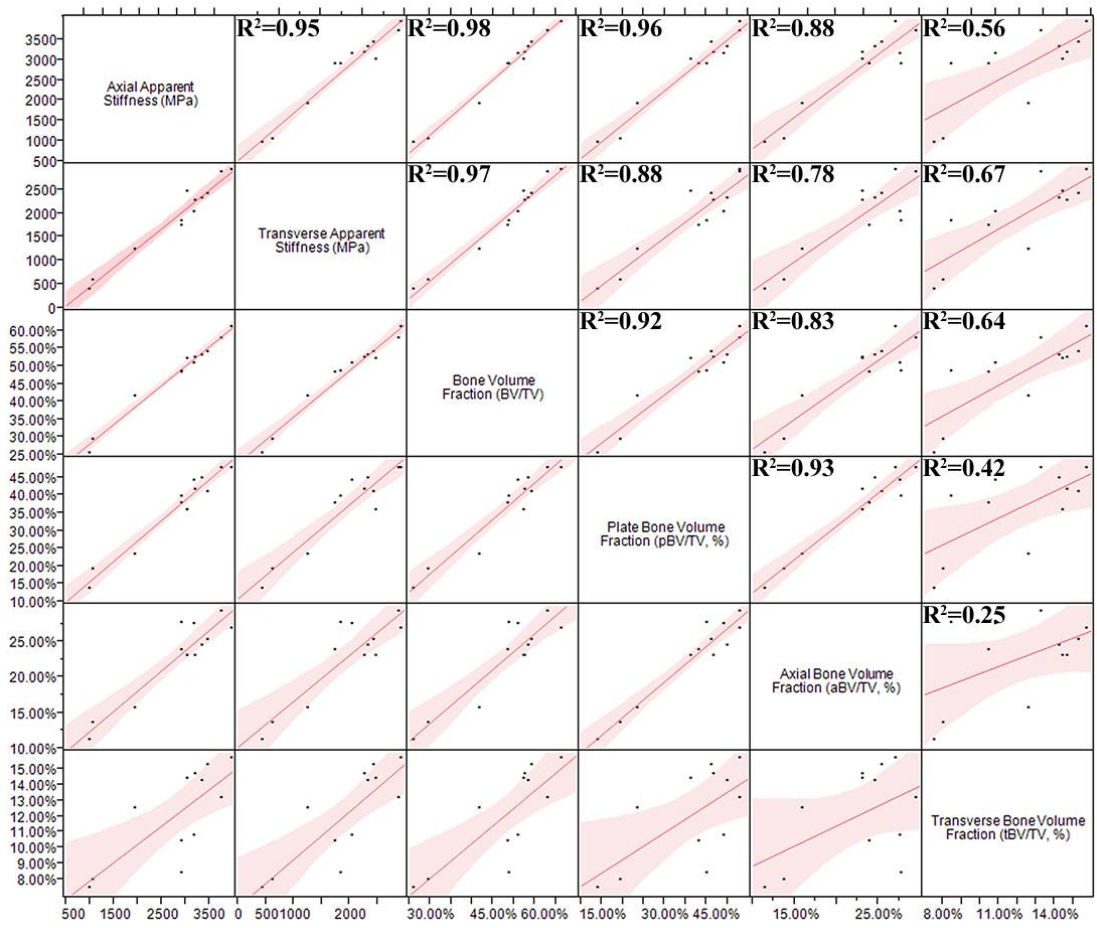

Figure 3.7. Correlation Scatterplots for measurements of stiffness derived from high resolution finite element models and traditional and ITS-based measurements of bone microstructure are shown.

REFERENCES

[1] H.K. Genant, P.D. Delmas, P. Chen, Y. Jiang, E.F. Eriksen, G.P. Dalsky, R. Marcus, J. San Martin, Severity of vertebral fracture reflects deterioration of bone microarchitecture, Osteoporos Int 18(1) (2007) 69-76.

[2] X. Li, M.S. Ominsky, K.S. Warmington, S. Morony, J. Gong, J. Cao, Y. Gao, V. Shalhoub, B. Tipton, R. Haldankar, Q. Chen, A. Winters, T. Boone, Z. Geng, Q.T. Niu, H.Z. Ke, P.J. Kostenuik, W.S. Simonet, D.L. Lacey, C. Paszty, Sclerostin antibody treatment increases bone formation, bone mass, and bone strength in a rat model of postmenopausal osteoporosis, J Bone Miner Res 24(4) (2009) 578-88.

[3] K.E. Poole, R.L. van Bezooijen, N. Loveridge, H. Hamersma, S.E. Papapoulos, C.W. Lowik, J. Reeve, Sclerostin is a delayed secreted product of osteocytes that inhibits bone formation, Faseb J 19(13) (2005) 1842-4.

[4] H. Hamersma, J. Gardner, P. Beighton, The natural history of sclerosteosis, Clin Genet 63(3) (2003) 192-7.

[5] M.E. Brunkow, J.C. Gardner, J. Van Ness, B.W. Paeper, B.R. Kovacevich, S. Proll, J.E. Skonier, L. Zhao, P.J. Sabo, Y. Fu, R.S. Alisch, L. Gillett, T. Colbert, P. Tacconi, D. Galas, H. Hamersma, P. Beighton, J. Mulligan, Bone dysplasia sclerosteosis results from loss of the SOST gene product, a novel cystine knot-containing protein, Am J Hum Genet 68(3) (2001) 577-89.

[6] W. Balemans, M. Ebeling, N. Patel, E. Van Hul, P. Olson, M. Dioszegi, C. Lacza, W. Wuyts, J. Van Den Ende, P. Willems, A.F. Paes-Alves, S. Hill, M. Bueno, F.J. Ramos, P. Tacconi, F.G. Dikkers, C. Stratakis, K. Lindpaintner, B. Vickery, D.

Foernzler, W. Van Hul, Increased bone density in sclerosteosis is due to the deficiency of a novel secreted protein (SOST), Hum Mol Genet 10(5) (2001) 537-43.

[7] M.S. Ominsky, Q.T. Niu, C. Li, X. Li, H.Z. Ke, Tissue-level mechanisms responsible for the increase in bone formation and bone volume by sclerostin antibody, J Bone Miner Res 29(6) (2014) 1424-30.

[8] M.S. Ominsky, F. Vlasseros, J. Jolette, S.Y. Smith, B. Stouch, G. Doellgast, J. Gong, Y. Gao, J. Cao, K. Graham, B. Tipton, J. Cai, R. Deshpande, L. Zhou, M.D. Hale, D.J. Lightwood, A.J. Henry, A.G. Popplewell, A.R. Moore, M.K. Robinson, D.L. Lacey, W.S. Simonet, C. Paszty, Two doses of sclerostin antibody in cynomolgus monkeys increases bone formation, bone mineral density, and bone strength, J Bone Miner Res 25(5) (2010) 948-59.

[9] D. Padhi, M. Allison, A.J. Kivitz, M.J. Gutierrez, B. Stouch, C. Wang, G. Jang, Multiple doses of sclerostin antibody romosozumab in healthy men and postmenopausal women with low bone mass: a randomized, double-blind, placebo-controlled study, J Clin Pharmacol 54(2) (2014) 168-78.

[10] D. Padhi, G. Jang, B. Stouch, L. Fang, E. Posvar, Single-dose, placebo-controlled, randomized study of AMG 785, a sclerostin monoclonal antibody, J Bone Miner Res 26(1) (2011) 19-26.

[11] M.R. McClung, A. Grauer, S. Boonen, M.A. Bolognese, J.P. Brown, A. Diez-Perez, B.L. Langdahl, J.Y. Reginster, J.R. Zanchetta, S.M. Wasserman, L. Katz, J. Maddox, Y.C. Yang, C. Libanati, H.G. Bone, Romosozumab in postmenopausal women with low bone mineral density, N Engl J Med 370(5) (2014) 412-20.

[12] F. Cosman, D.B. Crittenden, J.D. Adachi, N. Binkley, E. Czerwinski, S. Ferrari, L.C. Hofbauer, E. Lau, E.M. Lewiecki, A. Miyauchi, C.A. Zerbini, C.E. Milmont, L. Chen, J. Maddox, P.D. Meisner, C. Libanati, A. Grauer, Romosozumab Treatment in Postmenopausal Women with Osteoporosis, N Engl J Med 375(16) (2016) 1532-1543.

[13] S.R. Cummings, D.B. Karpf, F. Harris, H.K. Genant, K. Ensrud, A.Z. LaCroix, D.M. Black, Improvement in spine bone density and reduction in risk of vertebral fractures during treatment with antiresorptive drugs, Am J Med 112(4) (2002) 281-9.

[14] P.D. Delmas, Z. Li, C. Cooper, Relationship between changes in bone mineral density and fracture risk reduction with antiresorptive drugs: some issues with meta-analyses, J Bone Miner Res 19(2) (2004) 330-7.

[15] C.J. Hernandez, T.M. Keaveny, A biomechanical perspective on bone quality, Bone 39(6) (2006) 1173-81.

[16] M.L. Bouxsein, S.K. Boyd, B.A. Christiansen, R.E. Guldberg, K.J. Jepsen, R. Muller, Guidelines for assessment of bone microstructure in rodents using micro-computed tomography, J Bone Miner Res 25(7) (2010) 1468-86.

[17] X.S. Liu, P. Sajda, P.K. Saha, F.W. Wehrli, G. Bevill, T.M. Keaveny, X.E. Guo, Complete volumetric decomposition of individual trabecular plates and rods and its morphological correlations with anisotropic elastic moduli in human trabecular bone, J Bone Miner Res 23(2) (2008) 223-35.

[18] B. Zhou, X.S. Liu, J. Wang, X.L. Lu, A.J. Fields, X.E. Guo, Dependence of mechanical properties of trabecular bone on plate-rod microstructure determined by individual trabecula segmentation (ITS), J Biomech 47(3) (2014) 702-8.

[19] C. Sanchez, M.A. Deberg, N. Piccardi, P. Msika, J.Y. Reginster, Y.E. Henrotin, Osteoblasts from the sclerotic subchondral bone downregulate aggrecan but upregulate metalloproteinases expression by chondrocytes. This effect is mimicked by interleukin-6, -1beta and oncostatin M pre-treated non-sclerotic osteoblasts, Osteoarthritis Cartilage 13(11) (2005) 979-87.

[20] X.S. Liu, E.M. Stein, B. Zhou, C.A. Zhang, T.L. Nickolas, A. Cohen, V. Thomas, D.J. McMahon, F. Cosman, J. Nieves, E. Shane, X.E. Guo, Individual trabecula segmentation (ITS)-based morphological analyses and microfinite element analysis of HR-pQCT images discriminate postmenopausal fragility fractures independent of DXA measurements, J Bone Miner Res 27(2) (2012) 263-72.

[21] X.E. Guo, C.H. Kim, Mechanical consequence of trabecular bone loss and its treatment: a three-dimensional model simulation, Bone 30(2) (2002) 404-11.

[22] X. Banse, J.P. Devogelaer, C. Delloye, A. Lafosse, D. Holmyard, M. Grynpas, Irreversible perforations in vertebral trabeculae?, J Bone Miner Res 18(7) (2003) 1247-53.

[23] X. Banse, J.P. Devogelaer, D. Holmyard, M. Grynpas, Vertebral cancellous bone turn-over: microcallus and bridges in backscatter electron microscopy, Micron 36(7-8) (2005) 710-4.

[24] A.R. Altman, W.J. Tseng, C.M. de Bakker, B.K. Huh, A. Chandra, L. Qin, X.S. Liu, A closer look at the immediate trabecula response to combined parathyroid hormone and alendronate treatment, Bone 61 (2014) 149-57.

[25] A.R. Altman, C.M. de Bakker, W.J. Tseng, A. Chandra, L. Qin, X.S. Liu, Enhanced individual trabecular repair and its mechanical implications in parathyroid hormone and alendronate treated rat tibial bone, J Biomech Eng 137(1) (2015) 10.
[26] F.A. Schulte, F.M. Lambers, G. Kuhn, R. Muller, In vivo micro-computed tomography allows direct three-dimensional quantification of both bone formation and bone resorption parameters using time-lapsed imaging, Bone 48(3) (2011) 433-42.
[27] A.I. Birkhold, H. Razi, G.N. Duda, R. Weinkamer, S. Checa, B.M. Willie, Mineralizing surface is the main target of mechanical stimulation independent of age: 3D dynamic in vivo morphometry, Bone 66 (2014) 15-25.
[28] C.M. de Bakker, A.R. Altman, W.J. Tseng, M.B. Tribble, C. Li, A. Chandra, L. Qin, X.S. Liu, muCT-based, in vivo dynamic bone histomorphometry allows 3D evaluation of the early responses of bone resorption and formation to PTH and alendronate combination therapy, Bone 73 (2015) 198-207.
[29] F.M. Lambers, F.A. Schulte, G. Kuhn, D.J. Webster, R. Muller, Mouse tail vertebrae adapt to cyclic mechanical loading by increasing bone formation rate and decreasing bone resorption rate as shown by time-lapsed in vivo imaging of dynamic bone morphometry, Bone 49(6) (2011) 1340-50.
[30] J.J. de Jong, P.C. Willems, J.J. Arts, S.G. Bours, P.R. Brink, T.A. van Geel, M. Poeze, P.P. Geusens, B. van Rietbergen, J.P. van den Bergh, Assessment of the healing process in distal radius fractures by high resolution peripheral quantitative computed tomography, Bone 64 (2014) 65-74.

[31] P. Christen, K. Ito, R. Ellouz, S. Boutroy, E. Sornay-Rendu, R.D. Chapurlat, B. van Rietbergen, Bone remodelling in humans is load-driven but not lazy, Nat Commun 5 (2014) 4855.

[32] R. Ellouz, R. Chapurlat, B. van Rietbergen, P. Christen, J.B. Pialat, S. Boutroy, Challenges in longitudinal measurements with HR-pQCT: evaluation of a 3D registration method to improve bone microarchitecture and strength measurement reproducibility, Bone 63 (2014) 147-57.

[33] M.K. Manhard, J.S. Nyman, M.D. Does, Advances in imaging approaches to fracture risk evaluation, Transl Res (2016).

[34] C.R. Slyfield, E.V. Tkachenko, D.L. Wilson, C.J. Hernandez, Three-dimensional dynamic bone histomorphometry, J Bone Miner Res 27(2) (2012) 486-95.

[35] J.B. Matheny, C.R. Slyfield, E.V. Tkachenko, I. Lin, K.M. Ehlert, R.E. Tomlinson, D.L. Wilson, C.J. Hernandez, Anti-resorptive agents reduce the size of resorption cavities: A three-dimensional dynamic bone histomorphometry study, Bone 57(1) (2013) 277-83.

[36] C.R. Slyfield, Jr., K.E. Niemeyer, E.V. Tkachenko, R.E. Tomlinson, G.G. Steyer, C.G. Patthanacharoenphon, G.J. Kazakia, D.L. Wilson, C.J. Hernandez, Three-dimensional surface texture visualization of bone tissue through epifluorescence-based serial block face imaging, J Microsc 236(1) (2009) 52-9.

[37] E.N. Cresswell, M.G. Goff, T.M. Nguyen, W.X. Lee, C.J. Hernandez, Spatial relationships between bone formation and mechanical stress within cancellous bone, J Biomech 49(2) (2016) 222-8.

[38] M.S. Ominsky, C. Li, X. Li, H.L. Tan, E. Lee, M. Barrero, F.J. Asuncion, D. Dwyer, C.Y. Han, F. Vlasseros, R. Samadfam, J. Jolette, S.Y. Smith, M. Stolina, D.L. Lacey, W.S. Simonet, C. Paszty, G. Li, H.Z. Ke, Inhibition of sclerostin by monoclonal antibody enhances bone healing and improves bone density and strength of nonfractured bones, J Bone Miner Res 26(5) (2011) 1012-21.

[39] M. Doube, M.M. Klosowski, I. Arganda-Carreras, F.P. Cordelieres, R.P. Dougherty, J.S. Jackson, B. Schmid, J.R. Hutchinson, S.J. Shefelbine, BoneJ: Free and extensible bone image analysis in ImageJ, Bone 47(6) (2010) 1076-9.

[40] P.L. Salmon, C. Ohlsson, S.J. Shefelbine, M. Doube, Structure model index does not measure rods and plates in trabecular bone, Front. Endocrinol. (Lausanne) 6 (2015) 1-10.

[41] G. Maquer, S.N. Musy, J. Wandel, T. Gross, P.K. Zysset, Bone Volume Fraction and Fabric Anisotropy Are Better Determinants of Trabecular Bone Stiffness Than Other Morphological Variables, J. Bone Miner. Res. 30(6) (2015) 1000-1008.

[42] P. Chavassieux, N. Portero-Muzy, J.P. Roux, P. Garnero, R. Chapurlat, Are Biochemical Markers of Bone Turnover Representative of Bone Histomorphometry in 370 Postmenopausal Women?, J. Clin. Endocrinol. Metab. 100(12) (2015) 4662-4668.

[43] R.D. Ross, L.H. Edwards, A.S. Acerbo, M.S. Ominsky, A.S. Virdi, K. Sena, L.M. Miller, D.R. Sumner, Bone matrix quality after sclerostin antibody treatment, J Bone Miner Res 29(7) (2014) 1597-607.

CHAPTER 4
MATERIAL HETEROGENEITY IN CANCELLOUS BONE PROMOTES DEFORMATION RECOVERY AFTER MECHANICAL FAILURE

The following chapter was published in the Proceedings of the National Academy of Sciences (PNAS) in 2016 in Volume 113(11), pgs. 2892-2897. The article is titled "Material heterogeneity in cancellous bone promotes deformation recovery after mechanical failure" by Torres AM, Matheny JB, Keaveny TM, Taylor D, Rimnac CM, and Hernandez CJ and is reprinted here with permission of PNAS. One paragraph discussing resorption cavities, which was not included in the PNAS article has been added to the introduction. Authors Torres AM, and Matheny JB contributed equally to the published work. Torres contributed primarily to the mechanical testing and serial milling imaging of cancellous bone specimens and analysis of advanced glycation end products. Matheny contributed primary to the analyses involving microscopic tissue damage, resorption cavities and mechanical stresses from finite element analysis.

4.1. Abstract

Many natural structures use a foam core and solid outer shell to achieve high strength and stiffness with relatively small amounts of mass. Biological foams, however, must also resist crack growth. The process of crack propagation within the struts of a foam is not well understood and is complicated by the foam microstructure. We demonstrate that in cancellous bone, the foam-like component of whole bones, damage propagation during cyclic loading is dictated not by local tissue stresses but by heterogeneity of material properties associated with increased ductility of strut surfaces. The increase in surface ductility is unexpected because it is the opposite pattern generated by surface treatments to increase fatigue life in man-made materials, which often result in reduced surface ductility. We show that the more ductile surfaces of cancellous bone are a result of reduced accumulation of advanced glycation end products as compared to the strut interior. Damage is therefore likely to accumulate in strut centers making cancellous bone more tolerant of stress concentrations at strut surfaces. Hence the structure is able to recover more deformation after failure, and return to a closer approximation of its original shape. Increased recovery of deformation is a passive mechanism seen in biology for “setting” a broken bone that allows for a better approximation of initial shape during healing processes, and is likely the most important mechanical function. Our findings suggest a novel biomimetic design strategy in which tissue level material heterogeneity in foams can be used to improve deformation recovery after failure.

4.2. Significance Statement

Lightweight structures often employ foam cores to achieve high strength and stiffness. Structures that are submitted to cyclic loading with long service lives must also resist crack propagation. We show that the foam-like regions of cancellous bone resist damage propagation by varying material heterogeneity within struts, a strategy that makes the material less susceptible to stress concentrations at the surface and enhances the ability of the structure to recover its initial shape after mechanical failure. The ability to recover deformation after failure improves long-term function of bones after a fracture. Our findings suggest a novel design strategy of man-made foams in which material heterogeneity can be used to mitigate the effect of local failure to better maintain mechanical function.

4.3. Introduction

Many natural structures achieve a combination of low weight and mechanical properties that surpass what is currently possible with man-made materials [1]. A common structural motif in biological materials is a foam-like structure encased within a thin shell, a structure that uses less mass to achieve the same resistance to bending and torsional loads of solid structures [2, 3]. Foam core structures are seen in many biological systems including plants, feather stems and bones [2, 4]. In addition to increasing resistance to bending and torsional loads, the foam cores in biological materials must also resist failure from cracks and other damage generated by cyclic loading. However, little is known about the contribution of material toughness to failure in foams and other cellular solids.

Whole bones consist of a dense shell of cortical bone surrounding a foam-like tissue called cancellous bone. Bone tissue itself is a hierarchical composite consisting of a mineral component (primarily impure hydroxyapatite) and an organic polymer component (primarily

type I collagen). In bone, tissue level material toughness has been identified as a key mechanism in resisting osteoporosis- and age-related fractures [5]. The ability of bone tissue to resist crack growth has been studied predominately in cortical bone and is a result of a combination of intrinsic (ahead of crack tip) and extrinsic (behind crack tip) toughening mechanisms [6-9] resulting in a fracture toughness, K_{IC}, ranging from 2-8 MPa $m^{1/2}$ [6, 10, 11]. Advanced glycation end products accumulate in bone tissue over time and have been shown to have a detrimental effect on resistance to crack growth and fracture [12-14]. The most influential extrinsic toughening features in cortical bone are associated with a self-healing process called bone remodeling. During bone remodeling, discrete locations of old or damaged tissue are removed and replaced with newly synthesized material [15]. Completed remodeling sites have highly mineralized boundaries known as cement lines that contribute to crack deflection, thereby increasing tissue toughness [9, 16].

In engineering structures, stress risers are a common location for the initiation and propagation of microscopic tissue damage [17-19]. In bone there are many naturally occurring stress risers including resorption cavities formed during bone remodeling. Resorption cavities increase local stresses and strains [19, 20] and theoretical models predict that resorption cavities have a disproportionate effect on bone stiffness and strength of cancellous bone [21-23]. The mechanical effect of a stress riser is related to its size and local geometry [24]. Resorption cavities with a larger depth relative to local trabecular thickness can result in larger gross stress concentration and therefore more likely to promote microdamage [18, 25, 26].

The great majority of osteoporosis-related fractures occur in regions of the skeleton dominated by cancellous bone, yet little is known about resistance to crack growth in cancellous

bone tissue. Cancellous bone has a complex anisotropic microstructure made up of a network of struts called trabeculae (typically 400 μm long and 120 μm thick). Fracture toughness associated with flaws much larger than individual trabeculae (crack length 1 mm or larger) has been shown to be related to overall porosity in cancellous bone [4, 27, 28]. Tissue level toughness also influences failure of cancellous bone, but resistance to crack growth within individual trabeculae has not been reported previously and it is therefore unclear if alterations in tissue level material toughness contribute to osteoporosis- and age-related fractures in regions of cancellous bone.

Here we examine the propagation of tissue damage in cancellous bone during fatigue loading using a novel three-dimensional imaging approach known as serial milling. We report the propagation of 1,676 locations of tissue damage and the effects of local tissue stresses and stress concentrations on the surface of trabeculae. We find the propagation of tissue damage to be insensitive to local stresses and instead appear to be dominated by heterogeneities in tissue material properties related to accumulation of advanced glycation end products. We conclude that tissue level material heterogeneity in cancellous bone enhances deformation recovery of the structure, which promotes recovery of function after injury.

4.4. Materials and Methods

4.4.1 Specimen Collection

The fourth lumbar vertebral bodies of 11 human donors (4 male, 7 female, aged 62-88 years, tissue source NDRI) were examined in this study. Cylindrical cores of cancellous bone aligned in the superior-inferior direction (nominally 8 mm in diameter and 27 mm in length) were dissected from each vertebral body. Specimens were wrapped in saline soaked gauze and stored in airtight tubes at -20 °C prior to mechanical testing. Bone marrow was removed with a

low-pressure water jet. Each specimen was press fit into cylindrical brass end-caps and secured with cyanoacrylate glue (Loctite 401, Newington, CT, USA). Specimens were stored overnight at 4 °C while hydrated with saline soaked gauze to allow the glue to cure.

4.4.2. Mechanical Testing

Specimens were submitted to cyclic compressive loading in two separate cyclic bouts. Mechanical testing was performed at room temperature (23 °C). To maintain hydration during fatigue testing, specimens were kept hydrated with physiologically buffered saline (pH of 7.4). Strain was measured with a 25 mm gage length extensometer (MTS, Eden Prairie, MN, USA) attached to the specimen's end-caps. Applied load was measured with a load cell (100lb capacity, SSM-100, Transducer Techniques, CA, USA). Prior to each bout of loading, ten preconditioning cycles between 0 and 0.1% strain at a rate of 0.5 % per second were applied. Fatigue loading was applied cyclically between 0 N and a compressive load corresponding to $\sigma = E_0 * 0.0035$ mm/mm at a 4 Hz haversine waveform, where σ is stress and E_0 is the initial Young's modulus of the specimen (determined during preconditioning cycles, Figure 4.12A in ***Supplementary Materials***. The first bout of fatigue loading was stopped prior to overt failure by detecting rapid changes in the creep-fatigue curve (Figure 4.1B). Following the first bout of cyclic loading, specimens with end-caps were carefully removed and bulk stained in xylenol orange solution (0.5 mM, Sigma Chemical Co., St. Louis, MO). Specimens remained fully immersed in xylenol orange for 2 hours to label damage zones generated from the first bout of loading [29]. The specimens were then rinsed in three 20-minute washes of deionized water. The specimens were returned to the testing device, and a second bout of fatigue loading was applied until 5% apparent strain (Figure 4.1B). A negligible reduction in Young's modulus was caused by interruption of loading (Figure

4.12B in ***Supplementary Materials***). Following the second bout of loading, specimens were carefully removed from the testing device and bulk stained in calcein solution (0.5 mM, Sigma Chemical Co., St. Louis, MO) to label damage zones generated during the second bout of loading using the same 2 hour incubation period and rinses as the first damage stain [29]. Specimens were then removed from the end-caps using a low-speed diamond saw (Isomet, Buehler Ltd., Lake Bluff, IL) and embedded in methyl-methacrylate made opaque with sudan black dye in preparation for image acquisition using serial milling [30].

4.4.3. Microscopic Tissue Damage

Three-dimensional images of bone and fluorescent markers of damage zones were collected using serial milling to achieve a voxel size of 0.7 x 0.7 x 5.0 μm (690 GB per specimen, Figure 4.5 in ***Supplementary Materials***) [31]. Three images of each specimen were collected using different fluorescent filter sets: one channel to visualize bone tissue (350/420 nm, Ex/Em), and one for each of the two fluorescent markers of damage zones (xylenol orange - 545/620 nm, calcein - 470/525 nm). Images collected were segmented by a trained observer and underwent three-dimensional binary morphological operations. Propagating damage zones were identified as regions where the second damage stain was in direct contact with the first damage stain. Remodeling cavities on the bone surfaces were detected by irregular surface texture and traced manually in three dimensions [32]. Spatial correlations between damage zones and remodeling cavities were determined as the ratio of damage volume near remodeling cavities (within 8 μm) to that of bone volume selected at random that was found to be near remodeling cavities [33]. The characteristic size of each damage zone (c = cubed root of damage zone volume) was determined at the end of the first bout of loading ($c_{initial}$) and at the end of the second bout of

loading (c_{final}) and the growth rate was determined as follows:

$$\frac{dc}{dN} = \frac{c_{final} - c_{initial}}{N_{secondbout}},$$

where $N_{secondbout}$ is the number of cycles applied between the first and second bouts of loading.

4.4.4. Finite Element Modeling and Damage Propagation

Three-dimensional images of each specimen, collected prior to loading using microcomputed tomography (10 μm voxels), were used to generate linear elastic finite element models. Each finite element model consisted of 31-98 million elements and was implemented on the Stampede Supercomputer Cluster (Texas Advanced Computing Center) [34]. The tissue Young's modulus for each model was selected so that the stiffness of the finite element model matched that of the apparent Young's modulus determined experimentally (tissue Young's modulus 13.74 ± 3.25 GPa, mean ± SD). Compression applied at the apparent scale (millimeters) resulted in local regions of compression and tension (Figure 4.13 in ***Supplementary Materials***). The average von Mises stress within each damage zone, along with damage zone length, c, was used to calculate ΔK. Similar results were achieved with other scalar assays of tissue stress/strain.

4.4.5. Advanced Glycation End Products (AGEs)

Five cylindrical cores of cancellous bone from the same donor pool (2 male, 3 female, aged 67-88 years) were analyzed for fluorescent AGEs. Specimens were decalcified in a sodium citrate-formic acid solution and then dehydrated. Following dehydration, samples were embedded in paraffin, and 6 μm thick transverse sections were mounted onto slides. AGEs were observed by auto fluorescence in 5 sections per sample using a confocal microscope (Zeiss 710, 405/488 nm, Ex/Em) with uniform exposure time (150 ms). Bright field images were used to

normalize brightness among fields of view. Images were analyzed using Image J (developed at the U.S. National Institutes of Health).

4.5. Results

4.5.1. Fatigue Crack Growth within Trabeculae is Primarily Driven by Damage Size and Not Local Tissue Stress

We examined the propagation of tissue damage within cancellous bone (Figure 4.1A) from the fourth lumbar vertebral bodies of 11 human donors (4 male, 7 female, aged 62-88 years). Cylindrical specimens of cancellous bone were submitted to cyclic compression in two bouts of loading. After each bout of loading specimens were stained for tissue damage (first with xylenol orange then with calcein, Figure 4.1B). The applied loading brings the cancellous bone specimen into the tertiary phase of the creep-fatigue curve but does not cause overt failure (specimens remain intact). Three-dimensional fluorescent images of the entire cancellous bone microstructure (8 mm diameter, 4 mm in height) were collected using epifluorescence-based serial milling at a voxel size sufficient to observe tissue damage (0.7 × 0.7 × 5.0 μm voxels, see ***Materials and Methods*** and Figure 4.5 in ***Supplementary Materials***). The tissue damage examined consisted of microscopic cracks as well as regions of submicroscopic cracking, which together we refer to as "damage zones." The use of sequential staining made it possible to observe the propagation of damage zones in cancellous bone *in situ*. We found that 87% of the tissue damage generated during the second bout of loading was due to expansion of an already existing damage zone (i.e. propagation, Figure 4.1C, Table 4.1 in ***Supplementary Materials***) rather than the initiation of a new damage zone.

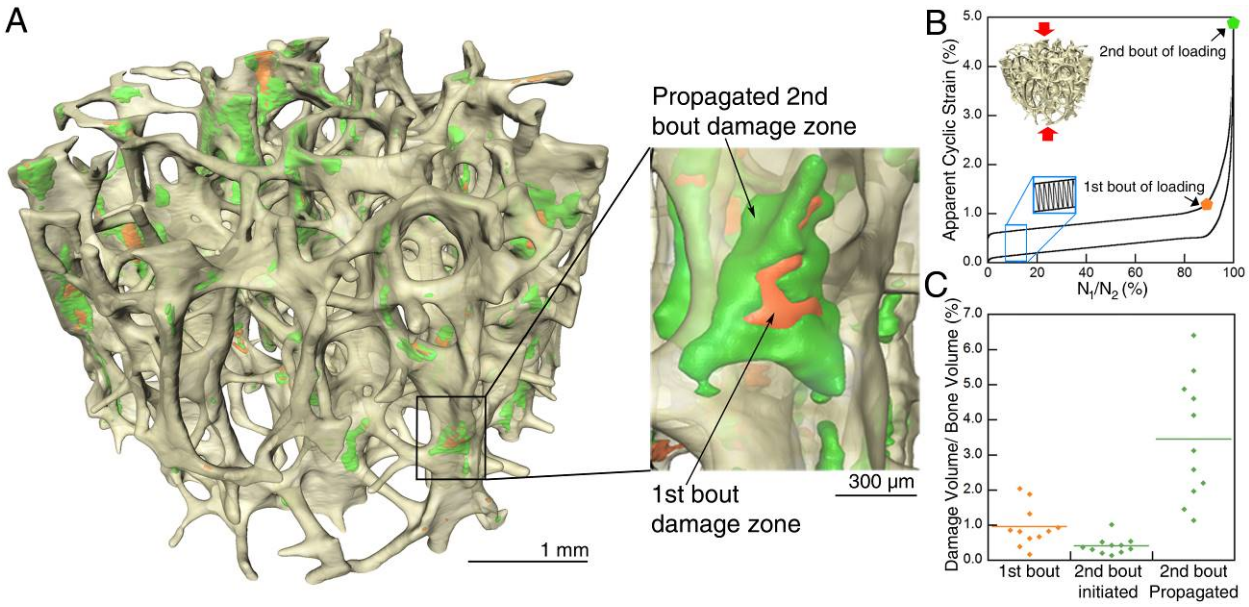

Figure 4.1. (A) A three-dimensional image of cancellous bone with tissue damage stained is shown. Propagating damage zones display green stain extending from orange stain. (B) The minimum and maximum strain per cycle is shown. Cyclic compressive loading was applied to cancellous bone specimens until the start of the tertiary phase of fatigue and a fluorescent stain (orange) was applied to mark damage zones. Cyclic loading was reinstated until 5% applied strain and a second fluorescent stain (green) was applied. (C) 87% percent of the damage volume in the second bout of loading had propagated from pre-existing damage.

Damage growth rates (dc/dN, m/cycle) and local stress intensity factor range (ΔK, MPa√m) were determined using the characteristic size of each damage zone (c = the cubed root of damage zone volume) after each bout of loading, the number of cycles between the two bouts of loading and the local stress range (von Mises) determined from high-resolution finite element models (10 µm elements, 31-98 million elements/model, see Methods, Figure 4.2A). Damage growth rate was assessed once at each of the 49-287 damage zones in each specimen (1,676 damage zones in 11 specimens). This approach differs from traditional fatigue crack growth, which performs multiple measures of crack growth rate during advance of a single crack, an analysis which, to our knowledge, has been performed on only a few dozen cracks in cortical bone [35-37]. The observed damage zone propagation was consistent with the stable crack

growth rates of small cracks in cortical bone (Figure 4.2D, Figure 4.6 in ***Supplementary Materials***). Damage zone growth rate, however, was positively correlated with local stress intensity factor range within each donor (R^2= 0.51, $p < 0.001$), although large inter-individual variations were observed (color labels on Figure 4.2D). Damage zone growth rate was closely related to initial damage zone size (Figure 4.2C) and, interestingly showed little relationship to local cyclic stress range (Figure 4.7 in ***Supplementary Materials***). Larger damage zones were more likely to propagate during the second bout of loading; on average, 72% of damage zones created during the first bout of loading went on to propagate during the second bout of loading (Figure 4.8 in ***Supplementary Materials***).

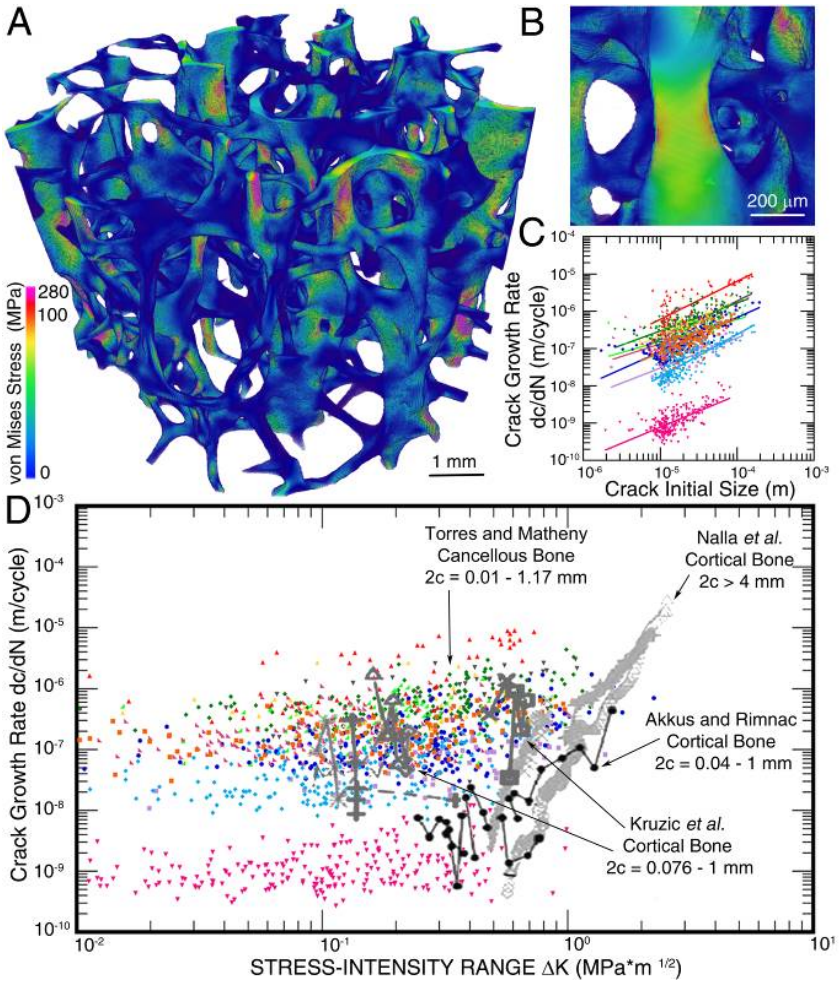

Figure 4.2. Fatigue crack growth within cancellous bone. (A) The distribution of von Mises stress within trabecular bone is shown. (B) Regions of greatest tissue stress were located at surfaces of trabeculae, suggesting that trabeculae experience bending and torsional loading. (C) Damage zone growth rate is expressed as the rate of change in damage zone size, c, divided by the applied number of cycles, N. Damage zone growth was strongly correlated with the size of the damage zone present before the second bout of loading ($p < 0.001$), but showed no correlation to local cyclic stress ($R^2 = 0.006$) (Figure 4.7 in ***Supplementary Materials***). (D) Data from the current study (colored points) is shown overlaid with fatigue crack growth measured in cortical bone (a summary of the literature from [35]). Positive relationships between crack growth rate (experimental data) and stress intensity range (finite element model data and experimental data) were observed within each specimen ($p < 0.001$). Data points with the same colors are from the same specimen.

To further understand the limited association between local tissue stress and damage propagation, we determined the local tissue stresses at damage zones (Figure 4.9A in ***Supplementary Materials***). The struts within cancellous bone commonly experience bending and

torsional loads, leading to the greatest tissue stresses at strut surfaces [38]. Tissue stresses at strut surfaces were greatest on the surfaces of trabeculae (Figure 4.2B, Figure 4.9B in ***Supplementary Materials***). However, the majority of tissue damage (68%) occurred in the central regions of trabeculae. Damage zone propagation also occurred predominately in the interior of the trabeculae (Figure 4.3C). Rupture of individual trabeculae, also known as trabecular microfracture, was rarely observed. The percent of trabeculae in a specimen that ruptured ranged from 0.06-1.32% (0.47 ± 0.36%, mean ± SD), demonstrating that failure of individual struts was not a common occurrence. In summary, these results demonstrate that damage formed and propagated in the interior of struts despite the fact that the tissue level stresses were greater at surfaces than the interior.

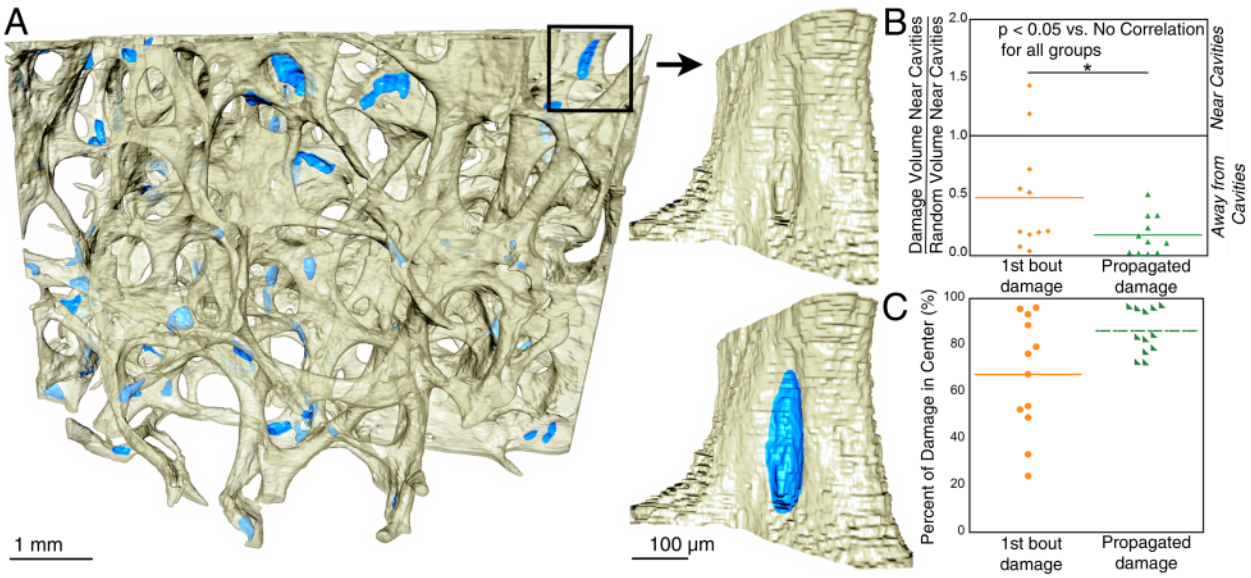

Figure 4.3. Tissue damage caused by fatigue loading is distant from stress concentrations generated by bone remodeling. (A) Remodeling cavities were traced manually and (B) damage zones were less likely to be near cavities than regions selected at random (the ratio is less than 1.0). (C) Damage initiated and propagated primarily in the interstitial regions in the center of trabeculae (more than the average depth of remodeling events, 30 µm).

4.5.2. Stress Concentrations on Trabecular Surfaces

To confirm our finding that local tissue stress was poorly correlated with damage propagation, we tested the idea that stress concentrations on the trabecular surfaces caused by bone remodeling were preferential locations of damage initiation and propagation. When old or damaged bone tissue is removed during bone remodeling, a cavity is generated on the trabecular surface that can increase local stresses by more than an order of magnitude [20], an increase expected to promote damage initiation and propagation [39]. However, we found remodeling cavities (54-111 per specimen, Figure 4.3A) were preferentially distant from damage zones (Figure 4.3B). One possible explanation is that trabeculae with cavities experience less stress because load is distributed preferentially to more robust trabeculae that do not have cavities. Additionally there is evidence that the generation of remodeling cavities *in vivo* occurs primarily on trabeculae experiencing less load [40]. However, in our analysis, stresses at remodeling cavities were similar to those at other trabecular surfaces (Figure 4.10 in ***Supplementary Materials***) demonstrating that trabeculae with cavities were not under-loaded. Hence we conclude that geometric discontinuities associated with the cavities did not lead to the creation or propagation of damage zones. To further assess the unexpected negative correlation between cavities and damage zones, we repeated our analysis considering only the cavities with the largest gross stress concentration factor (greatest ratio of cavity depth to strut thickness). The deepest cavities were even less likely to be near damage zones when compared to all of the cavities ($p < 0.05$, Figure 4.11 in ***Supplementary Materials***). The results indicate that geometric discontinuities such as remodeling cavities have little effect on damage zone initiation or propagation.

4.5.3. Patterns of Tissue Damage Reflect Accumulation of Advanced Glycation End products (AGEs)

To determine if patterns of material heterogeneity were consistent with regions of damage propagation, we determined the distribution of advanced glycation end products in cancellous bone from the same donor cohort. AGEs accumulate in bone tissue over time, and are found in higher concentrations in regions of bone tissue that has been present in an individual for a longer period of time. AGEs have been associated with non-enzymatic collagen cross-linking and increased tissue level brittleness [41, 42]. Higher concentrations of fluorescent AGEs were present in the central regions of the trabeculae (Figure 4.4). In summary, the presence of fluorescent AGEs, a factor associated with reduced ductility, was greater in the same regions where microscopic tissue damage was more likely to occur.

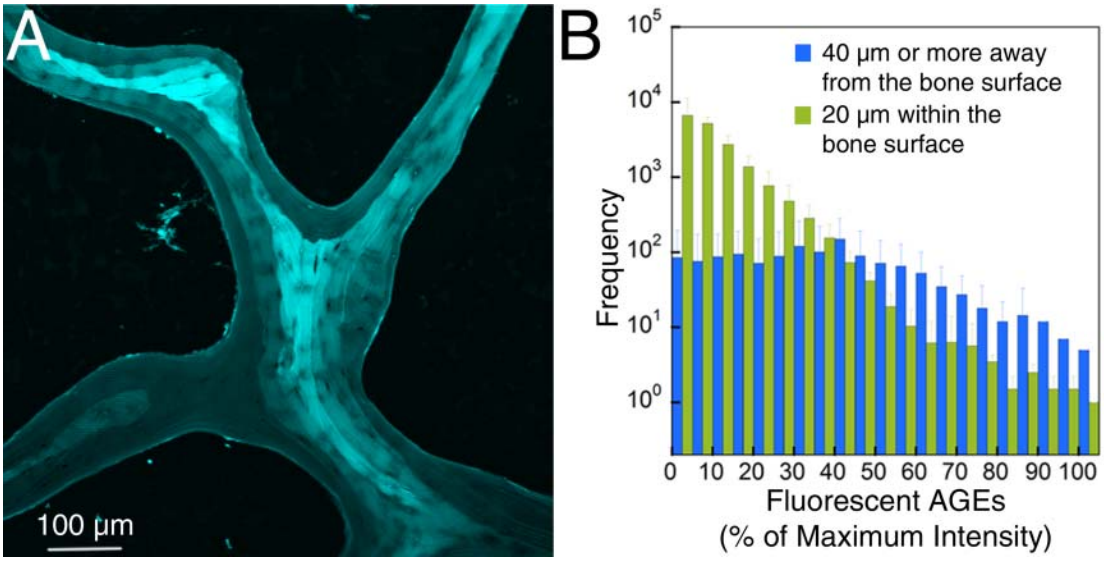

Figure 4.4. Advanced Glycation End products (AGEs) in cancellous bone are primarily found distant from the trabecular surface. (*A*) Fluorescence image of decalcified human vertebral cancellous bone. Regions of increased brightness indicate accumulation of advanced glycation end products. (*B)* The pixel intensity 40 μm or more away from the surface (blue) and within 20 μm of the bone surface (green) for a donor. The brightest regions were more than 40 μm away from the surface indicating high AGE content occurs primarily in the center of trabeculae.

4.6. Discussion

This work provides the first experimental analysis of damage propagation within the struts of an open-cell foam. The findings demonstrate that accumulation of tissue damage in cancellous bone is predominately the result of propagation from previously existing damage and that propagation of tissue damage occurs distant from regions of high stress due to material heterogeneity. As a result, the likelihood that a damage site will propagate is related to damage zone size instead of the magnitude of the local stress. Small damage events are less likely to propagate, while all large damage sites propagate. The results are consistent with the concept that failure of cancellous bone under fatigue is a localized process; once damage forms in a location; additional accumulation of tissue damage is a result of propagation rather than the initiation of new damage sites.

Stress concentration features that are physically small can be ineffective at initiating cracks [43], a fact that would suggest that the locations of damage zones might be indifferent to the presence of remodeling cavities. Damage zones were not found near remodeling cavities; instead we found that damage propagation was preferentially distant from surfaces with remodeling cavities, implying that differences in tissue material properties at surfaces and the interior are dominating damage propagation. The accumulation of tissue damage in the centers of trabeculae is also consistent with variation in material properties between material at the surface and the interstitial material in the interior of trabeculae. The central interstitial regions of trabeculae have been present longer in the body because bone remodeling initiates at trabecular surfaces. Tissue present in the body longer accumulates greater amounts of advanced glycation end products (AGEs) and associated increases in collagen cross-links as well as altered in mineral composition (increased degree of mineralization and crystallinity), traits that have been

associated with increased hardness [44, 45], increased brittleness [42], and reduced ductility [9, 14] of bone material. The current study directly demonstrates increased accumulation of AGEs in the centers of trabeculae suggesting that reductions in ductility and fracture toughness associated with increased non-enzymatic collagen cross-linking are the likely causes of observed damage patterns. Hence, our observations that damage zones initiate and propagate preferentially distant from cavities and strut surfaces are consistent with the idea that material heterogeneity, specifically increased surface ductility compared to the interior of trabeculae, directs damage propagation.

The observation that cancellous bone displays a more ductile surface and less ductile center was surprising in that it contrasts with surface treatment strategies used to increase fatigue life of man-made materials via surface hardening treatments [46]. The presence of a more ductile surface provides two key functional advantages to a biological foam. First, the presence of more ductile trabecular surfaces makes the material less sensitive to surface flaws and stress concentrations that are unavoidable in biological materials. Without this pattern in tissue heterogeneity, stress concentrations caused by self-healing processes such as bone remodeling could promote failure in cancellous bone. Hence, our findings contradict a long—held assumption that cavities generated by the activity of osteoclasts during the bone remodeling process weaken cancellous bone [39, 47]. Second, the presence of a more ductile strut surface forces tissue damage and associated permanent deformations into strut centers. Deformations in struts caused by bending and torsion (the primary loading modes experienced by trabeculae) are small near strut centers (neutral axis/center of twist). As a result, permanent deformations caused by tissue damage in strut centers are much smaller than would be expected if damage were

instead present at strut surfaces. Upon unloading, struts that accumulate tissue damage in the center (where stresses are lower) will recover more deformation from bending and torsion than struts accumulating damage at surfaces. Improved recovery of deformation of individual struts then leads to improved recovery of deformation of the entire foam structure.

Cancellous bone has long been recognized for the ability to recover large amounts of deformation after an overload; specimens compressed well beyond ultimate strain typically recover 61-94% of applied deformation [48-50]. The ability to recover deformation in cancellous bone allows for recovery of shape of whole bone after a fracture, and is therefore a passive mechanism of "setting" or reducing a fracture. By immediately recovering deformation of the whole bone, subsequent self-healing will maintain a structure more similar to the initial bone shape and lead to better function post-injury [48].

The ability of cancellous bone to recover deformation after failure provides a compelling answer to a long-standing question: why do bones have foam-like regions at all? A common explanation for the presence of a foam core in bone is to improve flexural and torsional rigidity and prevent buckling (crimping) [2]. However, in long bones the foam-like cancellous bone is present at the ends of the bones near the joints where they would provide relatively little contribution to flexural rigidity and resistance to buckling. The second common explanation for the presence of cancellous bone is improved energy absorption at joints, but energy absorption per unit mass is less in cancellous bone than in solid cortical bone [51]. In contrast, recovery of bone shape after fracture, especially at the joints where cancellous bone is most common, is key to enabling effective healing and locomotion after mechanical failure. We suggest that cancellous bone does not so much improve stiffness, strength and energy absorption, but

improves performance of the whole bone after failure.

The observed failure mechanisms of cancellous bone provide an attractive strategy for the design of biomimetic materials. Additive manufacturing techniques have achieved materials with designed microstructures that display large amounts of deformation recovery [3]. These strategies, however, concentrate on microstructural heterogeneity and mechanical performance prior to failure but do not necessarily consider material heterogeneity and performance of the component after failure has occurred [1, 2]. Lightweight, man-made components utilizing foams treated to increase surface ductility have the potential to continue to provide some mechanical function after overt failure, thereby providing longer service life in cases where replacement and repair are not immediately possible.

4.6. Acknowledgements

Research reported in this publication was supported by the National Institute of Arthritis and Musculoskeletal and Skin Diseases of the National Institutes of Health (U.S) under Award Number AR057362 (PI CJH). The content is solely the responsibility of the authors and does not necessarily represent the official views of the National Institutes of Health. We acknowledge use of human vertebral bodies provided by the National Disease Research Interchange (NDRI), with support from NIH grant 8U42OD011158-22. Cornell's NSF DGE-1144153. NSF GRFP (AMT). NSF GRFP (JBM). Cornell Colman Fellowship (AMT). We thank Christopher Chapa and Floor Lambers for assistance with specimen preparation. We thank Matthew Goff for assistance with finite element models. Imaging data was acquired in the Cornell BRC-Imaging Facility using the shared, NIH-funded (S10RR025502) Zeiss LSM 710 Confocal.

4.7. Supplemental Materials

Table 4.1. Damage volume fraction measurements

Damage Measure	Mean ± SD
Total damage volume fraction (1st + 2nd bout, DV/BV, %)	5.13 ± 2.04
1st bout damage volume fraction (DV/BV, %)	0.96 ± 0.58
2nd bout initiated damage volume fraction (DV/BV, %)	0.41 ± 0.24
2nd bout propagated damage volume fraction (DV/BV, %)	3.45 ± 1.74

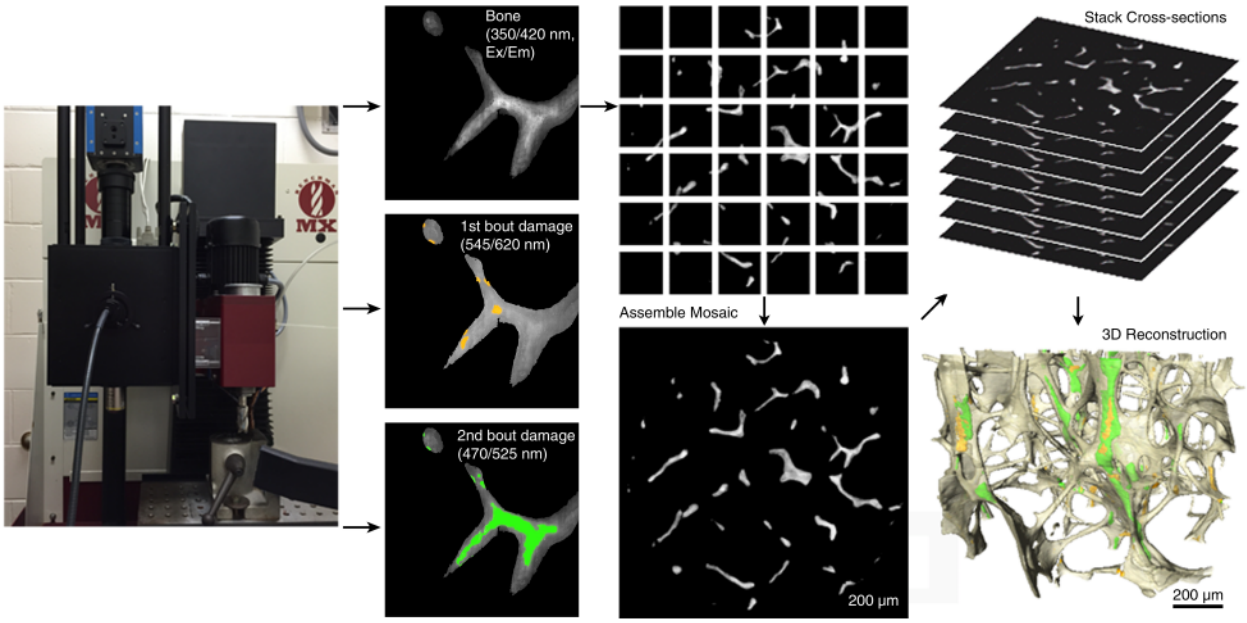

Figure 4.5. Serial milling imaging of microdamage is shown. Fluorescent light images of bone were acquired using UV excitation/emission (350/420 nm), with voxel sizes of 0.7×0.7×5.0 µm. Raw images were collected using this resolution consist of 800 transverse cross-sections, each consisting of a 6×6 mosaic of images.

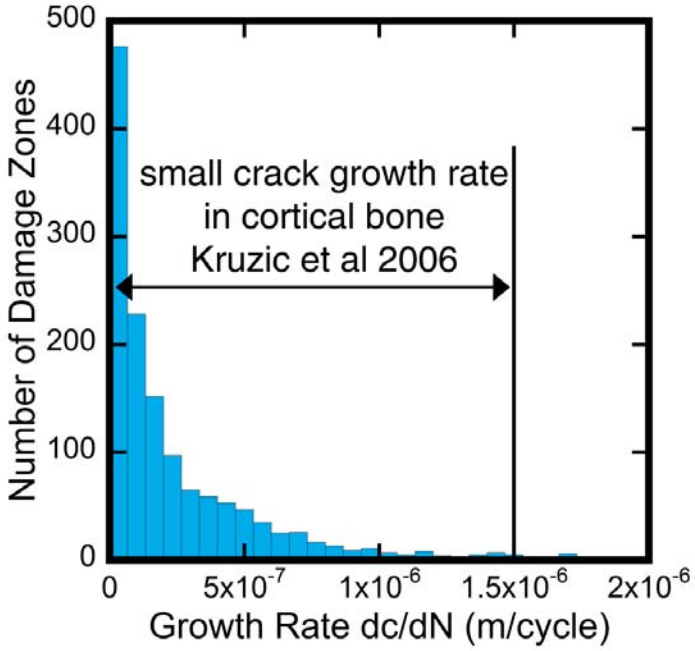

Figure 4.6. The distribution of damage zone growth rate for all specimens is shown. All but a few damage zones grew at rates within the range of small crack growth observed in cortical bone [35].

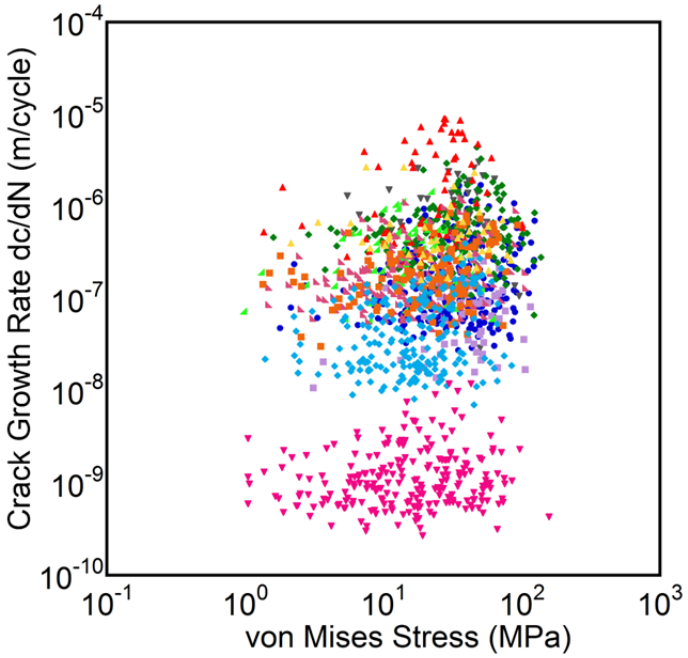

Figure 4.7. Damage zone growth rate collected from the experimental data was not related to local tissue stresses calculated from the finite element models ($R^2 = 0.006$). Data points with the same color are from the same specimen.

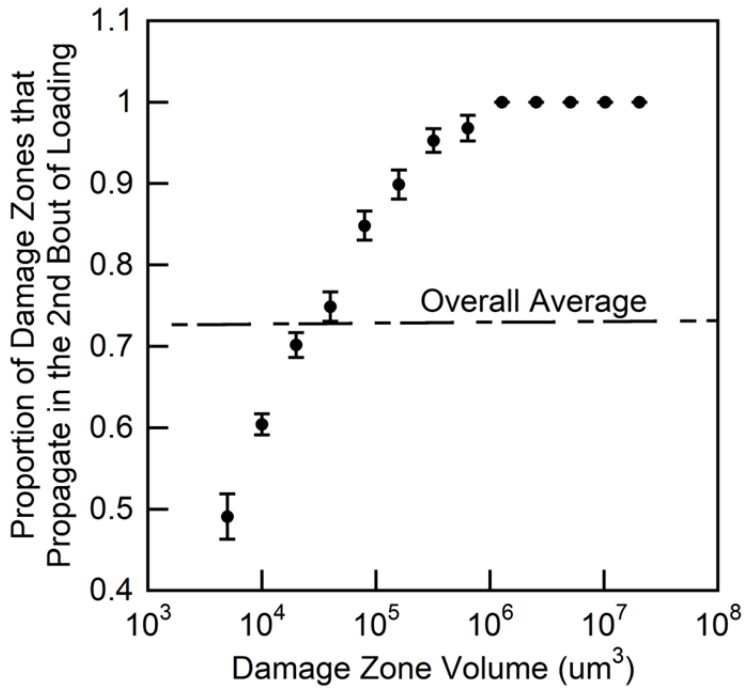

Figure 4.8. Probability of damage zone propagation during the second bout of loading is shown (mean ± SE). Larger microdamage sites were more likely to propagate. The overall average proportion of damage zones propagating was 0.72.

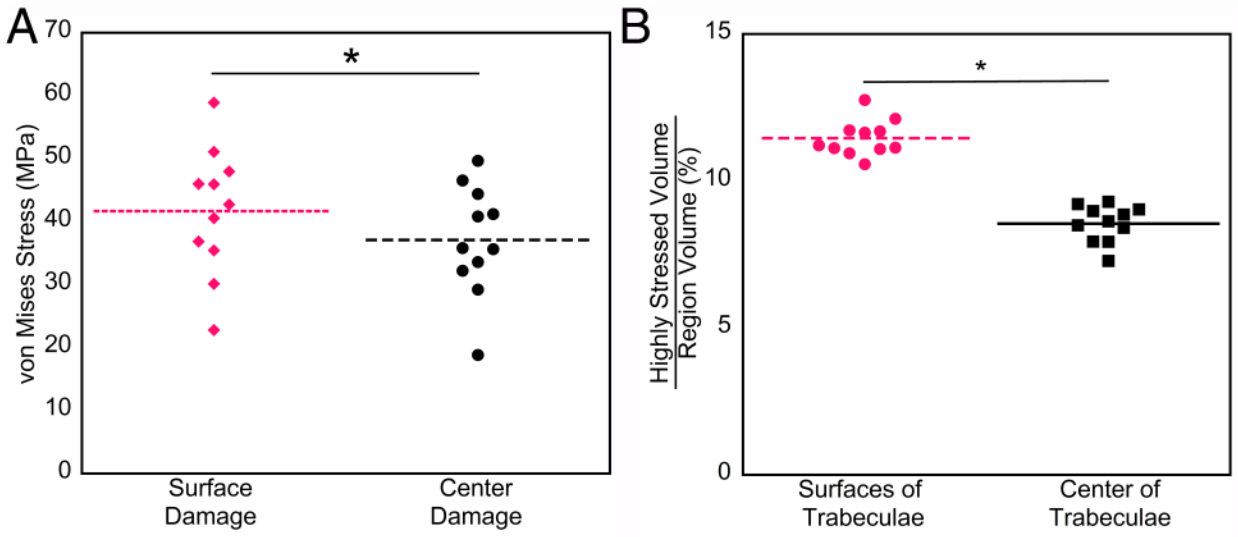

Figure 4.9. (A) Stresses of damage zones at the surfaces of trabeculae are greater compared to the center of trabeculae ($p < 0.01$). (B) Stresses at the surfaces of trabeculae are greater than at the center of trabeculae ($p < 0.01$).

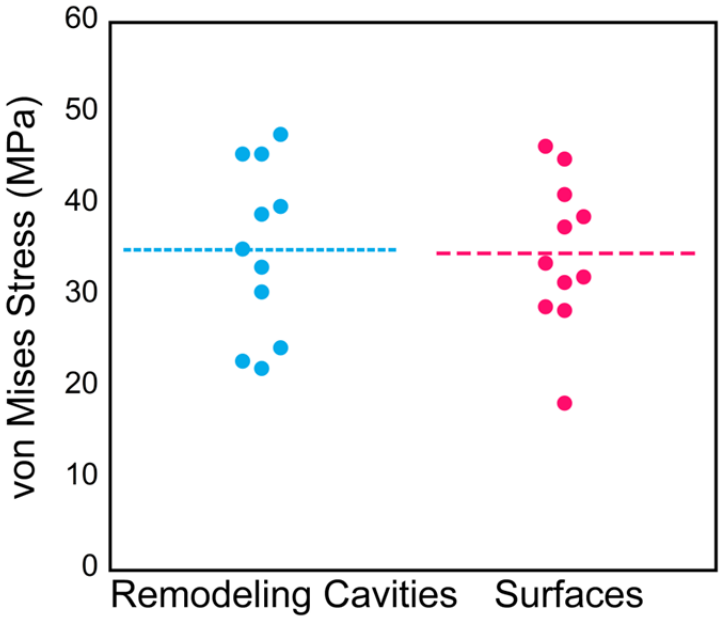

Figure 4.10. Stresses at remodeling cavities were not different from those at other regions of the surface at the resolution of the finite element models ($p = 0.82$, paired t-test), demonstrating that trabeculae with cavities were experiencing loads similar in magnitude to those at other regions of the microstructure.

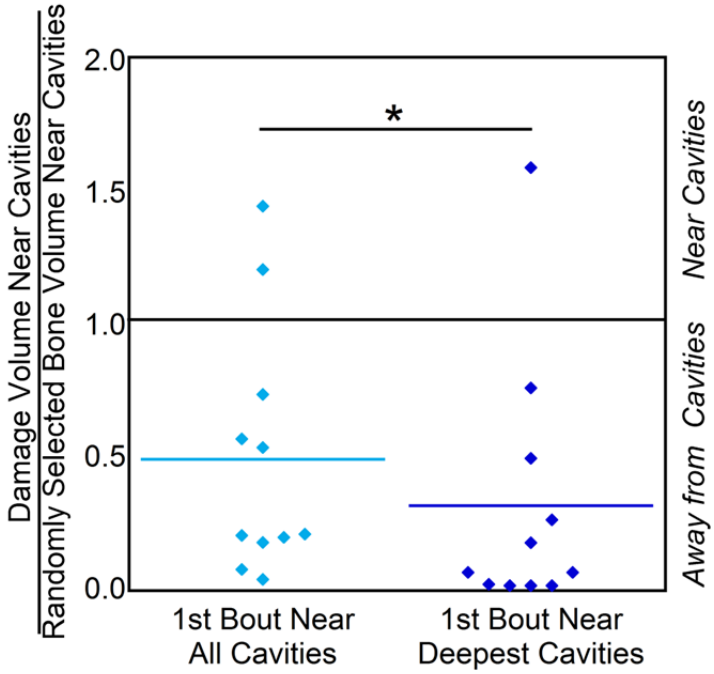

Figure 4.11. The deepest cavities (with greatest gross stress concentration factor) were even less likely to be near damage zones when compared to all of the cavities ($p < 0.05$).

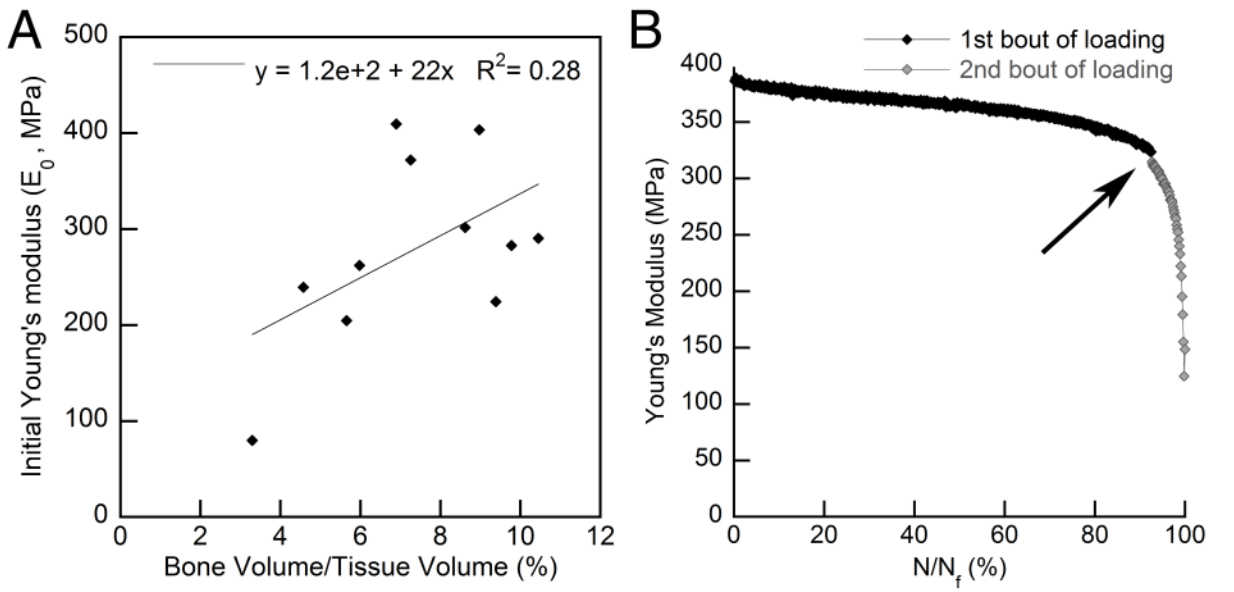

Figure 4.12. (A) Initial Young's modulus, E_0. Linear regression model of initial Young's modulus as a function of bone volume fraction ($R^2 = 0.28$). (B) Reductions in Young's modulus during fatigue loading. The reduction in young's modulus for the first bout of cyclic loading is shown in black, and the second bout of cyclic loading is shown in gray. A negligible reduction in Young's modulus was caused by interruption of loading (as indicated by the arrow).

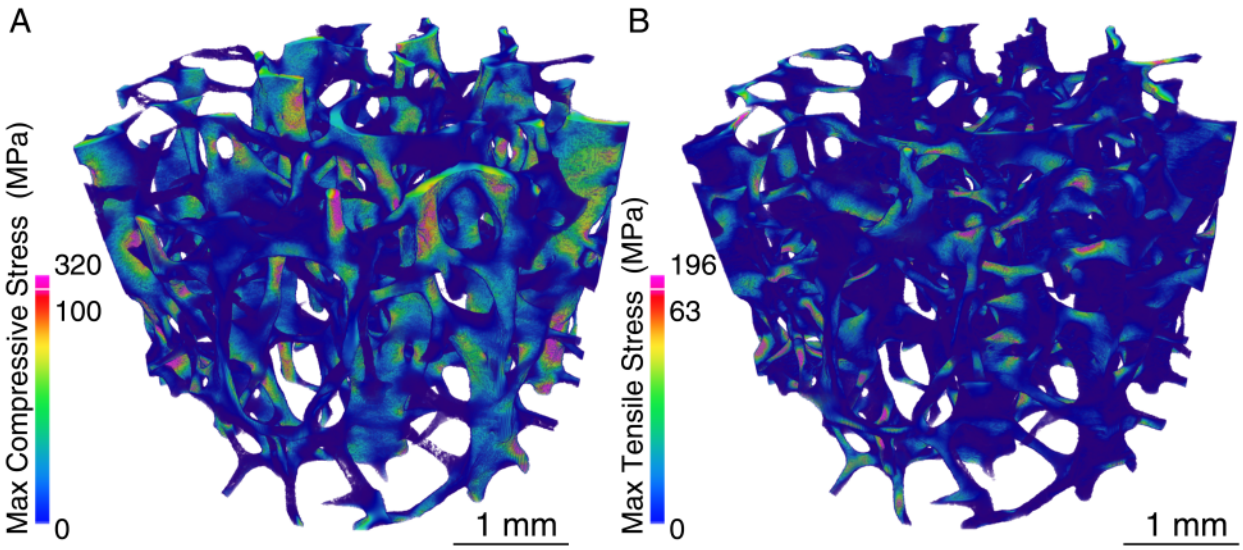

Figure 4.13. The distributions of maximum principal stress in tension and compression are shown. Although the specimen was loaded in apparent compression, regions of local tensile stress develop due to bending of trabeculae.

REFERENCES

[1] U.G. Wegst, H. Bai, E. Saiz, A.P. Tomsia, R.O. Ritchie, Bioinspired structural materials, Nat Mater 14(1) (2015) 23-36.

[2] M.A. Meyers, J. McKittrick, P.-Y. Chen, Structural Biological Materials: Critical Mechanics-Materials Connections, Science 339(6121) (2013) 773-779.

[3] L.R. Meza, A.J. Zelhofer, N. Clarke, A.J. Mateos, D.M. Kochmann, J.R. Greer, Resilient 3D hierarchical architected metamaterials, Proc. Natl. Acad. Sci. USA 112(37) (2015) 11502-11507.

[4] L.J. Gibson, Biomechanics of cellular solids, J Biomech 38(3) (2005) 377-399.

[5] R.O. Ritchie, M.J. Buehler, P. Hansma, Plasticity and toughness in bone, Phys Today 62(6) (2009) 41-47.

[6] R.K. Nalla, J.H. Kinney, R.O. Ritchie, Mechanistic fracture criteria for the failure of human cortical bone, Nat Mater 2(3) (2003) 164-8.

[7] K.J. Koester, J.W. Ager, 3rd, R.O. Ritchie, The true toughness of human cortical bone measured with realistically short cracks, Nat Mater 7(8) (2008) 672-7.

[8] M.E. Launey, M.J. Buehler, R.O. Ritchie, On the Mechanistic Origins of Toughness in Bone, Annu. Rev. Mater. Res. 40(1) (2010) 25-53.

[9] E.A. Zimmermann, E. Schaible, H. Bale, H.D. Barth, S.Y. Tang, P. Reichert, B. Busse, T. Alliston, J.W. Ager, R.O. Ritchie, Age-related changes in the plasticity and toughness of human cortical bone at multiple length scales, Proc. Natl. Acad. Sci. USA 108(35) (2011) 14416-14421.

[10] P. Zioupos, J.D. Currey, Changes in the stiffness, strength, and toughness of human cortical bone with age, Bone 22(1) (1998) 57-66.

[11] O. Akkus, K.J. Jepsen, C.M. Rimnac, Microstructural aspects of the fracture process in human cortical bone, Journal of Materials Science 35(24) 6065-6074.

[12] J.W. Ager, G. Balooch, R.O. Ritchie, Fracture, aging, and disease in bone, J. Mater. Res. 21(08) (2006) 1878-1892.

[13] X. Wang, X. Shen, X. Li, C. Mauli Agrawal, Age-related changes in the collagen network and toughness of bone, Bone 31(1) (2002) 1-7.

[14] D. Vashishth, G.J. Gibson, J.I. Khoury, M.B. Schaffler, J. Kimura, D.P. Fyhrie, Influence of nonenzymatic glycation on biomechanical properties of cortical bone, Bone 28(2) (2001) 195-201.

[15] D. Taylor, J.G. Hazenberg, T.C. Lee, Living with cracks: damage and repair in human bone, Nat Mater 6(4) (2007) 263-8.

[16] B. Busse, H.A. Bale, E.A. Zimmermann, B. Panganiban, H.D. Barth, A. Carriero, E. Vettorazzi, J. Zustin, M. Hahn, J.W. Ager, 3rd, K. Puschel, M. Amling, R.O. Ritchie, Vitamin D deficiency induces early signs of aging in human bone, increasing the risk of fracture, Sci Transl Med 5(193) (2013) 193ra88.

[17] P.L. Salmon, C. Ohlsson, S.J. Shefelbine, M. Doube, Structure model index does not measure rods and plates in trabecular bone, Front. Endocrinol. (Lausanne) 6 (2015) 1-10.

[18] R.A. Smith, K.J. Miller, FATIGUE CRACKS AT NOTCHES, International Journal of Mechanical Sciences 19(1) (1977) 11-22.

[19] J.C. van der Linden, J. Homminga, J.A. Verhaar, H. Weinans, Mechanical consequences of bone loss in cancellous bone, J Bone Miner Res 16(3) (2001) 457-65.

[20] L.M. McNamara, J.C. van der Linden, H. Weinans, P.J. Prendergast, Stress-concentrating effect of resorption lacunae in trabecular bone, J Biomech 39(4) (2006) 734-41.

[21] C.J. Hernandez, A. Gupta, T.M. Keaveny, A biomechanical analysis of the effects of resorption cavities on cancellous bone strength, J Bone Miner Res 21(8) (2006) 1248-55.

[22] S.K. Easley, M.T. Chang, D. Shindich, C.J. Hernandez, T.M. Keaveny, Biomechanical effects of simulated resorption cavities in trabecular bone across a wide range of bone volume fraction, J Bone Miner Res Submitted (2012).

[23] J. Vanderoost, G.H. van Lenthe, The effect of resorption cavities on bone stiffness is site dependent, Comput Methods Biomech Biomed Engin 17(13) (2014) 1483-91.

[24] W.D. Pilkey, Peterson's stress concentration factors, John Wiley & Sons, New York, NY, USA, 1997.

[25] B. Atzori, P. Lazzarin, A three-dimensional graphical aid to analyze fatigue crack nucleation and propagation phases under fatigue limit conditions, Int. J. Fract. 118(3) (2002) 271-284.

[26] M.G. Goff, C.R. Slyfield, S.R. Kummari, E.V. Tkachenko, S.E. Fischer, Y.H. Yi, M.G. Jekir, T.M. Keaveny, C.J. Hernandez, Three-dimensional characterization of resorption cavity size and location in human vertebral trabecular bone, Bone 51(1) (2012) 28-37.

[27] J.F. Griffith, H.K. Genant, New advances in imaging osteoporosis and its complications, Endocrine 42(1) (2012) 39-51.

[28] R.B. Cook, P. Zioupos, The fracture toughness of cancellous bone, J. Biomech. 42(13) (2009) 2054-60.

[29] F.J. O'Brien, D. Taylor, T.C. Lee, An improved labelling technique for monitoring microcrack growth in compact bone, J Biomech 35(4) (2002) 523-6.

[30] R.F. Bigley, M. Singh, C.J. Hernandez, G.J. Kazakia, R.B. Martin, T.M. Keaveny, Validity of serial milling-based imaging system for microdamage quantification, Bone 42(1) (2008) 212-215.

[31] C.R. Slyfield Jr, K.E. Niemeyer, E.V. Tkachenko, R.E. Tomlinson, G.G. Steyer, C.G. Patthanacharoenphon, G.J. Kazakia, D.L. Wilson, C.J. Hernandez, Three-dimensional surface texture visualization of bone tissue through epifluorescence-based serial block face imaging, Journal of Microscopy 236(1) (2009) 52-59.

[32] D.W. Dempster, J.E. Compston, M.K. Drezner, F.H. Glorieux, J.A. Kanis, H. Malluche, P.J. Meunier, S.M. Ott, R.R. Recker, A.M. Parfitt, Standardized nomenclature, symbols, and units for bone histomorphometry: A 2012 update of the report of the ASBMR Histomorphometry Nomenclature Committee, J. Bone Miner. Res. 28(1) (2013) 2-17.

[33] M.G. Goff, K.L. Chang, E.N. Litts, C.J. Hernandez, The effects of misalignment during in vivo loading of bone: Techniques to detect the proximity of objects in three-dimensional models, J. Biomech. 47(12) (2014) 3156-3161.

[34] M.F. Adams, H.H. Bayraktar, T.M. Keaveny, P. Papadopoulos, Ultrascalable implicit finite element analyses in solid mechanics with over a half a billion degrees of freedom, ACM/IEEE Proceedings of SC2004: High Performance Networking and Computing, 2004.

[35] J.J. Kruzic, J.A. Scott, R.K. Nalla, R.O. Ritchie, Propagation of surface fatigue cracks in human cortical bone, J Biomech 39(5) (2006) 968-72.

[36] R. Nalla, J. Stölken, J. Kinney, R. Ritchie, Fracture in human cortical bone: local fracture criteria and toughening mechanisms, J. Biomech. 38(7) (2005) 1517-1525.

[37] O. Akkus, C.M. Rimnac, Fracture resistance of gamma radiation sterilized cortical bone allografts, J. Orth. Res. 19(5) (2001) 927-934.

[38] G.A. Renders, L. Mulder, L.J. van Ruijven, G.E. Langenbach, T.M. van Eijden, Mineral heterogeneity affects predictions of intratrabecular stress and strain, J. Biomech. 44(3) (2011) 402-7.

[39] C. Hernandez, How can bone turnover modify bone strength independent of bone mass?, Bone 42(6) (2008) 1014-1020.

[40] R. Huiskes, R. Ruimerman, G.H. van Lenthe, J.D. Janssen, Effects of mechanical forces on maintenance and adaptation of form in trabecular bone, Nature 405(6787) (2000) 704-6.

[41] S. Tang, D. Vashishth, Non-enzymatic glycation alters microdamage formation in human cancellous bone, Bone 46(1) (2010) 148-154.

[42] J.C.I. Catanese, R.A. Bank, J.M. TeKoppele, T.M. Keaveny, Increased cross-linking by non-enzymatic glycation reduces the ductility of bone and bone collagen, Proc. Bioeng. Conf., 1999, pp. 267-68.

[43] D. Taylor, The theory of critical distances, Elsevier, London, UK, 2007.

[44] O. Brennan, O.D. Kennedy, T.C. Lee, S.M. Rackard, F.J. O'Brien, Biomechanical properties across trabeculae from the proximal femur of normal and ovariectomised sheep, J Biomech 42(4) (2009) 498-503.

[45] J.C. Burket, D.J. Brooks, J.M. MacLeay, S.P. Baker, A.L. Boskey, M.C.H. van der Meulen, Variations in nanomechanical properties and tissue composition within trabeculae from an ovine model of osteoporosis and treatment, Bone 52(1) (2013) 326-336.

[46] N.E. Dowling, Mechanical Behaviour of Materials, Third Edition ed., Pearson Prentice Hall, Upper Saddle River, NJ, USA, 2007.

[47] D.W. Dempster, The contribution of trabecular architecture to cancellous bone quality, J. Bone Miner. Res. 15(1) (2000) 20-23.

[48] D.P. Fyhrie, M.B. Schaffler, Failure mechanisms in human vertebral cancellous bone, Bone 15(1) (1994) 105-9.

[49] T.M. Keaveny, E.F. Wachtel, D.L. Kopperdahl, Mechanical behavior of human trabecular bone after overloading, J Orthop Res 17 (1999) 346-53.

[50] C.J. Hernandez, F.M. Lambers, J. Widjaja, C. Chapa, C.M. Rimnac, Quantitative relationships between microdamage and cancellous bone strength and stiffness, Bone 66 (2014) 205-13.

[51] J.D. Currey, Bones: Structure and Mechanics, Princeton University Press, Princeton, NJ, USA, 2002.

CHAPTER 5
AN IN VIVO MODEL OF A MECHANICALLY-INDUCED BONE MARROW LESION

The following chapter has been submitted for publication. The article is titled “An In Vivo Model of a Mechanically-Induced Bone Marrow Lesion” by Matheny JB, Goff MG, Pownder SL, Koff MF, Hayashi K, Yang X, Bostrom MPG, van der Meulen MCH, Hernandez CJ.

5.1. Abstract

Bone marrow lesions (BMLs) are radiologic abnormalities in magnetic resonance images of subchondral cancellous bone and have been correlated with the development of osteoarthritis. Little is known about the physiologic processes within a BML, but BMLs are often associated with mechanical stress, bone tissue microdamage and increased bone remodeling. Here we establish a rabbit model to study the pathophysiology of BMLs. We hypothesized that *in vivo* loads that generate microdamage in cancellous bone would also create BMLs and increased bone remodeling. Cyclic loads (0.2 to 2.0 MPa in compression for 10,000 cycles at 2 Hz) were applied to cancellous bone *in vivo* (n = 3 animals, right limb loaded, left limb controls experienced surgery but no loading). Magnetic resonance images were collected using STIR and T1 weighted sequences at 1 and 2 weeks after surgery/loading and histological analysis of the BML was performed after euthanasia to examine tissue microdamage and remodeling. Loaded limbs displayed BMLs larger than unloaded controls ($p = 0.01$). Histological analysis of the BML at 2 weeks after loading showed increased tissue microdamage ($p = 0.03$) and bone resorption ($p = 0.01$). The rabbit model described here displays the hallmarks of load-induced BMLs, supporting the use of the model for more detailed studies of the development, progression and treatment of BMLs. Clinical evidence suggests that BMLs may be an early indicator of, or contributor to, cartilage degeneration. The current study provides an animal model to understand the pathophysiology of BMLs.

5.2. Introduction

Bone marrow lesions (BMLs) or "bone marrow edema patterns" occur due to chronic and acute joint disorders and manifest as an increase of signal intensity in water sensitive magnetic resonance imaging sequences in subchondral cancellous bone. In longitudinal studies the presence and growth of bone marrow lesions are associated with increased risk of joint degeneration leading to total joint arthroplasty [1-3]. Bone marrow lesions have been observed in patients prior to clinical symptoms of osteoarthritis and, unlike articular cartilage degeneration, may be reversible raising the possibility that bone marrow lesions may be an indicator of early stage osteoarthritis or even a therapeutic target to prevent cartilage degeneration [4-7].

The etiology and pathophysiology of bone marrow lesions is poorly understood, but appears to be associated with mechanical stresses in cancellous bone. Bone marrow lesions associated with osteoarthritis occur in regions of subchondral bone experiencing greater habitual stresses [8, 9]. Biopsies of bone marrow lesions acquired at the time of total joint arthroplasty show microscopic cracks and other tissue damage [10] as well as increased bone remodeling [11], woven bone formation, and increased angiogenesis [12]. These findings are consistent with the idea that bone marrow lesions involve mechanically-induced tissue damage and bone remodeling. However, a limitation of biopsies is that they are acquired at the time of total joint replacement and therefore provide little information about the sequence of events in the early, reversible stages of bone marrow lesions.

Given the challenges in characterizing the pathophysiology of early stage bone marrow lesions in patients, a pre-clinical model that recapitulates the pathogenesis of a bone marrow lesion would be valuable for understanding the natural history of bone marrow lesion development and progression. In rodents, transection of the anterior cruciate ligament can result in bone marrow lesions [13] and tissue microdamage [14] prior to cartilage degeneration. Additionally some rodent studies have associated increased bone remodeling with subsequent articular cartilage degradation [13, 14]. These findings are consistent with long standing theories that load-induced microdamage and increased bone remodeling contribute to the pathogenesis of osteoarthritis [15, 16]. While rodent models are useful for studying surgically-induced cartilage degeneration, regions of cancellous bone in mice and rats are small, limiting our ability to characterize the biological and mechanical processes within a bone marrow lesion. In addition, the small anatomy frequently prevents the use of non-invasive imaging using clinical equipment, hampering translation to the clinical setting.

The goal of this line of investigation was to understand the pathophysiology of bone marrow lesions. Here we establish an animal model of mechanically-induced bone marrow lesions focusing on two specific hypotheses. First, we hypothesized that the loads required to generate microdamage in subchondral cancellous bone would also create bone marrow lesions. Second, we hypothesized that regions of cancellous bone receiving cyclic loading and forming bone marrow lesions would correspond with increased bone remodeling. The initiation and progression of bone marrow

lesions will be evaluated using non-invasive, clinical field strength MRI, and the amount of microdamage and bone resorption will be evaluated histologically following euthanasia.

5.3. Materials and Methods

Given the association between mechanical loading and bone marrow lesions, we adapted an *in vivo* loading model in the rabbit to generate a bone marrow lesion. The rabbit loading model has been used extensively to study functional adaptation in cancellous bone [17-19] and implant osseointegration [20-22]. In the model, an implant is placed on the lateral distal femur. The cortex under the implant is removed, and mechanical loads are applied directly to the epiphyseal cancellous bone through a loading core (Figure 5.1).

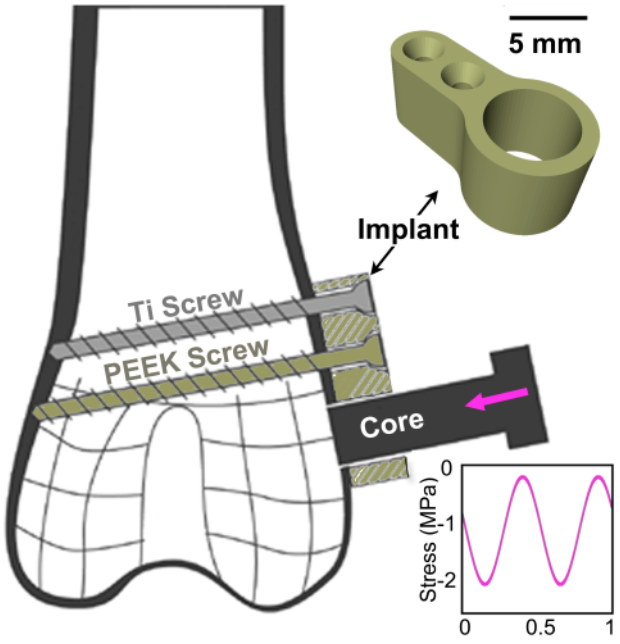

Figure 5.1. The rabbit *in vivo* loading device is shown. A PEEK implant (gold) was surgically fixed to the lateral epiphysis of the distal femur by Titanium and PEEK bicortical screws. The cortex below the implant was removed allowing for cyclic compressive loads to be applied to the underlying cancellous bone by the loading core.

Loads were applied for 10,000 cycles at 2 Hz immediately following device implantation. The loading core was removed prior to closing the surgical site.

In the current implementation, the loading device was implanted by a board certified veterinary surgeon (KH). Prior to implantation, a 17 mm x 9 mm region of the cortex located distal to the lateral femoral growth plate were ground flat using 6.5 and 5 mm spherical cutting burrs. A polyether ether ketone (PEEK) implant was placed on the lateral epiphyseal cortex of the distal femur. The implant was secured to the femur using a 2 mm diameter PEEK screw and a 1.5 mm diameter titanium screw (see Figure 5.1). The use of PEEK implants avoids metallic susceptibility artifact during magnetic resonance imaging (MRI) of tissues immediately adjacent to the implanted material. Following placement of the implant, the cortex (1 mm thickness) beneath the implant was removed using a custom routing device (diameter 4.75 mm). An aluminum loading core aligned with the implant was placed through the hole in the cortex and cyclic loading was applied directly to the underlying cancellous bone using a servo-electric loading device (Testbench, Bose Electroforce) (Figure 5.1).

5.3.1 In Vivo Loading and Visualization of Bone Marrow Lesions

Animal experiments were performed following approval by the Cornell University Institutional Animal Care and Use Committee in an AAALAC-accredited facility. Male, New Zealand white rabbits (n=3, 7.5 months old, 3.56±0.42 kg, Covance Inc., Princeton, NJ) were housed individually in stainless steel cages in a room with a 12:12 hour light: dark cycle and temperature between 18.9 to 21.1 °C. Rabbits were fed Teklad 15% rabbit diet 8630 (Envigo, Madison, WI) and water *ad libitum* and provided environmental enrichment. Following 2 weeks of acclimation,

animal were anesthetized with isoflurane and the implants were placed bilaterally using a posterior lateral surgical approach. The right limbs received implants and were loaded in cyclic compression between 0.2 MPa (minimum) and 2.0 MPa (maximum) at 2 Hz frequency for 10,000 cycles. The left limb received an implant but no load was applied. Prior to closing the surgical site, a PEEK cap was secured within the implant to occupy the hole in the cortex. Wounds were washed with antiseptic, and an antibiotic prophylaxis was applied the day of surgery (25 mg/kg ampicillin). Rabbits received buprenorphine (0.05 mg/kg) analgesic for 2 days after surgery.

At one and two weeks after surgery/loading, animals were anesthetized, and both limbs were evaluated using a clinical 3T MRI scanner (DVMR 750, GE Healthcare, Milwaukee WI) with an 8 channel phased-array transmit/receive (T/R) knee coil (Invivo, Gainesville, FL). T1-weighted and fat-suppressed short tau inversion recovery (STIR) images were collected to visualize BMLs. BMLs were identified and manually segmented by a board certified veterinary radiologist (SLP) using a combination of the STIR and T1 weighted images. BML volume (in mm^3) was calculated as the area of the BML within individual slices multiplied by slice thickness [2, 23]. Animals were euthanized via an intravenous injection of pentobarbital sodium (86 mg/kg FatalPlus, Vortech Pharmaceuticals, Dearborn MI) immediately following acquisition of the second MRI dataset.

Following euthanasia, the limbs were dissected free from soft tissue, implants were removed, and microcomputed tomography images of each femur were collected at an isotropic voxel size of 50 μm (eXplore CT-120, GE Healthcare, Milwaukee WI).

The lateral epiphysis of each femur was dissected using a low speed precision saw (IsoMet Low Speed Saw, Buehler, Lake Bluff, Illinois USA), and bone marrow was removed using a low-pressure water jet. To identify microscopic tissue damage, specimens were bulk stained in calcein solution (0.5 mM) for two hours under vacuum. Specimens were then embedded undecalcified in polymethyl- methacrylate, and sections from the coronal plane were collected and polished to 100 μm thickness. Images of the sections were obtained using a confocal microscope (Zeiss LSM 710 Confocal Carl Zeiss, Inc., Thornwood, NY USA) to obtain a mosaic of images (4.08 × 4.08 mm), 2.4 μm thick, with a pixel size of 0.66 μm. A rectangular region of interest (width 3.0 mm, height 3.7 mm) located 500 microns away from contact with the loading core was selected for analysis. Damage volume fraction (DV/BV, %), and eroded surface (ES/BS, %), identified as scalloped or crenated surfaces, were measured using point counting (21 μm grid spacing). The MR images, microcomputed tomography images and histology sections were aligned with each other in three dimensions using commercial software to allow co-localization between trabecular microstructure, histology and MRI (Amira, version 5.3, Visage Imaging, San Diego, CA, USA).

All analyses were conducted using automated approaches or by trained observers blinded to specimen loading history. The current study builds on prior pilot studies (see Figures 5.5 – 5.7 in ***Supplementary Materials***) in which the cyclic loading parameters were identified and shown to generate tissue microdamage in cancellous bone without causing overt fracture. Additionally, the time period of applied loading

(83 minutes) was within a reasonable duration of anesthesia (as viewed by veterinary staff and KH).

5.3.2. Statistical Analysis

Differences in damage volume fraction and eroded surface between loaded and unloaded groups were identified using two-tailed, paired t-tests (JMP Pro 10.0.2, SAS Institute Inc., Cary, NC, USA). The effect of *in vivo* loading on BML volume was determined using repeated measures ANCOVA implemented with a generalized least squares model using time and limb (loaded, non-loaded) as fixed effects and animal as a random effect. Data are presented as mean ± SD.

5.4. Results

Following surgery and cyclic loading *in vivo*, BMLs were apparent in loaded limbs in both STIR and T1 weighted MR sequences at one and two weeks after surgery/applied loading (Figure 5.2). BMLs were present in loaded limbs and small BMLs were present in control limbs. BMLs in loaded limbs were larger in volume and extended farther from the surface of applied loading than the BML signal in control limbs (Figure 5.3). BML volumes were 26.27 ± 19.13 mm^3 one week after loading and 35.97 ± 11.49 mm^3 two weeks after loading. In contrast, BMLs in control limbs were smaller than BMLs in loaded limbs ($p=0.01$ vs. loaded volumes, 9.60 ± 10.87 mm^3 and 10.97 ± 3.68 mm^3 at one and two weeks, respectively). The signal in the control limbs appeared closer to the surface and was likely associated with the surgery induced damage on the surface.

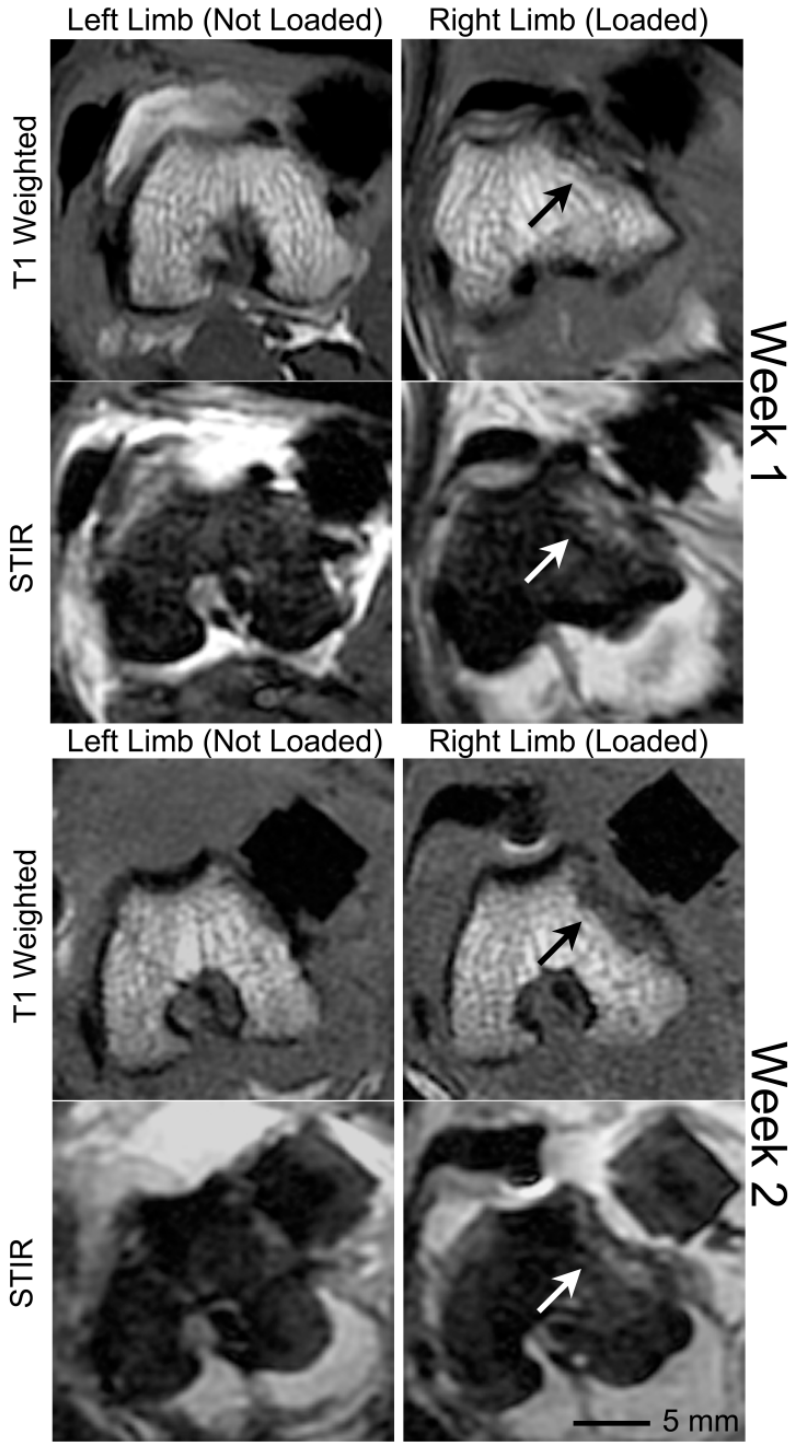

Figure 5.2. *In vivo* cyclic loading applied to epiphyseal cancellous tissue of the distal femur of the rabbit induced the formation of bone marrow lesions evident 1 and 2 weeks after loading. T1 weighted and STIR MR images collected at 1 and 2 weeks after surgery/loading. Bone marrow lesions in the loaded limbs are indicated with arrows.

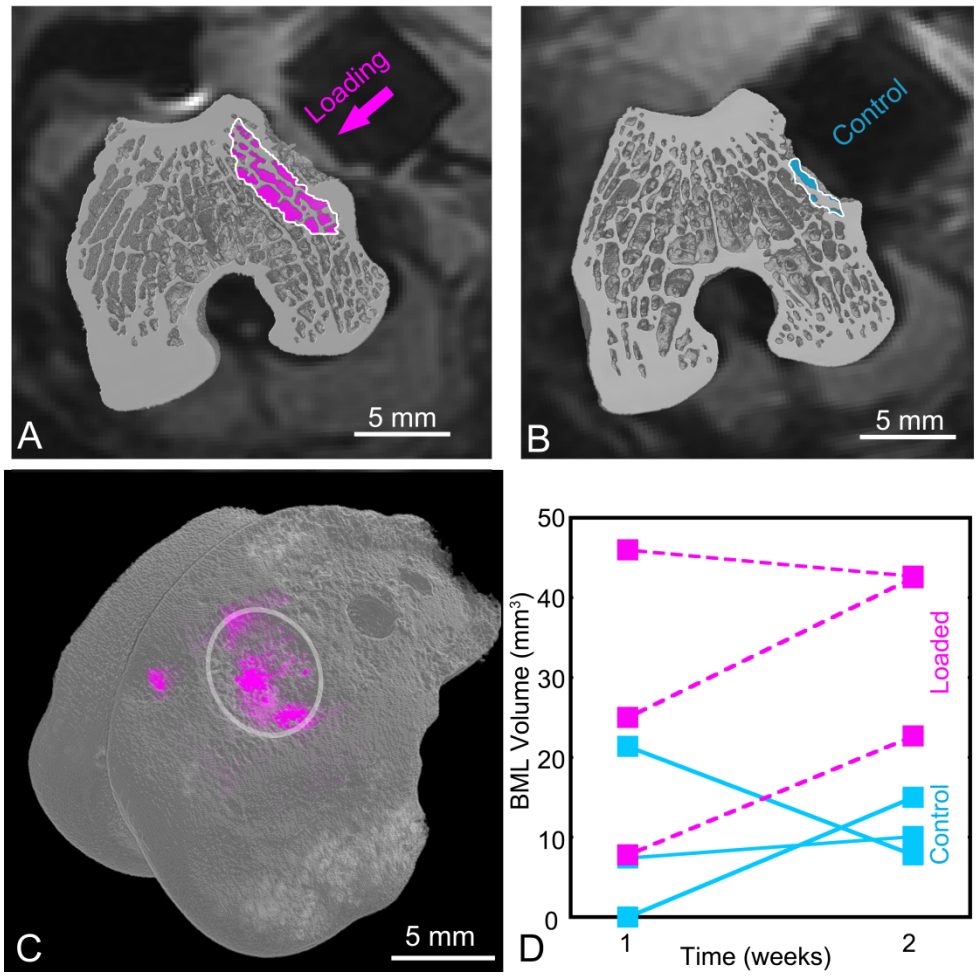

Figure 5.3. BMLs in loaded limbs were larger in volume and extended farther from the surface of applied loading than the BML signal in adjacent to surgery in control limbs. (A-B) MicroCT images overlaid on STIR MR images collected at 2 weeks after loading are shown. The BML in loaded limbs (magenta) and BML signal in control limb (blue) are shown. (C) A three-dimensional reconstruction of a microCT data set from a loaded limb is shown with partial transparency to enable visualization of the bone marrow lesion (BML, magenta) in relation to the location of applied loading (white circle). (D) BML volume was larger in loaded than in control limbs.

Bone tissue collected from BMLs had tissue microdamage and evidence of increased osteoclast activity at two weeks after surgery/loading (Figure 5.4A-C). Loaded limbs had substantially more calcein-stained microdamage (damage volume fraction: Loaded 3.7 ± 0.3% vs. Control 0.7 ± 0.7%, $p = 0.03$, see Figure 5.4D) and

evidence of greater osteoclast activity (eroded surface: Loaded 17.2 ± 2.72% vs. Control 6.21 ± 1.95%, $p = 0.01$, see Figure 5.4E) compared to contralateral control limbs. The amount of calcein-stained microdamage was correlated with BML volume ($R^2 = 0.85$, $p<0.009$, see Figure 5.4F).

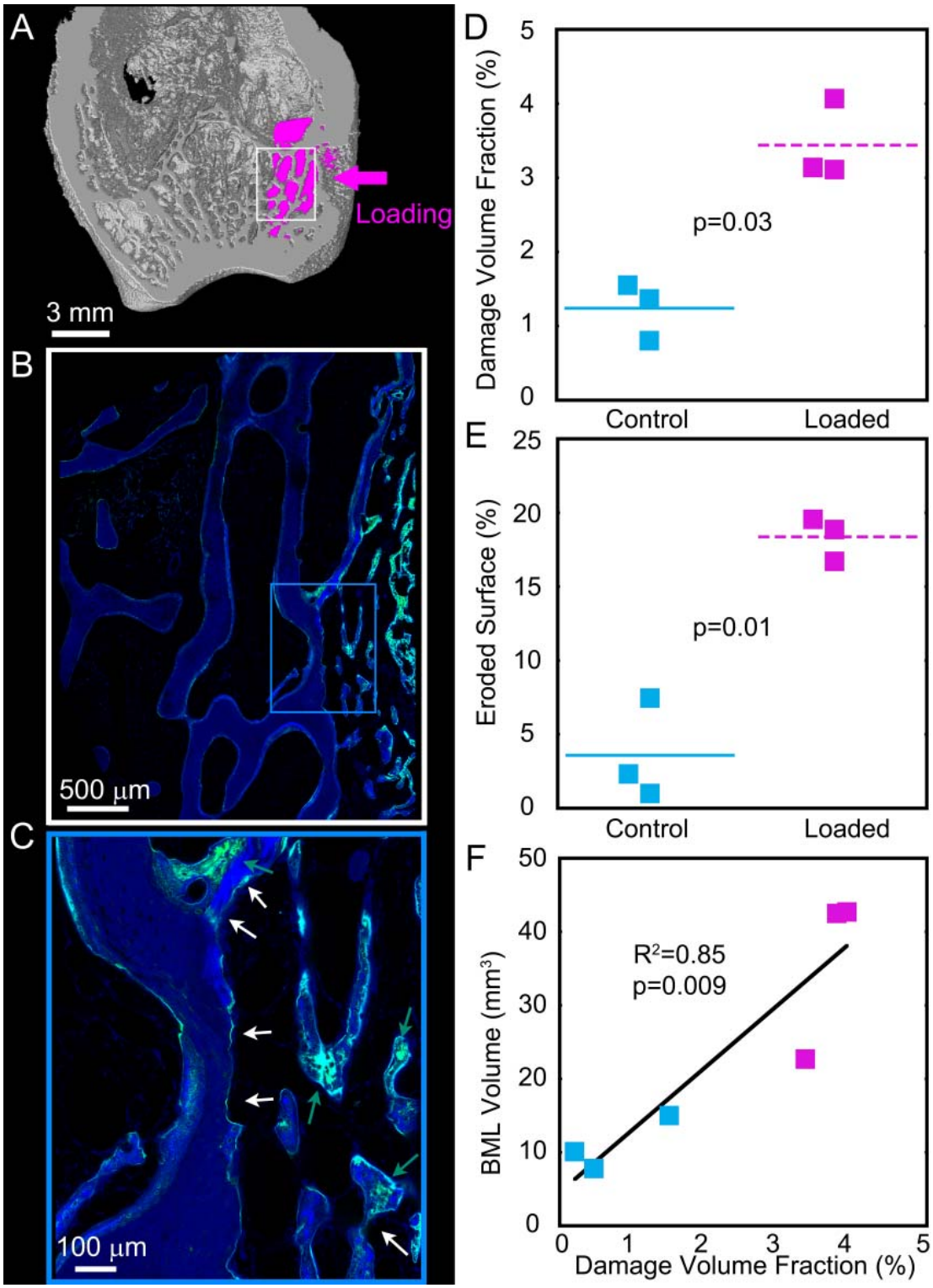

Figure 5.4. Bone tissue collected from BMLs had tissue microdamage and evidence of increased osteoclast activity when evaluated two weeks after surgery/loading (A) A

microCT image of a loaded limb with an overlay of the MR image of the BML 2 weeks after loading is shown. The white box indicates the location of the histology section shown in (B) with magnified section shown in (C). (C) Microdamage (stained with calcein, green arrows) and eroded surfaces (white arrows) were evident in the histology sections of the loaded limbs. Baseline levels of microdamage and remodeling were very low in the contralateral control limbs. (D-E) Eroded surface and damage volume fraction and eroded surface were greater in loaded limbs. (F) The direct assessment of damage volume fraction was correlated with indirect MRI assessment of BML volume at two weeks after loading.

5.5. Discussion

The goal of the current study was to establish a preclinical model of a BML utilizing indirect and direct imaging modalities to evaluate the development and progression of BMLs. We showed that *in vivo* cyclic mechanical loading of the cancellous bone in the lateral distal femur of the rabbit generated a BML visible at 1 and 2 weeks following loading. Regions of bone tissue within the bone marrow lesion contained tissue microdamage and increased bone resorption as detected by eroded surface. These features recapitulated the hallmarks of bone marrow lesions observed in clinical biopsies.

A limitation of the current study is the small sample size (n=3 paired limbs). Although the number of limbs examined was small, the differences between loaded and control limbs were large and consistent among all three animals, providing confidence in the repeatability of the model. We examined histology at a single time point; therefore, our results provide only rudimentary information regarding the longitudinal changes of the bone. Our data show that the current model is useful for examining load-induced BMLs, but our fatigue damage-based approach may result in a bone marrow lesion that differs from those associated with inflammation,

periarticular bone infarcts and transient idiopathic BMLs [24]. Little is known about the etiology of BMLs, the pathophysiology of a load-induced BML may not be representative of other types of BMLs. However, increased mechanical stress in the joint is implicated in most BMLs associated with osteoarthritis [8, 9], and our model recapitulates the histopathology of human BMLs including tissue damage [10] and bone remodeling [11, 12]. The current study concentrated on evaluating the pathogenesis of BMLs, but we anticipate that concomitant changes would occur at the adjacent articular surfaces that may also be evaluated using morphologic and quantitative MRI [25, 26]. Other approaches for studying BMLs in the context of cartilage degeneration are available in mice and rats [13]. Compared to rodent models, the rabbit model is advantageous for studying BMLs in bone because of larger regions of cancellous bone and fusion of the growth plates at a younger age [27], thereby providing an environment in epiphyseal cancellous bone that more closely mimics the conditions in human bone marrow lesions.

The presence of tissue microdamage and increased bone resorption in BMLs is consistent with prior work examining interactions between microdamage and remodeling. Tissue microdamage has long been considered a stimulus for bone resorption and remodeling. In cortical bone, the generation of tissue microdamage causes apoptosis of neighboring osteocytes leading to increased bone resorption and remodeling [28, 29]. In cancellous bone, the response to tissue microdamage is unknown and may also involve increased bone resorption. However, tissue damage in cancellous bone has also been associated with increased bone formation in the form of

a “microcallus” [30]. While the current study demonstrated increased bone resorption within the BML, as measured by eroded surface, the use of only a single time point for histology and the absence of bone formation markers prevent us from making conclusions regarding the bone remodeling response to tissue damage. A larger study with additional time points would be required to determine the temporal progression of load-induced microdamage in cancellous bone. A spatial and temporal relationship between microdamage and subsequent bone resorption/formation would indicate the importance of tissue microdamage as compared to other effects of loading (e.g. increased marrow pressure, etc.) in stimulating bone remodeling. Spatial and temporal associations between tissue damage and remodeling have been performed in cortical bone [29, 31], but demonstrating such a relationship in cancellous bone is more difficult because spatial correlations can occur out of the plane of a histology section, requiring the use of three-dimensional imaging of remodeling and microdamage [32].

The pre-clinical model described here has a number of strengths as a tool for studying BMLs. First, the model includes two characteristics that are observed in biopsies of established BMLs in humans: tissue microdamage and evidence of increased bone remodeling based on increased eroded surface. Second, BMLs in this animal model were created by applying loads directly to epiphyseal cancellous bone, allowing examination of the BMLs without direct damage to cartilage or ligaments. Lastly, as mentioned above, a strength of the model is the use of skeletally mature rabbits with closed growth plates to ensure that changes in cancellous bone

microarchitecture were due to the applied mechanical stimulus and not longitudinal growth [33].

Clinical evidence suggests that BMLs may be an early indicator of, or contributor to, articular cartilage degeneration. Recent studies have proposed clinical treatments for BMLs such as bisphosphonates [34], chondroitin sulphate [35] and subchondroplasty [36]. Because our understanding of the pathophysiology of BMLs is limited, the most effective treatment strategy is unclear, as is how best to evaluate the effectiveness of a given treatment. By representing the major components of a clinical BML, this *in vivo* rabbit model has the potential to provide important information on the natural history and efficacy of treatments on load-induced BML development and progression.

5.6. Acknowledgements
We thank Bhupinder Singh and the Cornell CARE facility for their assistance in animal care and housing and surgery. We thank Teresa Porri and the Cornell MRI facility for their assistance in microcomputed tomography and MR imaging. We also thank Hollis Potter for her advice on the project. One or more of the authors (CJH, MCH vdM) has received research funding from the National Institute of Arthritis and Musculoskeletal and Skin Diseases of the National Institute of Health under award AR57362 (CJH), AR007281 (MCH vdM). One or more of the authors (JBM) has received funding from the NSF Graduate Research Fellowship Program (GRFP). MCH vdM has stock ownership in Johnson & Johnson, Novartis, Proctor & Gamble. MPGB is a consultant for Smith and Nephew. Imaging data were acquired in the

Cornell Biotechnology Resource Center (BRC)-Imaging Facility using equipment purchased with NIH funding (1S10RR025502 and 1S10OD012287).

Each author certifies that his or her institution approved the animal protocol for this investigation and that all investigations were conducted in conformity with ethical principles of research

All research was performed at Cornell University, Ithaca, NY, USA.

5.7. Supplemental Materials

A series of pilot studies were performed on rabbit cadaver limbs to identify a cyclic loading regimen that would generate tissue microdamage in cancellous bone, thereby mimicking tissue microdamage observed in biopsies from patients. Generating tissue microdamage in bone is a balance between load amplitude and the number of applied cycles of loading [37]. Excessive load amplitude will cause overt failure of cancellous bone, but excessively small load amplitudes will only generate tissue microdamage following an excessive period of cyclic loading. To determine the appropriate balance between load magnitude, number of cycles and tissue microdamage, we performed pilot studies on rabbit femora dissected free of soft tissues. A compressive cyclic load ranging from 0.2 to 2.0 MPa (minimum to maximum) at 2 Hz frequency for 10,000 cycles was found to reliably generate tissue microdamage *in vitro* (Supplemental Figure 1). The duration of applied loading (83 minutes) was considered appropriate for anesthetic as viewed by veterinary experts.

To confirm that the selected loading regimen would reliably generate tissue microdamage when soft tissues were intact, the implant was implanted on rabbit limbs

(n=5 loaded femurs, n=2 control femurs). After applied loading, bones were dissected free of soft tissues. The lateral epiphysis of each femur was isolated using a low-speed precision saw (IsoMet Low Speed Saw, Buehler, Lake Bluff, Illinois USA). Microdamage was stained with a radiopaque marker (lead uranyl acetate) using a previously described protocol [38, 39]. Three-dimensional images of the specimens were collected using microcomputed tomography (Versa 520, Carl Zeiss AG, Oberkochen, Germany) in air with energy of 120 kVp and an isotropic voxel size of 10 μm. After imaging, a cylindrical volume of interest 3.7 mm in diameter and 3.7 mm high, located 500 microns away from the surface of the loading core was used for analysis. A three-dimensional Gaussian filter (sigma=1.2, support 1) was applied to the images, and an automated global threshold based on the image mean intensity value was used to segment bone from soft tissue (ImageJ 1.50d, National Institute of Health, USA). Microdamage stained with lead uranyl acetate was segmented from bone using a manual threshold; non-specific surface staining and damage objects less than 10,000 μm^3 were removed as noise (approximately the volume of 25 osteocyte lacunae, see [38] for further justification of image processing). The volume of tissue microdamage was measured per unit bone volume (damage volume fraction, DV/BV).

No signs of overt failure (macroscopic fractures or discontinuities in the loading displacement curve) were observed during cyclic loading (Supplemental Figure 2). Samples loaded *in situ* displayed substantial tissue microdamage, while control limbs had negligible amounts of stained microdamage (damage volume fraction: Loaded 5.7 ± 3.1% vs. Control 0.6 ± 0.8%, mean ± SD, $p = 0.01$, see

Supplementary Figure 3).

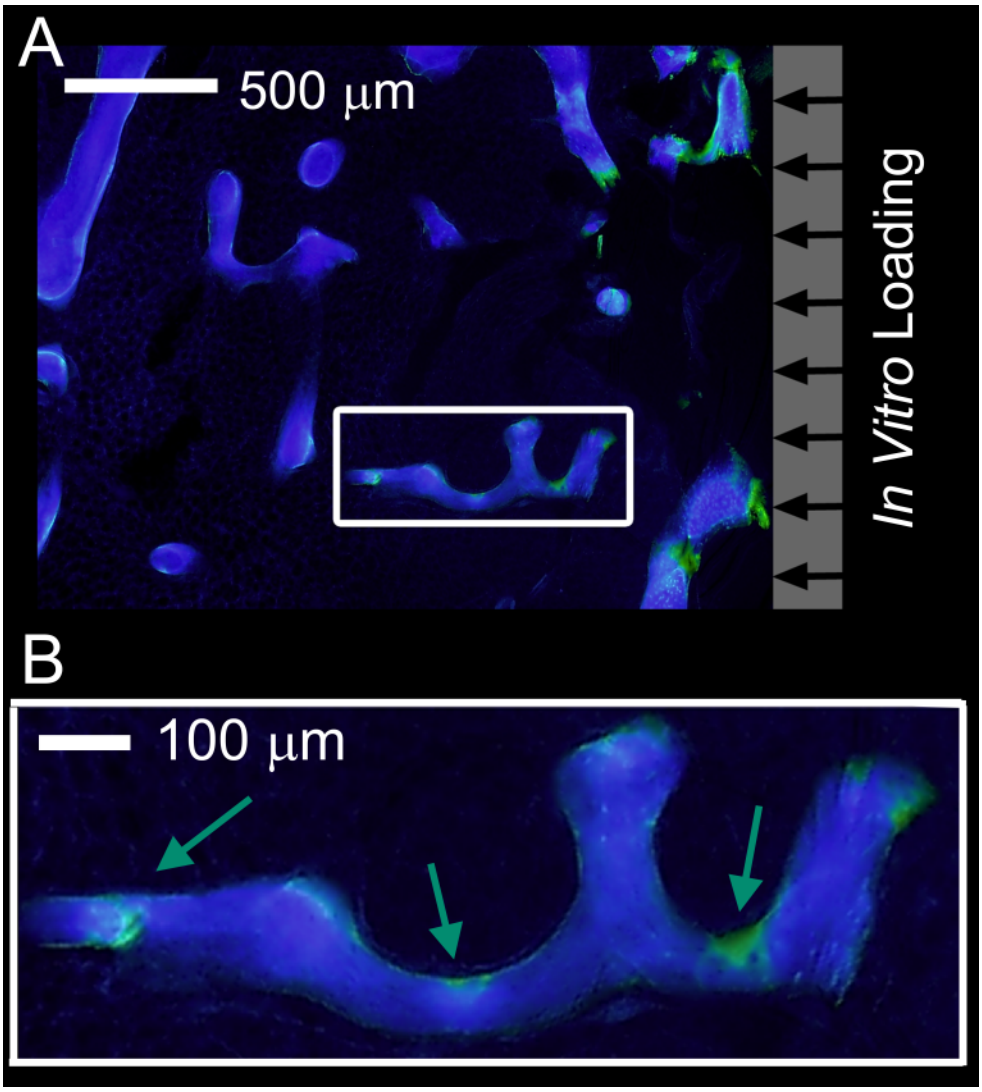

Figure 5.5. A cyclic loading regimen of 0.2-2.0 MPa in compression at 2 Hz frequency for 10,000 cycles generated tissue microdamage in cancellous bone without causing overt fracture. (A) Histological image of cancellous bone (bone=blue) in the rabbit distal femur stained for microdamage with calcein green and location of applied loading indicated. (B) An enlarged image of the boxed region displays the microdamage (stained with calcein green, indicated by green arrows).

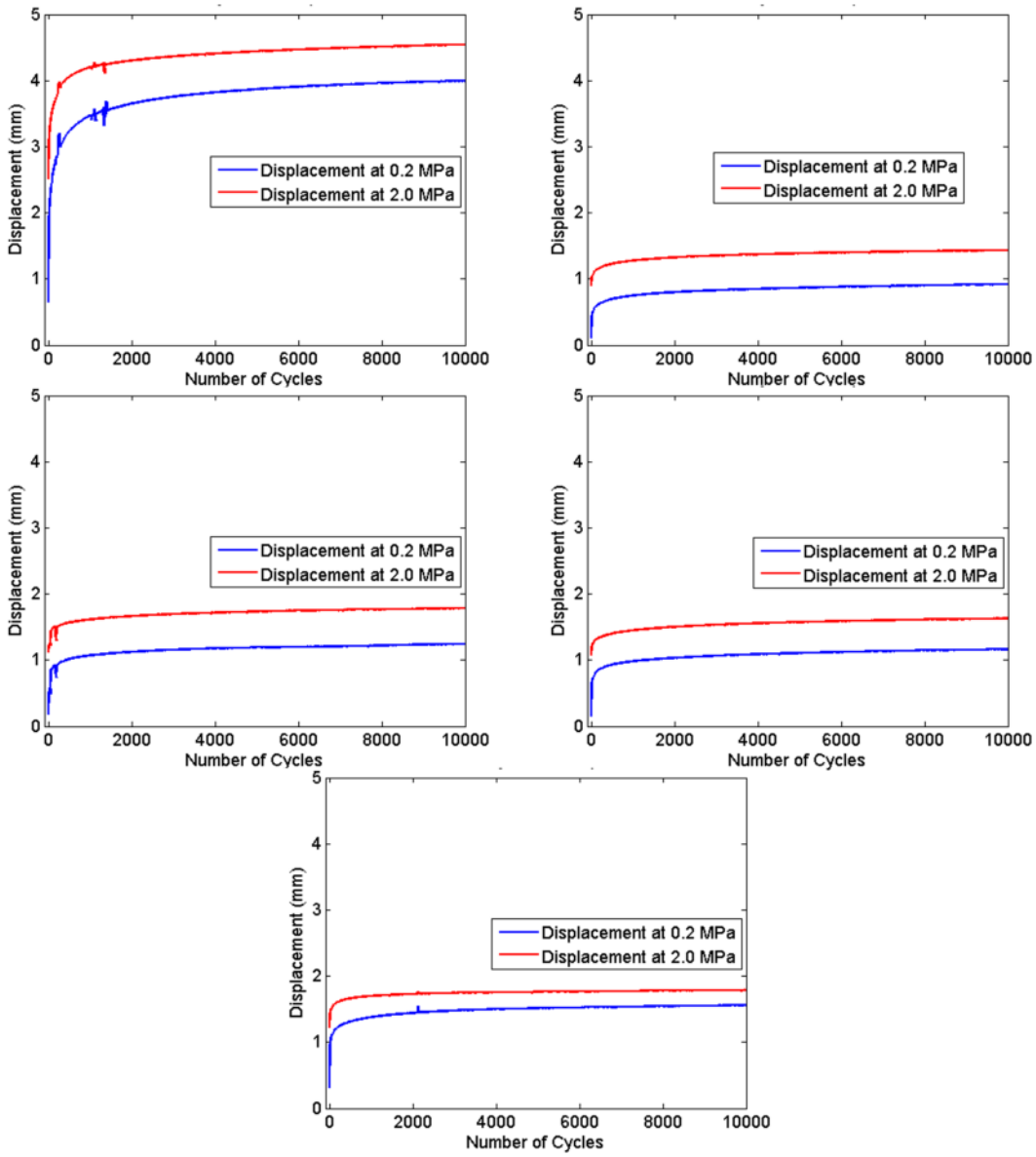

Figure 5.6. Peak-to-peak displacement during cyclic loading in for all five limbs loaded *in situ*. No signs of overt failure, indicated by a rapid increase in deformation, were observed.

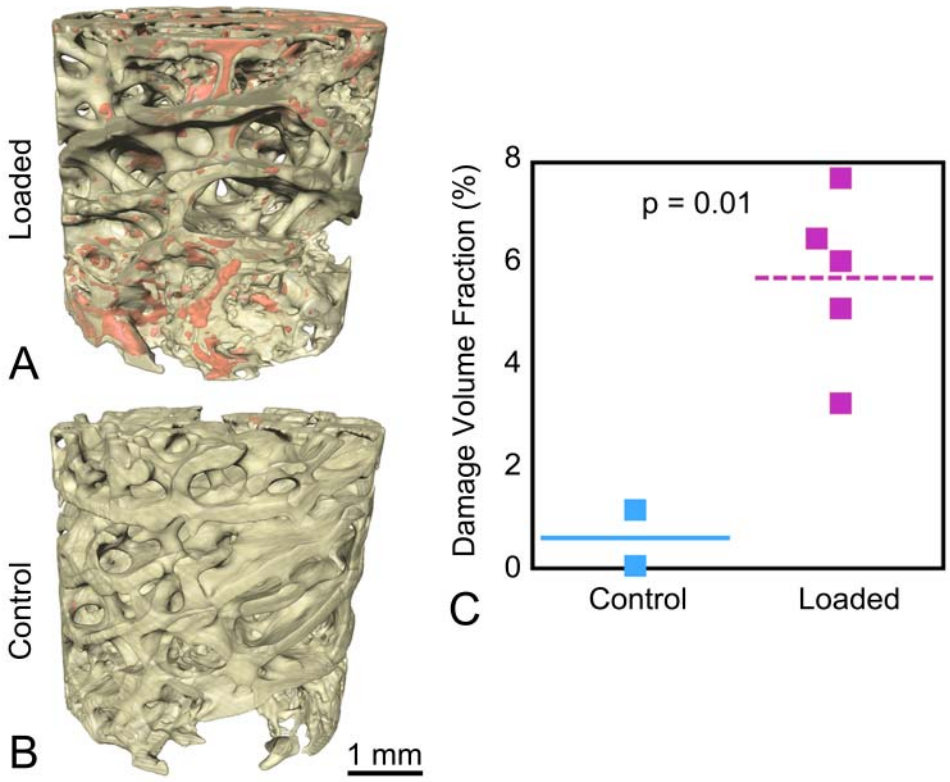

Figure 5.7. Three-dimensional reconstructions of cancellous bone and microdamage (pink) from *in situ* loading are shown for (A) a loaded limb and (B) control limb. (C) Loaded specimens (n=5) had a greater damage volume fraction than controls (n=2).

REFERENCES

[1] D.J. Hunter, W. Zhang, P.G. Conaghan, K. Hirko, L. Menashe, L. Li, W.M. Reichmann, E. Losina, Systematic review of the concurrent and predictive validity of MRI biomarkers in OA, Osteoarthritis Cartilage 19(5) (2011) 557-588.

[2] L. Xu, D. Hayashi, F.W. Roemer, D.T. Felson, A. Guermazi, Magnetic Resonance Imaging of Subchondral Bone Marrow Lesions in Association with Osteoarthritis, Semin. Arthritis Rheum. 42(2) (2012) 105-118.

[3] S.K. Tanamas, A.E. Wluka, J.P. Pelletier, J.M. Pelletier, F. Abram, P.A. Berry, Y.Y. Wang, G. Jones, F.M. Cicuttini, Bone marrow lesions in people with knee osteoarthritis predict progression of disease and joint replacement: a longitudinal study, Rheumatology 49(12) (2010) 2413-2419.

[4] L. Sharma, M. Nevitt, M. Hochberg, A. Guermazi, F.W. Roemer, M. Crema, C. Eaton, R. Jackson, K. Kwoh, J. Cauley, O. Almagor, J.S. Chmiel, Clinical significance of worsening versus stable preradiographic MRI lesions in a cohort study of persons at higher risk for knee osteoarthritis, Ann. Rheum. Dis. 75(9) (2016) 1630-6.

[5] F.J. Baranyay, Y. Wang, A.E. Wluka, D.R. English, G.G. Giles, R.O. Sullivan, F.M. Cicuttini, Association of bone marrow lesions with knee structures and risk factors for bone marrow lesions in the knees of clinically healthy, community-based adults, Semin Arthritis Rheum 37(2) (2007) 112-8.

[6] E. Guymer, F. Baranyay, A.E. Wluka, F. Hanna, R.J. Bell, S.R. Davis, Y. Wang, F.M. Cicuttini, A study of the prevalence and associations of subchondral bone

marrow lesions in the knees of healthy, middle-aged women, Osteoarthritis Cartilage 15(12) (2007) 1437-42.

[7] D.T. Felson, M.J. Parkes, E.J. Marjanovic, M. Callaghan, A. Gait, T. Cootes, M. Lunt, J. Oldham, C.E. Hutchinson, Bone marrow lesions in knee osteoarthritis change in 6-12 weeks, Osteoarthritis Cartilage 20(12) (2012) 1514-1518.

[8] D.T. Felson, S. McLaughlin, J. Goggins, M.P. LaValley, E. Gale, S. Totterman, W. Li, C. Hill, D. Gale, Bone marrow edema and its relation to progression of knee osteoarthritis, Ann. Intern. Med. 139(5) (2003) 330-336.

[9] K.L. Bennell, M.W. Creaby, T.V. Wrigley, K.A. Bowles, R.S. Hinman, F. Cicuttini, D.J. Hunter, Bone marrow lesions are related to dynamic knee loading in medial knee osteoarthritis, Ann. Rheum. Dis. 69(6) (2010) 1151-1154.

[10] M.S. Taljanovic, A.R. Graham, J.B. Benjamin, A.F. Gmitro, E.A. Krupinski, S.A. Schwartz, T.B. Hunter, D.L. Resnick, Bone marrow edema pattern in advanced hip osteoarthritis: quantitative assessment with magnetic resonance imaging and correlation with clinical examination, radiographic findings, and histopathology, Skeletal Radiol 37(5) (2008) 423-31.

[11] M. Zanetti, E. Bruder, J. Romero, J. Hodler, Bone marrow edema pattern in osteoarthritic knees: Correlation between MR imaging and histologic findings, Radiology 215(3) (2000) 835-840.

[12] M. Shabestari, J. Vik, J.E. Reseland, E.F. Eriksen, Bone marrow lesions in hip osteoarthritis are characterized by increased bone turnover and enhanced angiogenesis, Osteoarthritis Cartilage 24(10) (2016) 1745-52.

[13] G.H. Zhen, C.Y. Wen, X.F. Jia, Y. Li, J.L. Crane, S.C. Mears, F.B. Askin, F.J. Frassica, W.Z. Chang, J. Yao, J.A. Carrino, A. Cosgarea, D. Artemov, Q.M. Chen, Z.H. Zhao, X.D. Zhou, L. Riley, P. Sponseller, M. Wan, W.W. Lu, X. Cao, Inhibition of TGF-beta signaling in mesenchymal stem cells of subchondral bone attenuates osteoarthritis, Nat. Med. 19(6) (2013) 704-712.

[14] A.J. Ramme, M. Lendhey, J.G. Raya, T. Kirsch, O.D. Kennedy, A novel rat model for subchondral microdamage in acute knee injury: a potential mechanism in post-traumatic osteoarthritis., Osteoarthritis Cartilage 24(10) (2016) 1776-85.

[15] D.B. Burr, M.A. Gallant, Bone remodelling in osteoarthritis, Nat. Rev. Rheumatol. 8(11) (2012) 665-673.

[16] D.B. Burr, E.L. Radin, Microfractures and microcracks in subchondral bone: are they relevant to osteoarthrosis?, Rheum. Dis. Clin. North Am. 29(4) (2003) 675-685.

[17] M.C. van der Meulen, T.G. Morgan, X. Yang, T.H. Baldini, E.R. Myers, T.M. Wright, M.P. Bostrom, Cancellous bone adaptation to in vivo loading in a rabbit model, Bone 38(6) (2006) 871-7.

[18] M.C. van der Meulen, X. Yang, T.G. Morgan, M.P. Bostrom, The effects of loading on cancellous bone in the rabbit, Clinical Orthopaedics and Related Research 467(8) (2009) 2000-6.

[19] T.G. Morgan, M.P. Bostrom, M.C. van der Meulen, Tissue-level remodeling simulations of cancellous bone capture effects of in vivo loading in a rabbit model, J Biomech 48(5) (2015) 875-82.

[20] A. Fahlgren, X. Yang, C. Ciani, J.A. Ryan, N. Kelly, F.C. Ko, M.C. van der Meulen, M.P. Bostrom, The effects of PTH, loading and surgical insult on cancellous bone at the bone-implant interface in the rabbit, Bone 52(2) (2013) 718-24.

[21] M.J. Grosso, H.W. Courtland, X. Yang, J.P. Sutherland, K. Stoner, J. Nguyen, A. Fahlgren, F.P. Ross, M.C.H. van der Meulen, M.P. Bostrom, Intermittent PTH Administration and Mechanical Loading Are Anabolic for Periprosthetic Cancellous Bone, J. Orthop. Res. 33(2) (2015) 163-173.

[22] B.M. Willie, X. Yang, N.H. Kelly, J. Han, T. Nair, T.M. Wright, M.C. van der Meulen, M.P. Bostrom, Cancellous bone osseointegration is enhanced by in vivo loading, Tissue engineering. Part C, Methods 16(6) (2010) 1399-406.

[23] F.W. Roemer, A. Guermazi, M.K. Javaid, J.A. Lynch, J. Niu, Y. Zhang, D.T. Felson, C.E. Lewis, J. Torner, M.C. Nevitt, M.S. Investigators, Change in MRI-detected subchondral bone marrow lesions is associated with cartilage loss: the MOST Study. A longitudinal multicentre study of knee osteoarthritis, Ann. Rheum. Dis. 68(9) (2009) 1461-1465.

[24] F.W. Roemer, R. Frobell, D.J. Hunter, M.D. Crema, W. Fischer, K. Bohndorf, A. Guermazi, MRI-detected subchondral bone marrow signal alterations of the knee joint: terminology, imaging appearance, relevance and radiological differential diagnosis, Osteoarthritis Cartilage 17(9) (2009) 1115-1131.

[25] M.F. Koff, H.G. Potter, Noncontrast MR techniques and imaging of cartilage, Radiol Clin North Am 47(3) (2009) 495-504.

[26] H.G. Potter, J.M. Linklater, A.A. Allen, J.A. Hannafin, S.B. Haas, Magnetic resonance imaging of articular cartilage in the knee. An evaluation with use of fast-spin-echo imaging, J Bone Joint Surg Am 80(9) (1998) 1276-84.

[27] S.H. Kilborn, G. Trudel, H. Uhthoff, Review of growth plate closure compared with age at sexual maturity and lifespan in laboratory animals, Contemp Top Lab Anim Sci 41(5) (2002) 21-6.

[28] L. Cardoso, B.C. Herman, O. Verborgt, D. Laudier, R.J. Majeska, M.B. Schaffler, Osteocyte apoptosis controls activation of intracortical resorption in response to bone fatigue, J. Bone Miner. Res. 24(4) (2009) 597-605.

[29] O.D. Kennedy, B.C. Herman, D.M. Laudier, R.J. Majeska, H.B. Sun, M.B. Schaffler, Activation of resorption in fatigue-loaded bone involves both apoptosis and active pro-osteoclastogenic signaling by distinct osteocyte populations, Bone 50(5) (2012) 1115-22.

[30] M. Hahn, M. Vogel, M. Amling, H. Ritzel, G. Delling, Microcallus formations of the cancellous bone: a quantitative analysis of the human spine, J. Bone Miner. Res. 10(9) (1995) 1410-1416.

[31] M.B. Schaffler, O.D. Kennedy, Osteocyte signaling in bone, Curr Osteoporos Rep 10(2) (2012) 118-25.

[32] A.M. Torres, J.B. Matheny, T.M. Keaveny, D. Taylor, C.M. Rimnac, C.J. Hernandez, Material heterogeneity in cancellous bone promotes deformation recovery after mechanical failure, Proc. Natl. Acad. Sci. U S A 113(11) (2016) 2892-7.

[33] A.S. Turner, Animal models of osteoporosis--necessity and limitations, Eur. Cell Mater. 1 (2001) 66-81.

[34] L.L. Laslett, D.A. Dore, S.J. Quinn, P. Boon, E. Ryan, T.M. Winzenberg, G. Jones, Zoledronic acid reduces knee pain and bone marrow lesions over 1 year: a randomised controlled trial, Ann. Rheum. Dis. 71(8) (2012) 1322-1328.

[35] L.M. Wildi, J.P. Raynauld, J. Martel-Pelletier, A. Beaulieu, L. Bessette, F. Morin, F. Abram, M. Dorais, J.P. Pelletier, Chondroitin sulphate reduces both cartilage volume loss and bone marrow lesions in knee osteoarthritis patients starting as early as 6 months after initiation of therapy: a randomised, double-blind, placebo-controlled pilot study using MRI, Ann. Rheum. Dis. 70(6) (2011) 982-989.

[36] J. Farr, S.B. Cohen, Expanding Applications of the Subchondroplasty Procedure for the Treatment of Bone Marrow Lesions Observed on Magnetic Resonance Imaging, Oper. Tech. Sports Med. 21(2) (2013) 138-143.

[37] S.R. Kummari, A.J. Davis, L.A. Vega, N. Ahn, E.H. Cassinelli, C.J. Hernandez, Trabecular microfracture precedes cortical shell failure in the rat caudal vertebra under cyclic overloading, Calcif Tissue Int 85(2) (2009) 127-33.

[38] F.M. Lambers, A.R. Bouman, C.M. Rimnac, C.J. Hernandez, Microdamage caused by fatigue loading in human cancellous bone: relationship to reductions in bone biomechanical performance, PLoS One 8(12) (2013) e83662.

[39] S.Y. Tang, D. Vashishth, A non-invasive in vitro technique for the three-dimensional quantification of microdamage in trabecular bone, Bone 40(5) (2007) 1259-64.

CHAPTER 6
SUMMARY AND FUTURE DIRECTIONS

Bone loss following increased bone remodeling impairs the mechanical performance of cancellous bone and increases fracture risk. Cancellous bone strength is only partially explained by changes in bone mass, suggesting that factors independent of bone mass contribute to cancellous bone mechanical performance. The role that aspects of bone quality, including resorption cavity size, trabecular morphology and tissue composition, have on cancellous bone strength was unclear. Here, I investigated how bone quality was changed by altering bone remodeling through pharmaceutical treatment and how aspects of bone quality affected the accumulation of microdamage in cancellous bone. Finally, I investigated how bone remodeling responded to microdamage in a rabbit model for bone marrow lesions.

6.1. Aim 1 Summary

We investigated how treatment with anti-resorptive agents influenced the size of individual resorption cavities in a rodent model of estrogen depletion. We found that anti-resorptive treatment was associated with reduced resorption cavity size. The change in resorption cavity size was expected to reduce the stress concentration effect of cavities and was proposed as a potential mechanism through which treatment with anti-resorptive agents could reduce fracture risk greater than expected from changes in BMD.

6.2. Aim 2 Summary

We analyzed how treatment with sclerostin antibody modified the rod- or plate-like morphology and orientation of trabeculae in a cynomolgus monkey model. We found that sclerostin antibody treatment increased bone formation in a way that converted rod-like trabeculae into plate-like trabeculae. Sclerostin antibody also increased the thickness of both rods and plates regardless of trabecular orientation leading to an increase in apparent stiffness determined from finite element models. However, the improvements in the elastic mechanical performance were well explained by changes in bone volume.

6.3. Aim 3 Summary

We examined how resorption cavities and tissue composition (AGEs) influenced where microdamage formed and propagated following cyclic mechanical loading. We found that microdamage formed preferentially in the central regions of trabeculae, where the concentration of AGEs was greatest and away from resorption cavities on the more ductile trabecular surfaces. The preferential location of microdamage at trabecular centers may aid in deformation recovery following loading.

6.4. Aim 4 Summary

We evaluated the bone remodeling response to microdamage using an *in vivo* loading model that included the creation of BMLs in subchondral cancellous bone. We found an increase in bone resorption as measured by eroded surface in response to microdamage created by loading. The load-induced microdamage and subsequent increased bone resorption corresponded to regions where BMLs were created.

6.5 Thesis Synthesis

The overall goal of the work described here was to understand how changes in bone remodeling influenced cancellous bone strength in ways not attributable to bone mass. Anti-resorptive treatments for osteoporosis function primarily to decrease bone remodeling. Anti-resorptive agents decrease fracture risk beyond what could be attributed to changes in bone mass alone. We hypothesized that one major mechanism through which anti-resorptive treatments achieve a disproportionately large reduction in fracture risk was by reducing the size of resorption cavities. In Aim 1, we found that indeed anti-resorptive treatment did reduce the size of resorption cavities. Finite element models of cancellous bone with resorption cavities indicate that cavities act as stress risers in bone and that deeper cavities increase have an even greater stress concentration effect [1-4]. Consequently, resorption cavities ***should*** act as sites for microdamage initiation. In Aim 3, we directly tested the hypotheses that 1) resorption cavities would promote microdamage initiation and propagation following fatigue loading and 2) that deep resorption cavities would promote microdamage to a greater extent than small cavities. We found that in fact resorption cavities did not promote microdamage. Consequently, it is unlikely that resorption cavities play a significant role in influencing bone strength or fracture risk beyond what can be attributed to a loss in bone volume or through fenestration of trabeculae. Our results from Aim 3 indicate that cancellous bone tissue composition plays a greater role in determining where microdamage will form than resorption cavities. Microdamage formed preferentially in the central regions of the trabeculae, where the tissue was older and had accumulated a greater concentration of AGEs.

Bone resorption in response to microdamage may influence the progression of osteoarthritis. In Aim 4, we developed an *in vivo* loading model to create microdamage in subchondral cancellous bone. We found that increased bone resorption in response to microdamage accompanied the development of bone marrow lesions in subchondral cancellous bone. Our findings are consistent with a proposed pathway in which microdamage created by loading initiates an increase in bone resorption to repair damage. One potential molecular mechanism involves TGF-β. TGF-β in bone matrix is released by osteoclastic resorption [5] and subsequently influences the formation of nestin+ mesenchymal stem cell (MSC) clusters. These MSC clusters result in increased angiogenesis, aberrant bone formation, and bone marrow lesions prior to cartilage degeneration [6]. The direct role of bone marrow lesions in cartilage degeneration is unclear but may involve the disruption of bone and cartilage crosstalk by acting as a perfusion abnormality [7].

Next we investigated how the rod- and plate-like morphology and orientation of individual trabeculae may influence bone strength independent of bone mass. Anabolic treatments of osteoporosis could increase bone formation to such an extent that they could change the shape the individual trabeculae from rod to plates or even create new trabeculae. In Aim 2, we tested the hypotheses that sclerostin antibody could transition trabecular rods into trabecular plates and create new trabecular connections. While we did not observe any newly formed trabeculae, we did observe rods that transitioned into plates due to sclerostin antibody treatment. We also observed a thickening of the rods that did not transition to plates. The improvement in

trabecular morphology did improve the elastic mechanical properties of cancellous bone as predicted by finite element models; however, the improvements were almost entirely explained by changes in bone volume. While it does not appear that trabecular morphology or orientation influenced the pre-yield mechanical properties of cancellous bone independent of bone volume, the rod- and plate-like structure and orientation of trabeculae may be more influential in cancellous bone loaded in fatigue. Results from a recent study that included specimens from Aim 3 showed that the thickness of rod-like trabeculae influences how much microdamage forms in cancellous bone for a given strain. Additionally, morphology and orientation of trabeculae appear to influence when microdamage forms as a function of fatigue life with rod-like trabeculae aligned in the transverse direction failing preferentially in early fatigue and axially-aligned plate-like trabeculae failing primarily during late fatigue [8].

6.6. Future Directions

6.6.1. Three-dimensional spatial correlation between cancellous bone tissue composition and microdamage

In Aim 3, we found that microdamage formed preferentially in the central regions of trabeculae where the concentration of AGEs is greatest. It is unclear; however, which aspect of tissue composition, AGEs or local tissue degree of mineralization, were primarily responsible for microdamage formation. Both AGEs and local tissue degree of mineralization increase as tissue ages, and are found preferentially in the central regions of cancellous bone where bone turnover is less likely to occur. Understanding which aspects of bone tissue composition drive

microdamage formation are important in that it could help us understand the mechanism of bone failure and potentially develop therapeutic solutions that target specific aspects of bone tissue composition. Furthermore, it would provide further insight into how diseases that modify tissue composition like diabetes mellitus modify the biomechanical performance of bone.

I propose the following research study to more fully understand how local tissue degree of mineralization and AGEs influence where microdamage forms and propagates. Specimens of cancellous bone would be obtained from cadaver vertebrae and divided into one of two groups. One group would receive ribosylation to create a high concentration of AGEs homogenously distributed throughout the cancellous bone structure [9, 10], and the other group would serve as a control. First, all specimens would be evaluated with SrμCT to identify the bone mineral density distribution (BMDD) at each voxel. Cohort-1 of each group would be evaluated for AGEs using the fluorometric approach detailed in Aim 3 and registered to the three-dimensional BMDD images; Cohort-2 would receive cyclic mechanical loading until failure to create microdamage. Next, three-dimensional spatial correlation between microdamage created from fatigue loading and regions of high mineral content from the BMDD images would be examined for the two groups.

The proposed study would allow us to determine if microdamage forms preferentially in regions with the greatest BMDD or if AGEs matter more in directing microdamage formation. If ribosylation of cancellous bone changes the damage formation pattern such that damage does not form in the central regions of trabeculae

in the ribosylated group, it would indicate that AGEs, rather than BMDD preferentially determine where microdamage forms. Whereas, if damage still forms where BMDD is highest, it would indicate that local tissue degree of mineralization plays a stronger role in direct damage formation. An analysis testing the spatial correlation between resorption cavities and microdamage in the ribosylation group could also yield interesting results. If the lack of AGEs on trabecular surfaces were the reason why most microdamage did not form near resorption cavities, we would expect a stronger spatial correlation between cavities and microdamage if AGEs were distributed homogenously because resorption cavities are geometric stress risers.

6.6.2. Biomimetic open-cell foam with material heterogeneity

In Aim 3, we observed that material heterogeneity in cancellous bone directed microdamage toward trabecular regions that are least likely to experience large permanent deformation and away from regions that are most likely to experience large deformation or contain surface flaws. We speculated that the location of microdamage would allow the cancellous bone structure to recover more deformation than if trabeculae had accumulated damage at surfaces, and, indeed, cancellous bone has been shown can recover 61-94% of applied deformation [11-13] caused by loading beyond the ultimate strain. An open-cell foam with similar patterns of material heterogeneity may exhibit increased deformation recovery as well, enhancing the structure's mechanical function after overt failure.

I propose the following research project to test the idea that material heterogeneity in bone leads to improved deformation recovery. First, I would

implement additive manufacturing to create high-resolution structures with the microstructure of cancellous bone and heterogeneous material properties [14, 15]. For one group, the structures would be composed of harder, more brittle materials in the inner regions of each trabecula and more ductile regions on trabecular surfaces. A second group would receive the same two materials, except that the brittle material would be on the surfaces and the ductile material would be used in the central region. A third group would be printed with only one material. The microstructures of the specimens would be based on microCT images of specimens from Aim 3, and each specimen would be printed for all three groups. Material selection should be devised to maintain a similar mass for the same specimen in each group. Next, we would perform fatigue loading on the three groups in a similar fashion to Aim 3, with particular emphasis being placed on measurements of deformation recovery. Using the proposed three groups, we would be able to observe how changes in material heterogeneity in specimens with identical geometry would influence deformation recovery. An alternative strategy would be to create 3D printed bone structures from metal and use either surface annealing to increase surface ductility or surface hardening to decrease surface ductility.

6.6.3. In vivo rabbit loading to study bone marrow lesion progression and spatial correlation between microdamage, bone remodeling and bone marrow lesions

In Aim 4, we established an animal model for bone marrow lesions. Bone marrow lesions are associated with pain, cartilage degeneration and an increased risk of total joint replacement [16-18]. Understanding the mechanisms through which bone marrow lesions form and progress would aid in our understanding of early

osteoarthritis progression since bone marrow lesions are an early indicator of osteoarthritis. Identifying effective treatment options for established bone marrow lesions are clinically significant as well since bone marrow lesions may actually contribute to osteoarthritis progression, and an effective treatment for a bone marrow lesion may also limit or even reverse osteoarthritis progression.

I propose the following experiments that further test the idea that BML creation is stimulated by bone resorption in response to mechanically-induced microdamage and to evaluate potential treatment options for existing BMLs. For the first experiment, rabbits would be divided into four treatment groups two weeks prior to loading: TGF-β inhibitor treatment [6], bisphosphonate treatment, an anti-angiogenesis treatment, and control. *In vivo* loading would be applied to the right distal femur of all animals; as an additional control, contralateral limbs would receive implants but no loading. One cohort of animals from each group would be sacrificed bi-weekly to characterize bone remodeling and how much microdamage exists at a given time point. Animals would also be evaluated with MRI at bi-weekly intervals to identify and measure bone marrow lesions and changes to articular surfaces.

The rationale behind the treatment groups is as follows: TGF-β has been identified as a key mechanistic factor from which microdamage leads to cartilage degeneration. TGF-β is released by bone resorption leading to the recruitment of mesenchymal stem cell clusters, subsequent increases in bone formation, BMLs and eventually cartilage degeneration. A TGF-β inhibitor is not expected to impair microdamage repair (and may actually increase resorption) but should decrease the

bone formation/MSC recruitment response that accompanies damage repair, thereby inhibiting BML formation. Anti-resorptive treatment should inhibit resorption stimulated by microdamage, either preventing or limiting the pathway that leads to BML formation. Furthermore, anti-resorptive treatment decreases resorption cavity size and may indirectly inhibit release of TGF-β by reducing the volume of bone resorbed at each remodeling site. Increases in angiogenesis have been observed in biopsies of BMLs, suggesting that an angiogenesis inhibitor may inhibit BML formation. Using MR imaging, we can obverse how the three approaches may prevent (or exacerbate) BML formation, modify the bone remodeling response to microdamage, and lead to differences in cartilage damage.

Next we would perform a new set of experiments on animals with established bone marrow lesions. The right limbs of all animals would receive *in vivo* loading to create BMLs. Upon confirmation of a BML two weeks following loading, animals would be assigned into one of four groups, a bisphosphonate treatment to inhibit bone remodeling, an angiogenesis inhibitor to inhibit vascularity, chondroitin sulphate, a proposed therapeutic for bone marrow lesions [19], and a final group that would receive a subchondroplasty the area of a bone marrow lesion [20]. Subchondroplasty is a new surgical technique to decrease bone marrow lesion size. Bone marrow lesion size and changes to articular cartilage would be evaluated bi-weekly following treatment using MRI. Tissue from the bone marrow lesion would then be evaluated for bone remodeling, microdamage, and mechanical performance using mechanical testing to observe how proposed treatment options affect the cancellous bone.

REFERENCES

[1] C.J. Hernandez, A. Gupta, T.M. Keaveny, A biomechanical analysis of the effects of resorption cavities on cancellous bone strength, J Bone Miner Res 21(8) (2006) 1248-55.

[2] S.K. Easley, M.T. Chang, D. Shindich, C.J. Hernandez, T.M. Keaveny, Biomechanical effects of simulated resorption cavities in trabecular bone across a wide range of bone volume fraction, J Bone Miner Res Submitted (2012).

[3] L.M. McNamara, J.C. van der Linden, H. Weinans, P.J. Prendergast, Stress-concentrating effect of resorption lacunae in trabecular bone, J Biomech 39(4) (2006) 734-41.

[4] M.G. Goff, C.R. Slyfield, S.R. Kummari, E.V. Tkachenko, S.E. Fischer, Y.H. Yi, M.G. Jekir, T.M. Keaveny, C.J. Hernandez, Three-dimensional characterization of resorption cavity size and location in human vertebral trabecular bone, Bone 51(1) (2012) 28-37.

[5] Y. Tang, X. Wu, W. Lei, L. Pang, C. Wan, Z. Shi, L. Zhao, T.R. Nagy, X. Peng, J. Hu, X. Feng, W. Van Hul, M. Wan, X. Cao, TGF-beta1-induced migration of bone mesenchymal stem cells couples bone resorption with formation, Nat Med 15(7) (2009) 757-65.

[6] G.H. Zhen, C.Y. Wen, X.F. Jia, Y. Li, J.L. Crane, S.C. Mears, F.B. Askin, F.J. Frassica, W.Z. Chang, J. Yao, J.A. Carrino, A. Cosgarea, D. Artemov, Q.M. Chen, Z.H. Zhao, X.D. Zhou, L. Riley, P. Sponseller, M. Wan, W.W. Lu, X. Cao, Inhibition

of TGF-beta signaling in mesenchymal stem cells of subchondral bone attenuates osteoarthritis, Nat. Med. 19(6) (2013) 704-712.

[7] D.M. Findlay, J.S. Kuliwaba, Bone-cartilage crosstalk: a conversation for understanding osteoarthritis, Bone Res 4 (2016) 16028.

[8] A.M. Torres, J.B. Matheny, M. Luna, F.M. Lambers, C.M. Rimnac, C.J. Hernandez, Trabecular Morphology has Differential Effects in Uniaxial and Fatigue Failure of Cancellous Bone, 23rd Congress of the European Society of Biomechanics, Seville, Spain, 2017.

[9] D. Vashishth, G.J. Gibson, J.I. Khoury, M.B. Schaffler, J. Kimura, D.P. Fyhrie, Influence of nonenzymatic glycation on biomechanical properties of cortical bone, Bone 28(2) (2001) 195-201.

[10] S.Y. Tang, D. Vashishth, Non-enzymatic glycation alters microdamage formation in human cancellous bone, Bone 46(1) (2010) 148-54.

[11] D.P. Fyhrie, M.B. Schaffler, Failure mechanisms in human vertebral cancellous bone, Bone 15(1) (1994) 105-9.

[12] T.M. Keaveny, E.F. Wachtel, D.L. Kopperdahl, Mechanical behavior of human trabecular bone after overloading, J Orthop Res 17 (1999) 346-53.

[13] C.J. Hernandez, F.M. Lambers, J. Widjaja, C. Chapa, C.M. Rimnac, Quantitative relationships between microdamage and cancellous bone strength and stiffness, Bone 66 (2014) 205-13.

[14] M. Mott, J.R.G. Evans, Zirconia/alumina functionally graded material made by ceramic ink jet printing, Mater. Sci. Eng. A-Struct. Mater. Prop. Microstruct. Process. 271(1-2) (1999) 344-352.

[15] A. Nadernezhad, N. Khani, G.A. Skvortsov, B. Toprakhisar, E. Bakirci, Y. Menceloglu, S. Unal, B. Koc, Multifunctional 3D printing of heterogeneous hydrogel structures, Sci Rep 6 (2016).

[16] D.J. Hunter, W. Zhang, P.G. Conaghan, K. Hirko, L. Menashe, L. Li, W.M. Reichmann, E. Losina, Systematic review of the concurrent and predictive validity of MRI biomarkers in OA, Osteoarthritis Cartilage 19(5) (2011) 557-588.

[17] L. Xu, D. Hayashi, F.W. Roemer, D.T. Felson, A. Guermazi, Magnetic Resonance Imaging of Subchondral Bone Marrow Lesions in Association with Osteoarthritis, Semin. Arthritis Rheum. 42(2) (2012) 105-118.

[18] S.K. Tanamas, A.E. Wluka, J.P. Pelletier, J.M. Pelletier, F. Abram, P.A. Berry, Y.Y. Wang, G. Jones, F.M. Cicuttini, Bone marrow lesions in people with knee osteoarthritis predict progression of disease and joint replacement: a longitudinal study, Rheumatology 49(12) (2010) 2413-2419.

[19] L.M. Wildi, J.P. Raynauld, J. Martel-Pelletier, A. Beaulieu, L. Bessette, F. Morin, F. Abram, M. Dorais, J.P. Pelletier, Chondroitin sulphate reduces both cartilage volume loss and bone marrow lesions in knee osteoarthritis patients starting as early as 6 months after initiation of therapy: a randomised, double-blind, placebo-controlled pilot study using MRI, Ann. Rheum. Dis. 70(6) (2011) 982-989.

[20] J. Farr, S.B. Cohen, Expanding Applications of the Subchondroplasty Procedure for the Treatment of Bone Marrow Lesions Observed on Magnetic Resonance Imaging, Oper. Tech. Sports Med. 21(2) (2013) 138-143.

APPENDIX

Aim2 Creation of FE model with boundary conditions to run in Abaqus

Purpose: The following protocol is used to create and run Abaqus input files based on stack of images of bone (tiff format). Following creation of a basic mesh using tiff_stack_to_aba_inp.m, the user can create boundary conditions on the top and bottom surfaces using a bash script.

1. Create binary tiff stack of images of cancellous bone. Use connective component analysis to ensure that all cancellous bone is connected.
2. Create an input file (inp.) from the tiff stack using Run tiff_stack_to_aba_inp.m in MATLAB
    a. Select MicroCT Images Folder.....what folder contains the image stack
    b. Select folder to store inp.....what folder do you want to store the input file
    c. What would you like to name this abaqus input file?..... input file name
    d. What is the voxel size for this image in mm for this tiff stack?.....input voxel size in mm
    e. What is the threshold value for this tiff stack?... for binary pick anything greater than 0 and less than 255
3. Open Cygwin Terminal and change working directly (cd) to folder with input files (Example below)

Jonathan Matheny@BIOMECH-11 ~

$ cd /cygdrive/k/tiffstack/Input_Files/

(drive K and subfolders tiffstack→Input_Files)

4. Create new folder to store complete input files (Input _full is example below) and change directory to it
    a. Store mkinp.awk in this newly created folder
5. Type the following command line in Cygwin to run mkinp.awk. Mkinp will create boundary conditions, material properties, etc. for the model

Jonathan Matheny@BIOMECH-11 /cygdrive/k/tiffstack/Input_Files/Input_full
$ for file in ../*inp; do echo $file; ./mkinp.awk $file; done
The script will run on any input file in the folder, and the output input file(s) will have the attachment text "_full".

6. Move full input files to complete input file folder (Input_full)

Jonathan Matheny@BIOMECH-11 /cygdrive/k/tiffstack/newtest/Input_full
$ mv ../*full.inp .

7. Run Abaqus to create FE models for the input files by inputing the following lines of text, one line at a time

Jonathan Matheny@BIOMECH-11 /cygdrive/k/tiffstack/newtest/Input_full
$ for file in *.inp;do
> echo $file
> done
> /cygdrive/c/SIMULIA/Abaqus/Commands/abaqus.bat interactive cpus=3 job=$file
Abaqus will run any input file in this folder.

If you need to kill the operation, do so using task manager, finding the specific process Abaqus is using and ending it.

Mkinp.awk will apply boundary conditions (fixed bottom boundary and compression to top boundary in the z-dimension.

```
#!/bin/awk -f


# (for pre-generated aba input files, "," is the field separator)

BEGIN {FS=",";mode="none"; maxz=-1e10; minz=1e10

  # find max and min z since there's round off differences

  # the current input file
  finp= ARGV[ARGC-1]

  # output file
  fout = substr(finp,1,length(finp)-4)"_full.inp"

  # loop through it checking z values
  while (getline < finp > 0) {
    if ($0 ~ /\*/) {mode="none"}

    if (mode=="node") {
      if ($4 > maxz) {
        maxz=$4
      }
      if ($4 < minz) {
        minz=$4
      }
    }

    if ($0 ~ /NODE/) {mode="node"}
  }
}


# let us know we don't have nodes to process
/\*/ {mode="none"}

{

if (mode=="node") {
  # check if they are in the max or min sets
  if ($4 == maxz) maxn[$1]=$1
  if ($4 == minz) minn[$1]=$1

  # we want to echo the input file
```

```
  print >fout
}
# not a node to process
else {
  # we want to echo the input file
  print >fout
}

}

# tell us that the next lines are nodes to process
/NODE/ {mode="node"}


END {

  print "**" >fout
  print "*NSET, NSET=top" >fout
  n = 0
  # write out all the nodes in the top group, eight to a line
  for (i in maxn) {
    n++
    if (n < 9) {
      printf ("%9d,",i) >fout
    }
    else {
      printf ("\n%9d,",i) >fout
      n=1
    }
  }
  printf "\n" >fout

  print "*NSET, NSET=bottom" >fout
  n = 0
  # write out all the nodes in the bottom group, eight to a line
  for (i in minn) {
    n++
    if (n < 9) {
      printf ("%9d,",i) >fout
    }
    else {
      printf ("\n%9d,",i) >fout
      n=1
    }
```

```
  }
  printf "\n" >fout
  print "**" >fout

  # now write out props and link to the elements
  # it is assumed that the elements are defined w/ ELSET=PROP1
  print "*MATERIAL,NAME=MATPROP1" >fout
  print "*ELASTIC,TYPE=ISO" >fout
  print "10000,0.3" >fout
  print "**" >fout

  # link the prop to the element set
  print "*SOLID SECTION,ELSET=PROP1,MATERIAL=MATPROP1" >fout
  print "**" >fout

  # Hmmm, don't need to fix rigid motion??

  # set the bottom as a global boundary condition (=0 disp)
  print "*BOUNDARY" >fout
  print "bottom,   3,,        0." >fout
  print "**" >fout

  # write out the step control
  print "*STEP, PERTURBATION" >fout
  print "*STATIC" >fout
  print "**" >fout

  # imposed displacement of -0.02 (1% of core height)
  print "*BOUNDARY" >fout
  print "top, 3,,     -0.02" >fout
  print "**" >fout

  # by specifying nothing, you should get default output in .odb

  # ask for reaction forces in the .dat file
  print "*NODE PRINT, NSET=bottom, FREQ=1" >fout
  print "RF" >fout
  print "**" >fout

  # and we're done
  print "*END STEP" >fout
}
```

Mkinpx.awk will apply boundary conditions (fixed bottom boundary and compression to top boundary in the x-dimension. The material properties and amount of displacements are highlighted in yellow.

```
#!/bin/awk -f


# (for pregenerated aba input files, "," is the field separator)

BEGIN {FS=",";mode="none"; maxz=-1e10; minz=1e10

  # find max and min z since there's roundoff differences

  # the current input file
  finp= ARGV[ARGC-1]

  # output file
  fout = substr(finp,1,length(finp)-4)"_full.inp"

  # loop through it checking z values
  while (getline < finp > 0) {
    if ($0 ~ /\*/) {mode="none"}

    if (mode=="node") {
      if ($4 > maxz) {
        maxz=$4
      }
      if ($4 < minz) {
        minz=$4
      }
    }

    if ($0 ~ /NODE/) {mode="node"}
  }
}


# let us know we don't have nodes to process
/\*/ {mode="none"}

{

if (mode=="node") {
```

```
  # check if they are in the max or min sets
  if ($4 == maxz) maxn[$1]=$1
  if ($4 == minz) minn[$1]=$1

  # we want to echo the input file
  print >fout
}
# not a node to process
else {
  # we want to echo the input file
  print >fout
}

}

# tell us that the next lines are nodes to process
/NODE/ {mode="node"}


END {

  print "**" >fout
  print "*NSET, NSET=top" >fout
  n = 0
  # write out all the nodes in the top group, eight to a line
  for (i in maxn) {
    n++
    if (n < 9) {
      printf ("%9d,",i) >fout
    }
    else {
      printf ("\n%9d,",i) >fout
      n=1
    }
  }
  printf "\n" >fout

  print "*NSET, NSET=bottom" >fout
  n = 0
  # write out all the nodes in the bottom group, eight to a line
  for (i in minn) {
    n++
    if (n < 9) {
      printf ("%9d,",i) >fout
```

```
   }
   else {
      printf ("\n%9d,",i) >fout
      n=1
   }
}
printf "\n" >fout
print "**" >fout

# now write out props and link to the elements
# it is assumed that the elements are defined w/ ELSET=PROP1
print "*MATERIAL,NAME=MATPROP1" >fout
print "*ELASTIC,TYPE=ISO" >fout
print "10000,0.3" >fout
print "**" >fout

# link the prop to the element set
print "*SOLID SECTION,ELSET=PROP1,MATERIAL=MATPROP1" >fout
print "**" >fout

# Hmmm, don't need to fix rigid motion??

# set the bottom as a global boundary condition (=0 disp)
print "*BOUNDARY" >fout
print "bottom,   3,,        0." >fout
print "**" >fout

# write out the step control
print "*STEP, PERTURBATION" >fout
print "*STATIC" >fout
print "**" >fout

# imposed displacement of -0.02 (1% of core height)
print "*BOUNDARY" >fout
print "top, 3,,     -0.02" >fout
print "**" >fout

# by specifying nothing, you should get default output in .odb

# ask for reaction forces in the .dat file
print "*NODE PRINT, NSET=bottom, FREQ=1" >fout
print "RF" >fout
print "**" >fout
```

```
  # and we're done
  print "*END STEP" >fout

}
```

Aim 3: Operating the MTS Material Testing Machine – Cyclic Loading

This protocol describes how to operate the MTS machine located in Upson 148 to test endcapped cancellous bone cores. The test consists of 10 preconditioning cycles to 0.2% compressive strain followed by two bouts of cyclic compressive loading.

1. Remove endcapped specimen from refrigerator and allow to thaw for a minimum of 30 minutes before testing (Perform steps 2-11 while specimen thaws)
2. Login to MTS computer. (Station Manager should be opened the day before testing with configuration file Floor.cfg, parameter set 100 lbf. Load cell Aim 4)
3. Attach upper and lower fastening chucks to MTS mechanical testing rig
4. Connect Hernandez extensometer (Number:51-191-508) to MTS testing machine On screen Signal Auto Offset, select Clear Offsets
5. Calibrate external load cell using signal conditioner.
6. On screen Station Manager:
    a. Check Exclusive Control
    b. Reset Interlock 1
    c. Turn on hydraulics in software
        i. Hit top button, wait until solid green

ii. Hit lower yellow button (two bars) followed by lower green button (three bars)

7. Turn on physical hydraulics by flipping switch to low (counterclockwise) and then to high (clockwise)
8. On screen Signal Auto Offset, select Clear Offsets
9. On screen Manual Command, select enable manual command and set displacement to 0.000 mm, deselect enable manual command
10. On screen Station Manager, run function generator for 30 minutes (0.1 Hz, 40 mm amplitude) then stop
11. Raise piston head up so that endcapped specimen can be placed in MTS testing machine (See step 9 for displacement of piston head)
12. After thawing, use the following procedure to attach a hydraulically sealed chamber to specimen and attach specimen to MTS testing machine
    a. Cut off pinky finger from small sized nitrile glove and cut off twice the length of the exposed specimen from the finger-tip region of the glove (allows for the glove piece to slip over the specimen)
    b. Before the specimen is fastened to the protective block, slide glove piece onto endcap that will be fastened to bottom chuck, place O-rings on both end-caps with minimal force on specimen
    c. Fasten specimen to protective block
    d. Clamp bottom endcap to bottom chuck

e. Using adjustable plate attached to bottom chuck, align bottom chuck with top chuck, tighten adjustable plate screws
f. On screen Signal Auto Offset, select Auto Offset
g. Tighten upper chuck to upper endcap
h. Remove protective block from specimen
i. Record Preload value in terms of volts and convert to force units (in N) using the equation Force=43.164 *V -0.2373
j. If the specimen appears to be misaligned (as signified by a high preload value of over 20 N), repeat sub steps d-h
k. Pull up glove so that the glove span over both end-caps, move the O-ring attached to bottom endcap near the upper edge of the endcap
l. Use syringe to add 1 mL of PBS solution to the specimen encased inside the glove
m. Move O-ring on upper endcap over the glove and move to lower edge of the endcap
n. With a scalpel, remove glove parts to the outside of the two O-rings and dry with Chem-Wipes (this is to ensure the hydration chamber fits within in the extensometer)

13. Attach extensometer to specimen and remove pin from extensometer (watch strain reading to ensure the value does not drift too much)
14. On screen Signal Auto Offset, auto offset value for axial strain

15. Open Multipurpose elite software, select file→Open Test and select AIM4_Preconditioning_100lbf
16. Click “New Test Run”→Click “Add New”→Enter specimen name and press “OK” twice→Enter pre-measured values for specimen length, diameter, and exposed length.
17. Double check to make sure extensometer pin is removed, MTS is in displacement mode, and alignment plate is tightened.
18. Press Run, preconditioning test should complete in approximately 5 seconds. Record effective length, area, and initial modulus from variable summary page, save test
19. Using the excel sheet Emod.xlsx, calculate the initial modulus that will be used for the subsequent bouts of cyclic loading (should be close in value to the modulus calculated by MTS)
20. In the Multipurpose elite software, select file→Open Test and select AIM4_Fatigue_Part 1_100lbf
21. Click “New Test Run”→Click “Add New”→Enter specimen name and press “OK” twice→Enter pre-measured values for specimen length, diameter, and exposed length and initial modulus calculated from Emod.xlsx.
22. Double check to make sure extensometer pin is removed, MTS is in displacement mode, and alignment plate is tightened.
23. Press Run, place hand near emergency stop. Test will need to be manually stopped by the user once the value for stainrate10 exceeds +15 or appears to be

entering into the tertiary phase. The test will automatically stop if the value for strain exceeds 2%.

24. Once the test has stopped, take a screen shot of the runtime display and save in a PowerPoint file. Save test run.
25. Make sure MTS is in displacement mode.
26. Fasten protective block to specimen, remove from MTS testing machine, and submerge specimen in 0.5 mM solution of xyenol orange staining for 2 hours→ store in refrigerator
27. After staining, perform three rinses (10 minutes each) in deionized water
28. Repeat Steps 11-14 to attach a hydraulically sealed chamber to the specimen, attach the specimen to MTS mechanical testing rig, and attach extensometer to the specimen
29. In the Multipurpose elite software, select file→Open Test and select AIM4_Preconditioning_100lb_part 2(This preconditioning only runs for 3 cycles). Click save
30. In the Multipurpose elite software, select file →Open Test and select AIM4_Fatigue_Part 2_100lbf
31. Click “New Test Run”→Click “Add New”→Enter specimen name and press “OK” twice→Enter pre-measured values for specimen length, diameter, and exposed length and initial modulus calculated from Emod.xlsx.
32. Double check to make sure extensometer pin is removed, MTS is in displacement mode, and alignment plate is tightened.

33. Press Run, place hand near emergency stop. Test will stop automatically once the value for stain exceeds 4%.
34. Once the test has stopped, take a screen shot of the runtime display and save in a powerpoint file. Save test run.
35. Make sure MTS is in displacement mode.
36. Fasten protective block to specimen, remove from MTS testing machine, and submerge specimen in 0.5 mM solution of Calcein staining for 2 hours→ store in refrigerator
37. After staining, perform three rinses (10 minutes each) in deionized water
38. Using the Isomet 1000 saw, remove the exposed portion of the specimen, store specimen in 70% EtOH, and submerge end-caps in acetone for at least 24 hours.
39. Close out of Multipurpose elite software
40. Lower piston head to lowest position
41. Turn off the hydraulics in the software
42. Turn off the real hydraulics by switching to low and then pressing the red button
43. Exit station manager (use file→ Exit, not the X button
44. Log off computer
45. Sanitize area and surfaces with 10% bleach for 10 minutes, wash with water and dry

Aim 3: Derivation for Calculating Tissue Modulus for Aim 3 Specimens using Finite Element Models and Apparent Modulus from Mechanical Testing

$d = 0.09\ mm$ →Displacement applied to top face of each sample in Finite Element Model in negative z-direction

$h = 13.85mm$ → Height of each sample in Finite Element Model

$\varepsilon_{A-FE} = \frac{d}{h} = 0.0064$ → Apparent applied strain to each sample in Finite Element Model. Since both h and d are constant among each sample, $\varepsilon_{A\text{-}FE}$ is constant among samples

E_{A-Exp} → Experimentally measured Apparent Young's Modulus found using a preconditioning loading cycle. The value is different for each sample

$\varepsilon_{A-Exp} = \frac{\sigma_{Exp}}{E_{A-Exp}} = 0.0039$→Experimental Apparent applied strain to each sample.

σ_{Exp} chosen such that $\varepsilon_{A\text{-}Exp}$ is constant among samples

σ_{Exp} → Apparent Stress applied to each sample.

σ_{Exp} is selected to satisfy the equation $\sigma_{Exp}=\varepsilon_{A\text{-}Exp} * E_{A\text{-}Exp}$

Since both the apparent strain applied experimentally ($\varepsilon_{A\text{-}Exp}$)and apparent strain applied in the Finite Element Model ($\varepsilon_{A\text{-}FE}$) are constant among samples, the strain distributions among samples are comparable The Finite Element Model chosen is appropriate to approximate the local strain distributions created experimentally by loading.

While the Tissue Modulus was assumed to be homogeneous and held constant at 10 Gpa in the Finite Element Models, the actual average tissue modulus of the bone was not known. The following derivation will allow the determination of average tissue modulus.

$E_{Tissue-FE} = 10\ GPa$ →Tissue Modulus chosen for each sample of the finite element model, the same value for tissue modulus was chosen for each sample

$A_{FE} = 5.027 \times 10^{-5} m^2$ →Cross-sectional area for each sample given that each sample had a radius of 4 mm, found using the equation $A=\pi*r^2$.

F_{FE} → Total Reaction Force was determined from the finite element model for each sample (in N). The value is different for each sample.

$\sigma_{FE} = \frac{F_{FE}}{A_{FE}}$ →Apparent Stress was applied to each sample in the finite element model (in Pa). The value is different for each sample.

$E_{A-FE} = \frac{\sigma_{FE}}{\varepsilon_{A-FE}}$ → Apparent Young's Modulus was derived for each sample for the finite element model (in Pa). The value is different for each sample.

$E_{Tissue-Exp} = E_{A-Exp} / \frac{E_{A-FE}}{E_{Tissue-FE}}$ →The experimentally derived average tissue modulus was determined from the using parameters from finite element model and from the experimentally measured $E_{A\text{-}Exp}$.

The local tissue stresses from the finite element model were calculated using the constant finite element tissue modulus of 10 GPa. Since a linear element finite element model was used. The derived experimental tissue modulus can be used to scale local tissue stresses to the correct magnitude using the scale factor ratio $E_{Tissue\text{-}Exp}/ E_{Tissue\text{-}FE}$.

Aim 4: Histological Sections of the distal Rabbit Femur Visualized using Confocal Microscopy

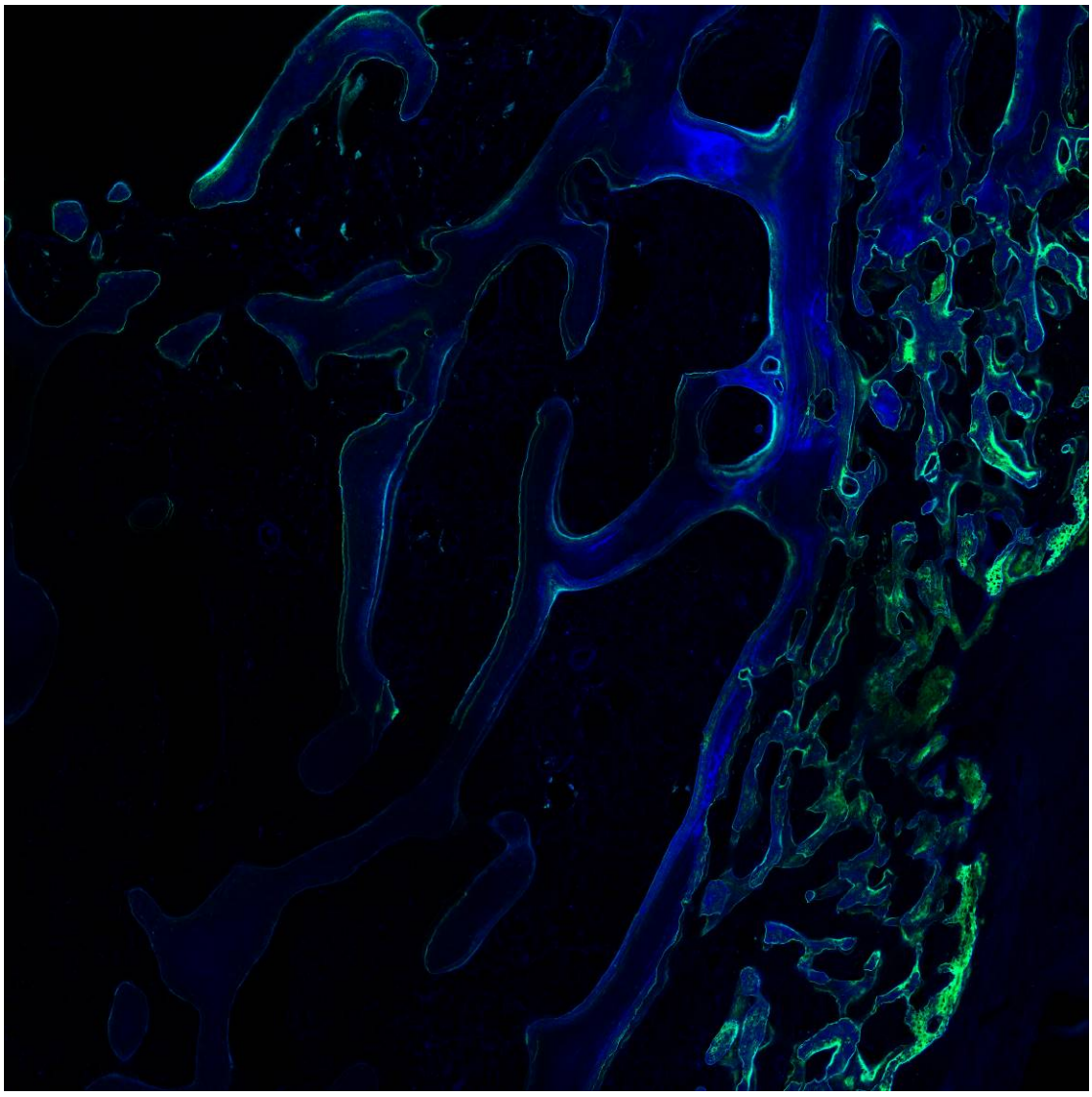

Rabbit 74 Loaded Limb-Maximum Intensity Projection Image

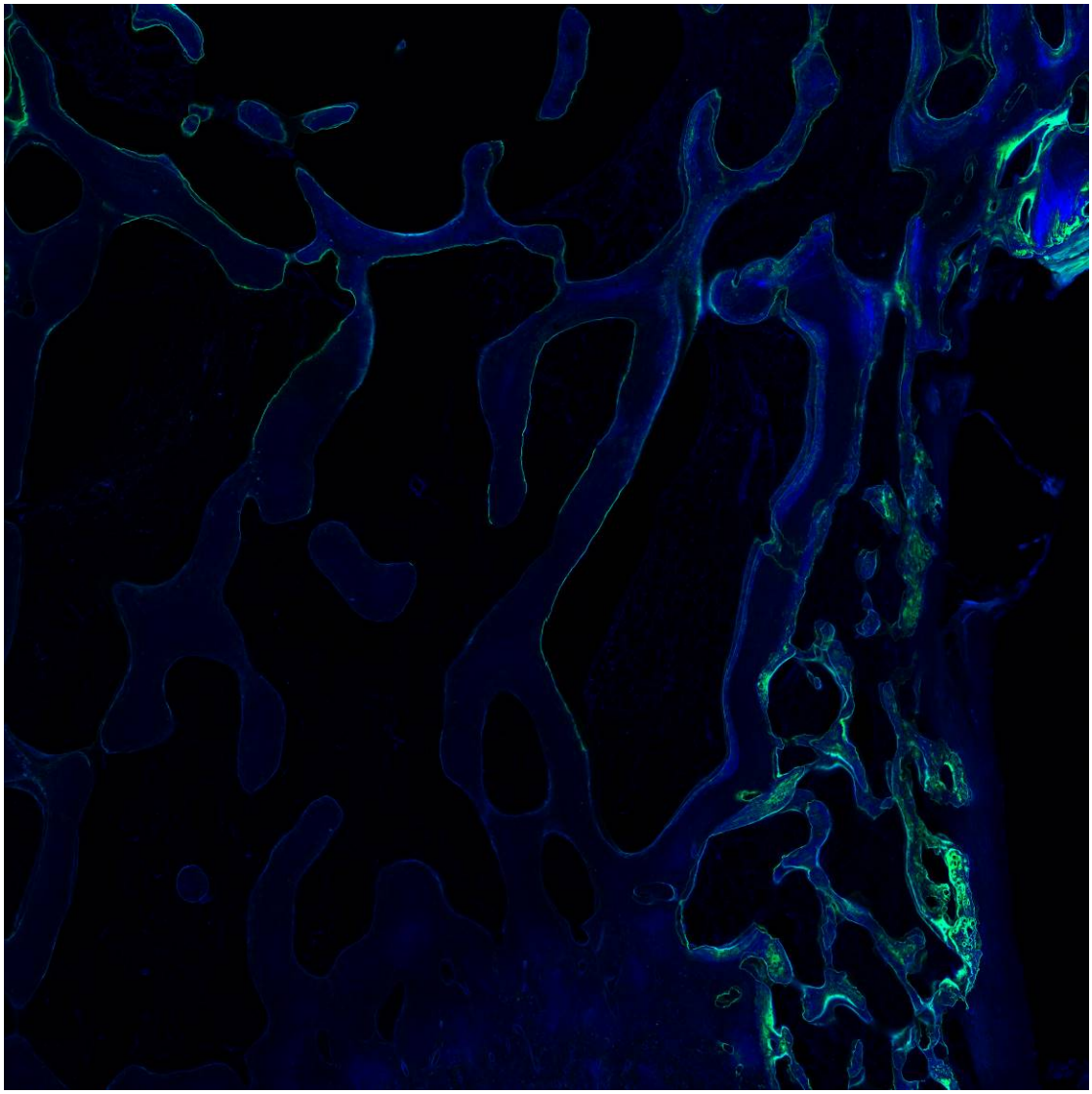

Rabbit 74 Control Limb-Maximum Intensity Projection Image

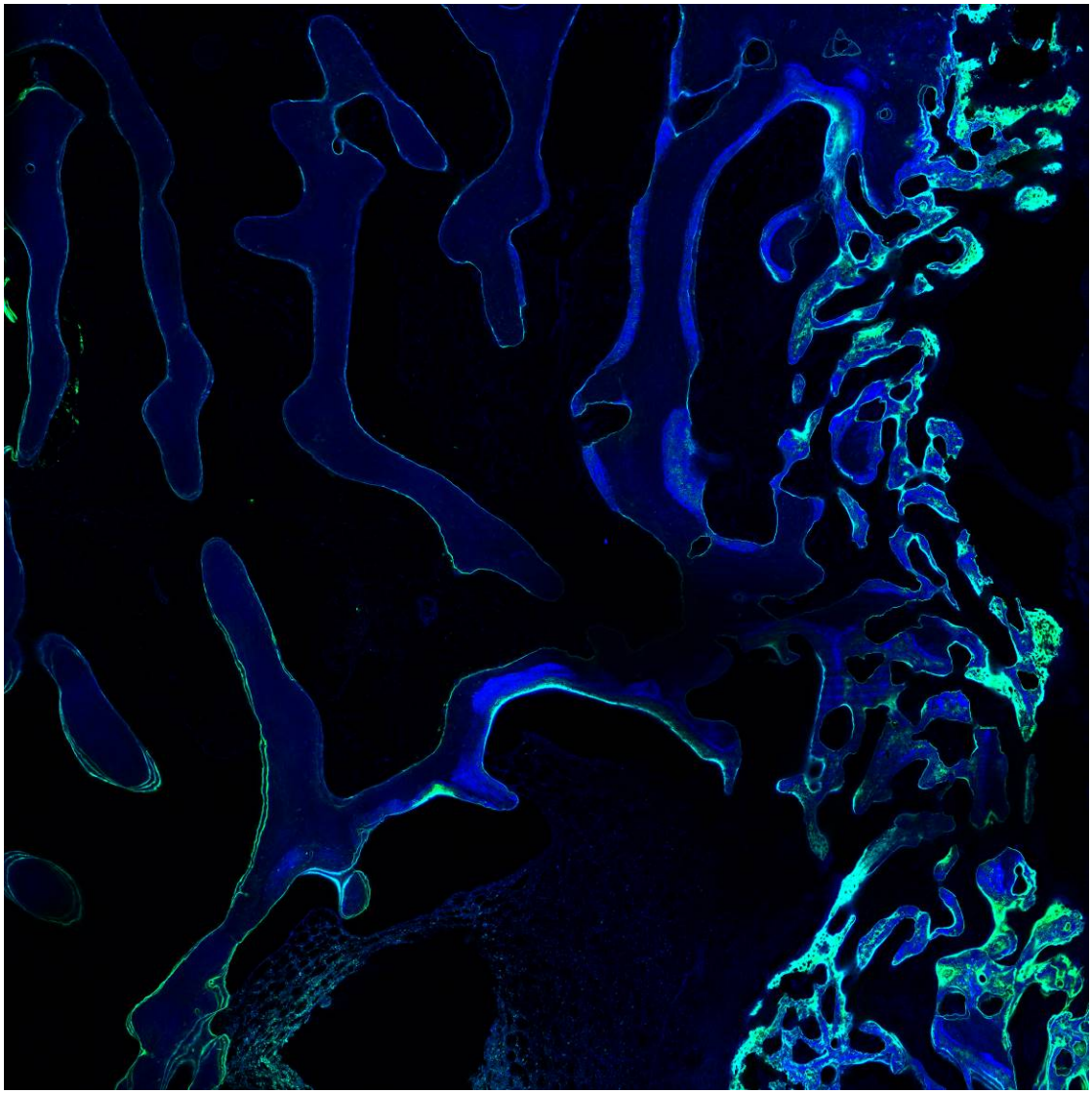

Rabbit 75 Loaded Limb-Maximum Intensity Projection Image

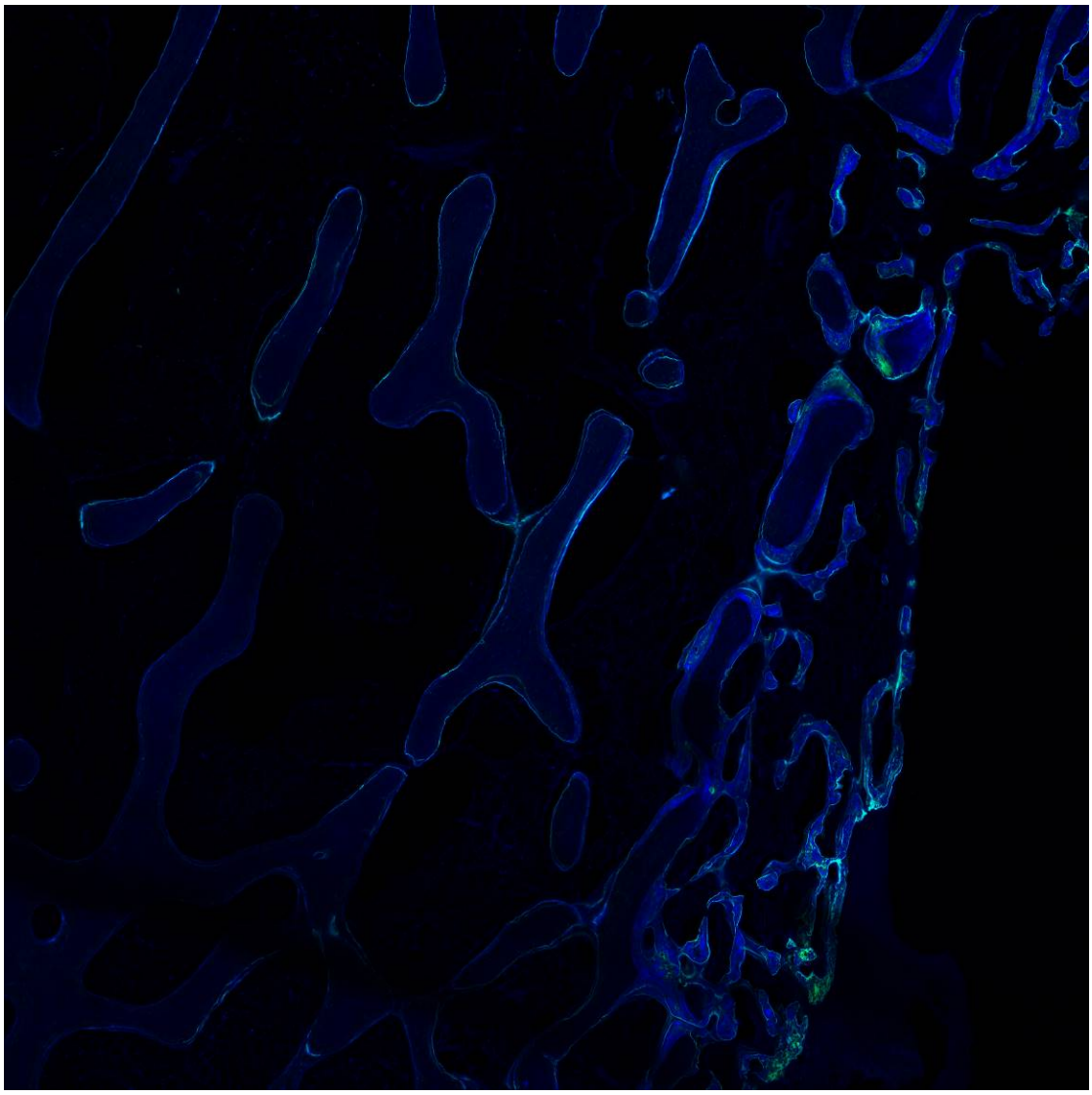

Rabbit 75 Control Limb-Maximum Intensity Projection Image

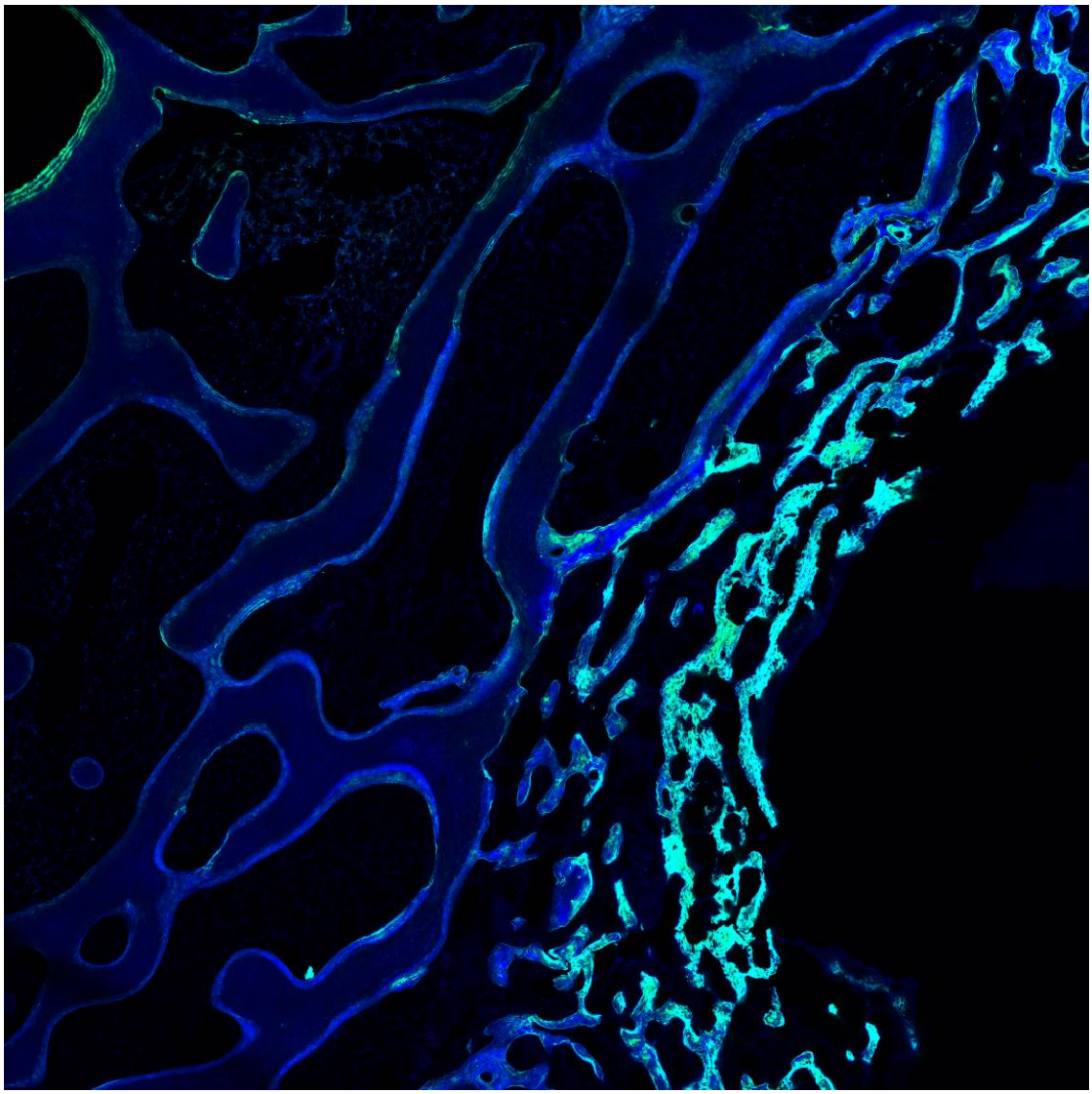

Rabbit 76 Loaded Limb-Maximum Intensity Projection Image

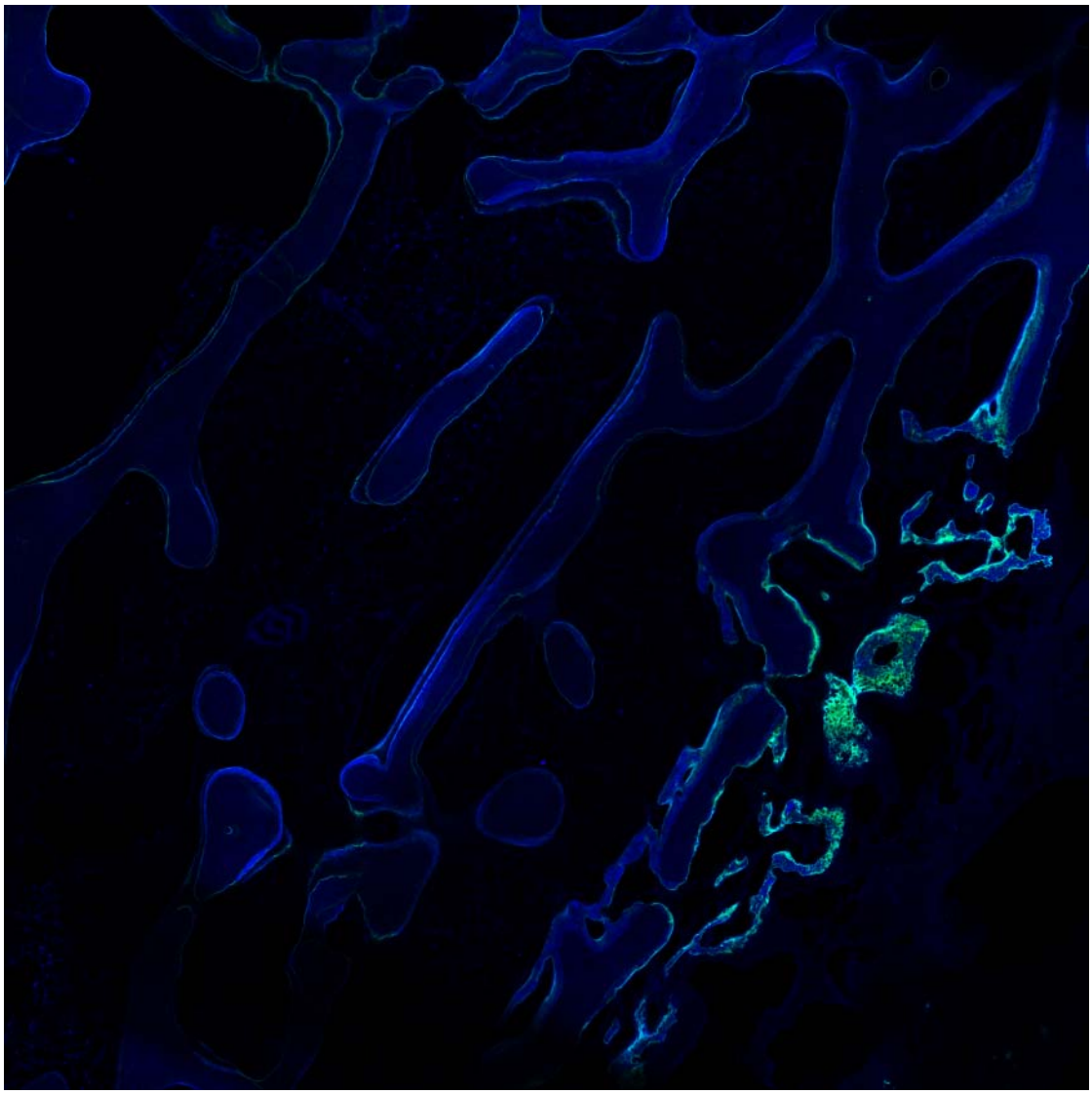

Rabbit 76 Control Limb-Maximum Intensity Projection Image